論文 / 著書情報
Article / Book Information

題目(和文)	繊維強化プラスチックから発生するAE信号のb値解析
Title(English)	b-Value analysis of AE signals from fiber reinforced plastics
著者(和文)	ジョン ドユン
Author(English)	JUNG DOYUN
出典(和文)	学位:博士(工学), 学位授与機関:東京工業大学, 報告番号:甲第10628号, 授与年月日:2017年9月20日, 学位の種別:課程博士, 審査員:水谷 義弘,轟 章,髙原 弘樹,井上 裕嗣,因幡 和晃
Citation(English)	Degree:Doctor (Engineering), Conferring organization: Tokyo Institute of Technology, Report number:甲第10628号, Conferred date:2017/9/20, Degree Type:Course doctor, Examiner:,,,,
学位種別(和文)	博士論文
Type(English)	Doctoral Thesis

TOKYO INSTITUTE OF TECHNOLOGY

b-Value analysis of acoustic emission signals from fiber reinforced plastic

by

Jung Do-yun

A thesis submitted to Tokyo Institute of Technology for the degree of

Doctor of Engineering

Department of Mechanical Sciences and Engineering
Tokyo Institute of Technology
2-12-1 O-okayama, Meguro, Tokyo 152-8552, Japan

Abstract

Acoustic emission (AE) testing is a major non-destructive testing method used for integrity evaluation of structures. Amplitude distributions of AE signals are characterized by the *b*-value. This value is mainly used for integrity evaluation of concrete structures. The value is assumed to be independent of propagation distance between the AE source and its sensor.

This study investigated the applicability of *b*-values to integrity evaluation of fiber-reinforced plastics (FRPs). By analyzing real and simulated AE signals from FRPs, it was found that the *b*-value is not independent of the propagation distance for these materials. FRPs have several fracture modes and each mode generates AE with a different frequency range. It was found that the change in *b*-value of FRPs is caused by the frequency dependence of attenuation of the AE signals.

The amplitude distributions of AE signals at the AE source were estimated from signals detected by AE sensors placed at different propagation distances. Because the amplitude distribution at the source is independent of propagation distance, a new parameter (named the modified *b*-value), calculated from this distribution, was proposed for integrity evaluation of FRPs.

Table of contents

Chapter 1 Introduction

Fiber-reinforced plastics (FRPs) are hybrid materials that contain fibers as reinforcements and plastics as matrixes, and they are widely used in the chemical and mechanical industries. To ensure the soundness of FRP structures, it is important to evaluate their integrity by non-destructive testing (NDT). Acoustic emission testing (AT) is an NDT method that is able to detect damage in mechanical structures by using acoustic emission (AE) signals that are generated by such damage. Amplitude distributions of AE signals are characterized by the *b*-value, which is used to evaluate the severity of damage [1-1]–[1-5]. *b*-Value analysis is considered an ideal way to determine the integrity of real structures. Furthermore, the analysis can be performed in real time and thus enables monitoring of damage in real structures using AE sources. In civil engineering, the *b*-value is used for evaluating damage in ground slopes and concrete structures [1-6]–[1-12]. There are now demands to use the *b*-value for integrity evaluation of FRP structures. FRPs are known to have several fracture modes: each mode generates AE comprising a different frequency range [1-13]–[1-15]. It is known that attenuation of AE changes with its frequency. To date, the *b*-value has been used mainly for structures that generate a narrow AE frequency range, such as concrete structures [1-16]–[1-20]: changes in attenuation by difference AE frequencies have therefore not been discussed. This thesis discusses the effects of propagation length and frequency of AE from FRPs on the *b*-value.

1.1 Acoustic emission testing and *b*-value analysis

The most advanced method to detect simple harmonic motion is AT. The technique is based on the detection of dynamic surface motion caused by an elastic wave. AE signals are generated by energy that is elastically stored by micro- and/or macro-cracks during deformation and failure of materials. Modern AE systems are so powerful that AE signal waveforms, which are used to analyze AE signals, can be accurately recorded in real time. Several AE parameters, such as amplitude, threshold, and number of hits, can be derived from the AE signal [1-21]–[1-25].

The intensity of an AE signal is represented by its amplitude: the amplitude of the peak voltage of the signal waveform is usually assigned. Instead of a linear scale, amplitudes are expressed on a decibel scale, where 1 μV at a sensor is defined as 0 dB_{AE}. The amplitude is closely related to the magnitude of the AE source. Recording is triggered once the output AE signal reaches a set threshold value based on amplitude. An AE signal hit is defined as the number of times that the signal exceeds a defined threshold [1-21]–[1-25].

1.1.1 Previous studies concerning the *b*-value

The concept of the *b*-value originates from the field of earthquake seismology. The Gutenberg–Richter equation expresses the relationship between magnitude of an earthquake (*M*) and the number of earthquakes larger than magnitude *M* as empirical equations [1-26]:

$$\log_{10} N(M) = a - bM \ , \tag{1-1}$$

$$N(M) = \int_M^\infty n(M) dM \ , \tag{1-2}$$

where *M* is the magnitude of an earthquake, *n*(*M*) is the number of earthquakes with magnitude *M*, *N*(*M*) is the total number of earthquakes larger than magnitude *M*, and *a* and *b* are empirical constants. *b* is a parameter that provides the possibility of describing the stress and materials conditions in the focal region. High *b*-values are an indication of a low-stress level in a genetic seismic zone; conversely, low *b*-values are correlated with high-stress conditions.

To compare AE results with those from seismology, it was reported that a multiplier of 20 should be used with the *b*-value obtained from AE [1-7]. An alternative method, known as the improved *b*-value, *Ib*-value, was proposed to evaluate slope failure, as shown in Equation (1-3):

$$N(w_1) = N(\mu - \alpha_2 \cdot \sigma) = \int_{\mu-\alpha_2\cdot\sigma}^{\infty} n(a) da \ ,$$

$$N(w_2) = N(\mu - \alpha_1 \cdot \sigma) = \int_{\mu-\alpha_1\cdot\sigma}^{\infty} n(a) da \ , \tag{1-3}$$

$$Ib = \frac{\log_{10} N(w_1) - \log_{10} N(w_2)}{(\alpha_1 + \alpha_2) \cdot \sigma} \ , \tag{1-4}$$

where σ is the standard deviation, μ is the mean value of the amplitude distribution, α_1 is a coefficient related to smaller amplitudes, and α_2 is a coefficient related to the fracture level. This method was applied to AE by modifying the *Ib*-value as shown in Equation (1-4), where ($\mu - \alpha_1 \cdot \sigma$) is the number of hits with an amplitude greater than ($\mu - \alpha_2 \cdot \sigma$) and ($\mu - \sigma$) is the number of hits with an amplitude exceeding ($\mu + \sigma$) [1-27], [1-28]. Test results showed that this method successfully followed the progression of slope failures ([1-8], [1-9], [1-16], [1-19]).

Shiotani applied the *Ib*-value in bending tests on two reinforced concrete and two fiber-reinforced concrete specimens. The fiber-reinforced specimens were half plain concrete and half vinyl fiber-reinforced mortar. All specimens were 150 mm × 150 mm × 530 mm (6 in. × 6 in. × 21 in.) in dimension and reinforced with two bars of 13 mm (0.5 in.) diameter on the tension side. Twelve 60 kHz resonant sensors were used for data acquisition. It was observed that as the load was increased in a stepwise manner, the range of the *Ib*-value decreased. A threshold of 0.05 was used, such that *Ib*-values lower than 0.05 (which equals unity after applying the multiplier of 20) indicated significant damage. Recently, Antorino et al. [1-18] proposed a method of calculating wavelet *b*-value using a divided AE source and a complex mole continuous wavelet transform. Wavelet *b*-value, cumulative AE energy (CAE), and cumulative dissipated energy (CDE) were applied to AE signals from dynamic tests conducted on a reinforced-concrete slab. The steel reinforcement bars did not yield during the tests, but a severe loss of bonding between the bars and the surrounding concrete was detected. Accordingly, the CDE, CAE, and wavelet *b*-value changed at the onset of slippage of the reinforcing bar within the concrete.

1.1.2 One- and two-dimensional location methods

A great advantage of the AE method is that the location of the AE source can be determined relatively easily. The location of an AE source is defined as the position where AE signals are generated and can be estimated using AE signals detected by AE sensors at different positions. This is the same method as that used to determine the location of an earthquake center. In the location method, the wave velocity of the object and the arrival time of the AE wave must be known. Consequently, because a clear rising point of the waveform is observed in the detected burst of AE waveforms generated by micro-cracking, it is easy to detect the arrival time of an AE wave, thereby enabling a relatively accurate location to be determined. However, because continuous AE waveforms associated with plastic deformations do not exhibit a clear rising point, it is difficult to determine the arrival time of the AE wave; therefore, an accurate location cannot be determined.

In general, it is desirable to determine the three-dimensional location of the damage position; however, when the number of measurable channels and number of sensors are limited or when the shapes of the object are specific, it is difficult to determine the three-dimensional location of the damage. With a known velocity, only an arrival time interval is needed for the order of a location to be determined; i.e., the minimum numbers of sensors required for one-, two-, and three-dimensional locations are two, three, and four, respectively.

Detection of a burst waveform from a one-dimensional location is now discussed. Assuming that AE is generated between two AE sensors, the location of the AE source is x, and the locations of the two sensors are x_1 and x_2, we can derive an equation for times t_1 and t_2 at which the AE wave reaches the respective sensors:

$$Ct_1 = |x - x_1|, Ct_2 = |x - x_2|, \tag{1-6}$$

where C is the velocity of the AE wave. Furthermore, assuming that there is a difference between the arrival times at the two sensors, we have:

$$C\Delta t_{12} = |x - x_1| - |x - x_2|. \tag{1-7}$$

The velocity and positions of the sensors are known. From Equation (1-6), the one-dimensional location of the AE source, *x*, can be determined, as shown in Figure 1.1.

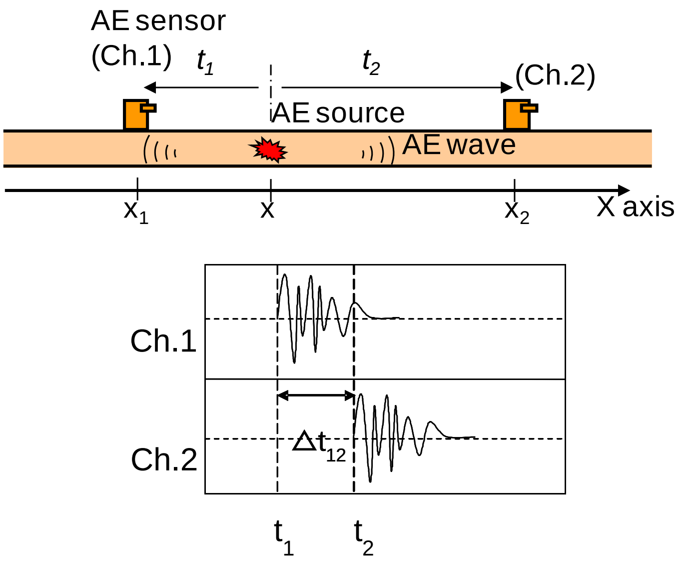

Figure 1.1 Determination of linear source location from one-dimensional data

Similarly, three sensors enable the planar or two-dimensional (x, y) location of an AE source to be determined. Assuming that the velocity is C, the positions of the three sensors are (x_1, y_1), (x_2, y_2), and (x_3, y_3), the arrival times at the sensors are t_1 and t_2, and the differences between the arrival times at the sensors are Δt_{12} and Δt_{13}, as mentioned above, we thus have (see Figure 1.2):

$$C\Delta t_{12} = \sqrt{(x-x_1)^2 + (y-y_1)^2} - \sqrt{(x-x_2)^2 + (y-y_2)^2}\ ; \qquad (1.8)$$

$$C\Delta t_{13} = \sqrt{(x-x_1)^2 + (y-y_1)^2} - \sqrt{(x-x_3)^2 + (y-y_3)^2}\ . \qquad (1.9)$$

These two equations have two unknown *x*- and *y*-values and can therefore be solved. Numerical solution of non-linear equations obtained using a computer enables us to easily determine the two-dimensional location of the AE source.

The precision of location achieved by these methods depends mainly on the resolution of the arrival times, sensor sizes, and the sensor-to-sensor interval.

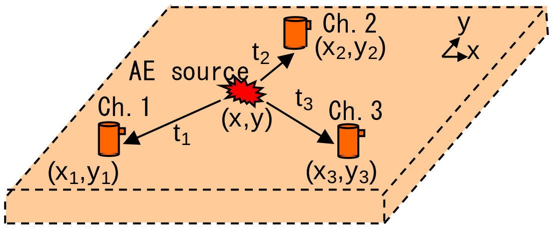

Figure 1.2　Determination of planar source location

1.2 Fiber-reinforced plastics

1.2.1 Fracture behavior

Owing to the anisotropy of FRP materials, different failure modes can occur simultaneously or successively before the entire structure fails. FRPs consist of two different phases so failure can occur in either of the phases or at their interface. Failures that could develop in FRPs include fiber breaks, matrix cracks, de-bonding, and delamination (Figure 1.3). De-bonding is the separation of the matrix from individual fibers, which can also lead to fiber pull-outs; delamination is the separation of fiber layers or piles. The time at which failure appears is dependent on the strength and elasticity of both materials and their interface. Some of these failure modes can be initiated at low load levels and will grow under subsequent loading [1-32].

If tensile stress is applied to an FRP in the direction of the fiber, some fibers will eventually break at their weakest point and the stress will redistribute over the matrix to other fibers. If the ultimate tensile strength is exceeded, more fibers will break, and eventually the whole structure will fail.

If a compressive load is applied on a unidirectional FRP in the direction of the fiber, the strength of the FRP mainly depends on the strength of the matrix–fiber bonding [1-33]. De-bonding can occur at weak bonds at relatively low stresses. Another problem is that matrix cracks develop where the force is transmitted into the FRP if the force is not adequately distributed.

Critical stresses for FRPs are shear stresses. The shear strength is always lower than the tensile strength. Most FRPs therefore have layers of fibers in different directions or even woven fiber lay-ups. The aim is always to have fibers that can be loaded under tensile stress. If the shear stress is parallel to the fibers, the shear strength depends on the shear strength of the matrix and the matrix–fiber interface [1-33]. A bent bar will fail due to shear stresses in the natural plane before it breaks by tensile failure of the outer fibers. Owing to the sensitivity of FRPs to shear stress, bolted joints should be avoided. Loads that are transferred from one FRP to another are diffused away from the joints by shear stress [1-33].

Today's knowledge of FRP materials is still inadequate for proper fatigue design [1-34]–[1-35]. For most newly developed FRP structures, a prototype must be built and tested to verify the design and ensure the required certifications, such as those of the International Standards Organization (ISO), the American Society for Testing and Materials (ASTM), or the Deutsches Institut für Normung e.V. (German Institute for Standardization) (DIN). The main problem with fatigue damage is that very small cracks can occur that may not be detectable with NDT techniques, such as, for example, ultrasonic scanning. Small flaws can merge very quickly to develop into a fast-propagating crack and thereby adversely affect the structural health of a component. For maintenance, different failure modes have to be detected and recognized using an appropriate NDT technique.

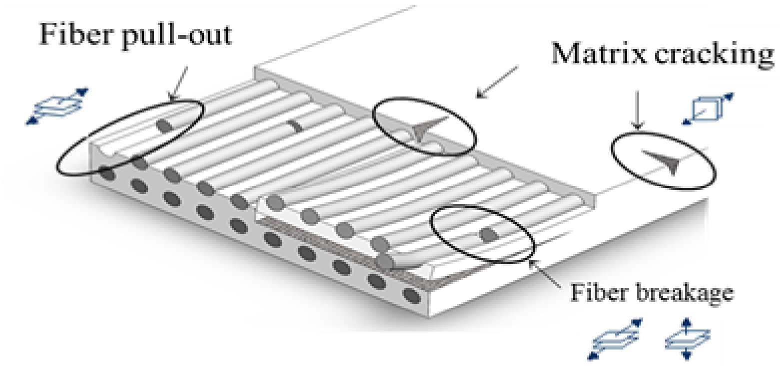

Figure 1.3 Fracture mode in fiber-reinforced plastics

1.2.2 Acoustic emission testing

The amplitude of AE is closely related to the magnitude of the source event. The magnitude of the amplitude in each signal has often been analyzed in relation to the its frequency. Features of AE signals are generally known to change with the type of fracture. Different fracture types in FRP materials generate different AE signals that vary over a range of frequencies and amplitudes [1-16], [1-29]. Groot et al. [1-13] and Ramirez-Jimenez et al. [1-15] measured AE in load testing of a comprehensive series of carbon (CFRP; 50–550 kHz) and glass (GFRP; 80–520 kHz) FRPs and classified the detected AE signals based on their frequency spectra. Gutkin et al [1-31]. studied the frequency distribution of AE signals recorded in several tests of various fiber stacking sequences of CFRPs using pattern recognition techniques (matrix cracking: 0–50 kHz; de-bonding: 200–300 kHz; delamination: 50–100 kHz; fiber fracture: 400–500 kHz). These materials exhibit a wider frequency band compared with those of Earth's crust, rock formations, and engineering concrete.

During the propagation of an AE signal through a solid medium from its source, it can suffer attenuation from refraction, diffraction, and scattering. The intensity of an AE signal decreases as propagation from the source increases. It is evident that attenuation suffered by propagation of AE signals generated by dynamic disturbances will affect the waveform of the AE source. In a homogeneous medium, these losses usually occur as a certain percentage of the wave packet energy per unit length of propagation. Theoretically, this manifests as an exponential decrease in amplitude with propagation distance and can be expressed as [1-36]–[1-38]:

$$A = A_0 \cdot \exp[-\alpha(\omega) \cdot x], \tag{1-5}$$

where α is the attenuation and A is the amplitude after propagation from source A_0. The attenuation of higher frequencies is most affected by increasing propagation distance (d). Understanding the propagation of AE signals in homogeneous, anisotropic materials and the scattering caused by inhomogeneities is of benefit to various engineering fields. Scattering becomes increasingly important in complex geometries where there are a number of discontinuities between the source and sensor.

Absorption is the process by which kinetic and acoustic energy are converted into heat due to internal friction. The rate of absorption is greater at higher frequencies owing to the shorter wavelengths. In contrast to geometric spreading, where the rate of attenuation is a function of the distance from the source, amplitude reduction due to absorption occurs at a constant rate. Absorption therefore becomes relatively more important further away from the source.

1.2.3 Degradation

Considering their often harsh service environments, FRPs are very sensitive to moisture, acid rain, ultraviolet (UV) radiation, and thermal cycling owing to the presence of unexpected elements [1-39]–[1-40]. UV radiation in the presence of atmospheric oxygen induces chemical changes in epoxy polymer matrices, which is a very complex process. This is sometimes referred to as a photo-oxidation process and ultimately changes the mechanical behavior of FRP materials. Covalent bonds present in the polymer dissociate and form free radicals when UV radiation is absorbed by chromophoric polymers. This is followed by molecular cross-linking and chain scission [1-41]. Visually, surface yellowing discoloration occurs as a result of UV radiation, in which light photons react with polymer chains, leading to instability in mechanical properties. Natural UV radiation has both short and long wavelengths; the short wavelengths have higher photon energies, to which the polymer resin matrix is very sensitive, so there is the chance of breaking the chemical bonds between molecular compounds [1-42]. A decrease of 15% in average failure strain and 18% decrease in tensile modulus was observed by Shokrieh et al. for polyester resin composites exposed to UV radiation for 100 h. It was reported that the strength retention of a 0.13 mm (l ply) unidirectional DuPont Kevlar-49 epoxy laminate after 1000 h UV irradiation on both surfaces was −60% [1-43]. Chevali investigated flexural creep behavior of long-fiber-reinforced thermoplastic (LFT) composites as a function of UV irradiation and moisture absorption. Creep values increased with increasing UV conditioning duration, whereas, in some cases, significant changes in creep values were observed [1-44]. Some authors have investigated the inner structure of materials after exposure to accelerated UV radiation [1-45].

1.3 Thesis outline

This thesis presents a *b*-value analysis for structural health monitoring in FRP structures. Figure 1.4 presents a flow chart for the thesis structure.

Chapter 1: Introduction

This chapter describes the inspiration for the present work and outlines the essential approach of evaluating FRP structural health using *b*-value analysis.

Chapter 2: Problems when applying *b*-value to FRP structures

The applicability of the *b*-value to integrity evaluation of FRPs is discussed. Tensile testing of CFRP with several stacking sequences and GFRP with woven fiber were conducted. AE signals from a center hole of plate specimens were detected by several AE sensors positioned at different distances from the hole.

Chapter 3: Cause of changes in *b*-value with propagation distance

The cause of changes in the *b*-value with propagation distance was investigated. The *b*-value was analyzed for AEs detected at different propagation distances from an AE source.

Chapter 4: Effect of ultraviolet radiation-induced degradation of fiber-reinforced plastics on *b*-value

The cause of changes in the *b*-value with increasing UV irradiation time was investigated. The *b*-value was analyzed for AEs detected for different UV irradiation times of an AE source.

Chapter 5: Modified *b*-value for integrity evaluation of fiber-reinforced plastics

This chapter proposes a new parameter, named the modified *b*-value. The feasibility of using this value was evaluated. The modified *b*-value can be calculated from AE data detected at different propagation distances from the AE source. The modified *b*-value is the slope of the estimated amplitude distribution of AE signals at the source position.

Chapter 6: Conclusions

This thesis presents an analysis of using the *b*-value for structural health monitoring in FRPs. *b*-Value distributions in FRPs were investigated by AT and parametric study. Findings obtained from the experiments were used to propose a new *b*-value specifically for structural health monitoring of FRPs. This value seems suitable for use in continuous monitoring of FRP structures.

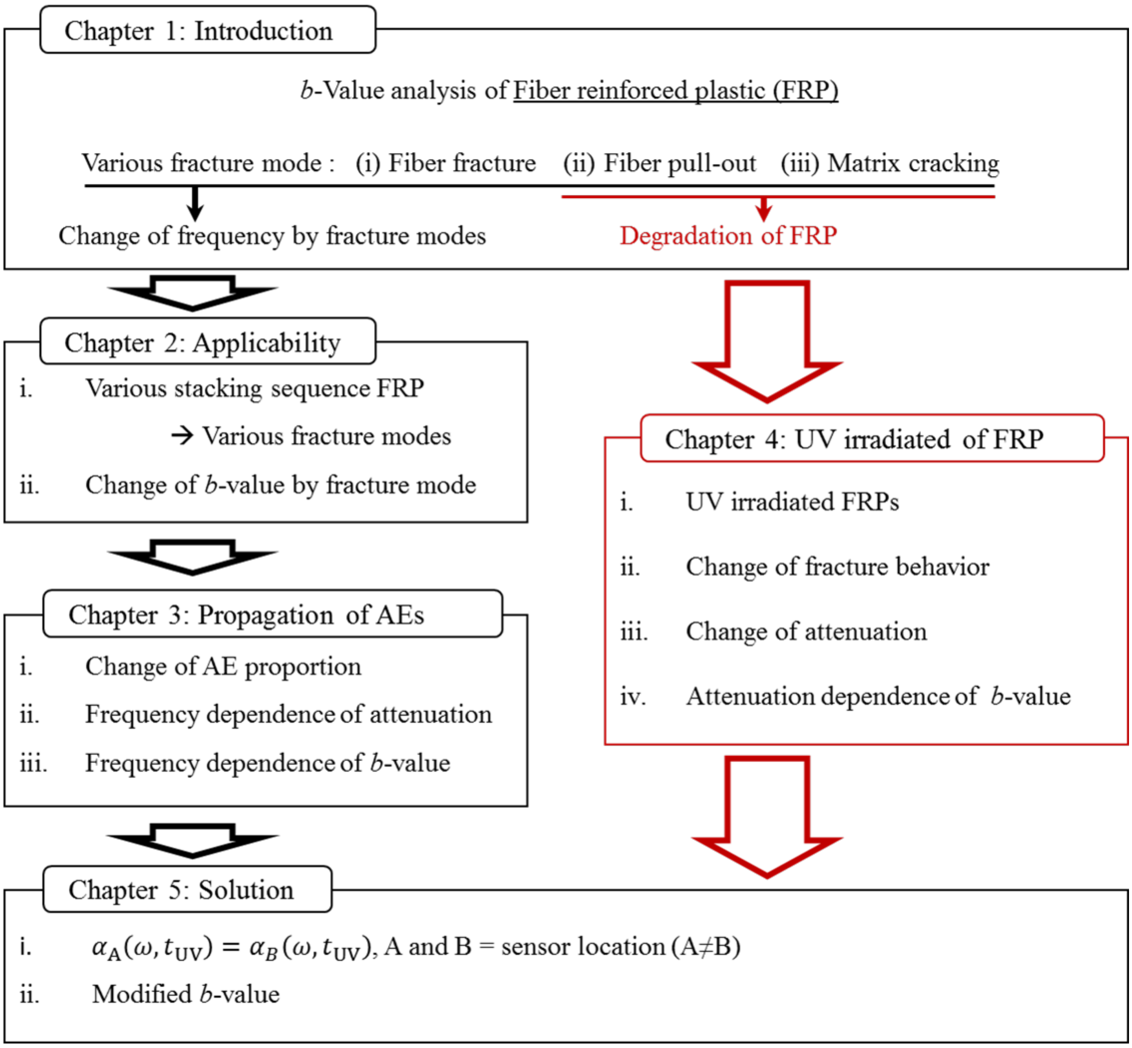

Figure 1.4 Flow chart of thesis

1.4 References

[1-1] Roberts, T. M., & Talebzadeh, M. (2003). Fatigue life prediction based on crack propagation and acoustic emission count rates. *Journal of Constructional Steel Research*, *59*(6), 679-694.

[1-2] Roberts, T. M., & Talebzadeh, M. (2003). Acoustic emission monitoring of fatigue crack propagation. *Journal of Constructional Steel Research*, *59*(6), 695-712.

[1-3] Ni, Q. Q., & Iwamoto, M. (2002). Wavelet transform of acoustic emission signals in failure of model composites. *Engineering Fracture Mechanics*, *69*(6), 717-728.

[1-4] Coverley, P. T., & Staszewski, W. J. (2003). Impact damage location in composite structures using optimized sensor triangulation procedure. *Smart materials and structures*, *12*(5), 795.

[1-5] Diamanti, K., & Soutis, C. (2010). Structural health monitoring techniques for aircraft composite structures. *Progress in Aerospace Sciences*, *46*(8), 342-352.

[1-6] Colombo, I. S., Main, I. G., & Forde, M. C. (2003). Assessing damage of reinforced concrete beam using "*b*-value" analysis of acoustic emission signals. *Journal of materials in civil engineering*, *15*(3), 280-286.

[1-7] Shiotani, T., Fujii, K., Aoki, T., & Amou, K. (1994). Evaluation of progressive failure using AE sources and improved *b*-value on slope model tests. *Progress in acoustic emission*, *7*(7), 529-534.

[1-8] Shiotani, T., Yuyuma, S., Li, Z. and Ohtsu, M. (2001). Application of AE improved *b*-value to quantitative evaluation of fracture process in concrete materials. Journal of Acoustic Emission, 18, 118-133 .

[1-9] Shiotani, T., Luo, X., Haya, H., & Ohtsu, M. (2007, July). DAMAGE QUANTIFICATION FOR CONCRETE STRUCTURES BY IMPROVED *b*-VALUE ANALYSIS OFAE. In *Earthquakes and Acoustic Emission: Selected Papers from the 11th International Conference on Fracture, Turin, Italy, March 20-25, 2005* (p. 181). CRC Press.

[1-10] Sagar, R. Vidya, BK Raghu Prasad, and S. Shantha Kumar. "An experimental study on cracking evolution in concrete and cement mortar by the *b*-value analysis of acoustic emission technique." *Cement and Concrete Research* 42.8 (2012): 1094-1104.

[1-11] Sagar, R. V., Prasad, B. R., & Kumar, S. S. (2012). An experimental study on cracking evolution In concrete and cement mortar by the *b*-value analysis of acoustic emission technique. *Cement and Concrete Research*, *42*(8), 1094-1104.

[1-12] Schumacher, T., Higgins, C. C., & Lovejoy, S. C. (2011). Estimating operating load conditions on reinforced concrete highway bridges with b-value analysis from acoustic emission monitoring. Structural Health Monitoring, 10(1), 17-32.

[1-13] de Groot, P.J., Wijnen, P.A.M., Janssen, R.B.F.: Real-time frequency determination of acoustic emission for different fracture mechanisms in carbon/epoxy composites. Compos. Sci. Technol. 55, 405–412 (1995). doi:10.1016/0266-3538(95)00121-2

[1-14] Ramirez-Jimenez, C.R., Papadakis, N., Reynolds, N., Gan, T.H., Purnell, P., Pharaoh, M.: I dentification of failure modes in glass/polypropylene composites by means of the primary frequency content of the acoustic emission event. Compos. Sci. Technol. 64, 1819–1827 (2004).

[1-15] Gutkin, R., Green, C.J., Vangrattanachai, S., Pinho, S.T., Robinson, P., Curtis, P.T.: On acoustic emission for failure investigation in CFRP: Pattern recognition and peak frequency analyses. Mech. Syst. Signal Process. 25, 1393–1407 (2011).

[1-16] Grosse, C. U., & Ohtsu, M. (Eds.). (2008). Acoustic emission testing. Springer Science & Business Media.

[1-17] Aggelis, D. G. (2011). Classification of cracking mode in concrete by acoustic emission parameters. Mechanics Research Communications, 38(3), 153-157.

[1-18] Zitto, M. E., Piotrkowski, R., Gallego, A., Sagasta, F., & Benavent-Climent, A. (2015). Damage assessed by wavelet scale bands and b-value in dynamical tests of a reinforced concrete slab monitored with acoustic emission. Mechanical Systems and Signal Processing, 60, 75-89.

[1-19] ElBatanouny, M. K., Larosche, A., Mazzoleni, P., Ziehl, P. H., Matta, F., & Zappa, E. (2014). Identification of cracking mechanisms in scaled FRP reinforced concrete beams using acoustic emission. Experimental Mechanics, 54(1), 69-82.

[1-20] Zaki, A., Chai, H. K., Behnia, A., Aggelis, D. G., Tan, J. Y., & Ibrahim, Z. (2017). Monitoring fracture of steel corroded reinforced concrete members under flexure by acoustic emission technique. Construction and Building Materials, 136, 609-618.

[1-21] Kyōkai, N. H. H. K. (2016). Practical acoustic emission testing.

[1-22] B. Muravin. (2010) Acoustic Emission wave propagation and source location. [Online]. http://www.muravin.com/

[1-25] Sause, M. G. (2016). In situ monitoring of fiber-reinforced composites: theory, basic concepts, methods, and applications (Vol. 242). Springer.

[1-26] Gutenberg, B., and Richter, C.F. "Magnitude and energy of earthquakes." Annals of Geophysics 9.1 (1956): 1-15.

[1-27] Aggelis, D. G. (2011). Classification of cracking mode in concrete by acoustic emission parameters. Mechanics Research Communications, 38(3), 153-157.

[1-28] Aggelis, D. G., Shiotani, T., Momoki, S., & Hirama, A. (2009). Acoustic emission and ultrasound for damage characterization of concrete elements. ACI Materials Journal, 106(6), 509.

[1-29] Mizutani, Yoshisiro., Nagashima, K., Takemoto, M., & Ono, K. (2000). Fracture mechanism characterization of cross-ply carbon-fiber composites using acoustic emission analysis. Ndt & E International, 33(2), 101-110.

[1-30] Hafizi, Z. M., Epaarachchi, J., & Lau, K. T. (2013). An investigation of acoustic emission signal attenuation for monitoring of progressive failure in fiberglass reinforced composite laminates. International Journal of Automotive and Mechanical Engineering, 8, 1442.

[1-31] Gutkin, R., Green, C.J., Vangrattanachai, S., Pinho, S.T., Robinson, P., Curtis, P.T.: On acoustic emission for failure investigation in CFRP: Pattern recognition and peak frequency analyses. Mech. Syst. Signal Process. 25, 1393–1407 (2011).

[1-32] Z. M. Hafizi, Epaarachchi, J., Lau, K.T.: AN INVESTIGATION OF ACOUSTIC EMISSION SIGNAL ATTENUATION FOR MONITORING OF PROGRESSIVE FAILURE IN FIBERGLASS REINFORCED COMPOSITE LAMINATES. Int. J. Automot. Mech. Eng. 8, 1442–1456 (2013).

[1-33] Wevers, M. (1997). Listening to the sound of materials: acoustic emission for the analysis of material behaviour. NDT & E International, 30(2), 99-106.

[1-34] Langley, M. (1973). Carbon fibres in engineering. McGraw-Hill.

[1-35] Wevers, M. (1997). Listening to the sound of materials: acoustic emission for the analysis of material behaviour. NDT & E International, 30(2), 99-106.

[1-36] Scholey, J. J., Wilcox, P. D., Lee, C. K., Friswell, M. I., & Wisnom, M. R. (2006).

Acoustic emission in wide composite specimens. In Advanced Materials Research (Vol. 13, pp. 325-332). Trans Tech Publications.

[1-37] Owino, J. O., Jacobs, L. J., (1999), Attenuation measurements in cementbased materials using laser ultrasonics, Journal of Engineering Mechanics June: 637-647.

[1-38] Philippidis T.P., Aggelis D. G., 2005, Experimental study of wave dispersion and attenuation in concrete, Ultrasonics, Vol. 43, pp. 584-595.

[1-39] Drzal, L. T., Rich, M. J., & Lloyd, P. F. (1983). Adhesion of graphite fibers to epoxy matrices: I. The role of fiber surface treatment. The Journal of Adhesion, 16(1), 1-30.

[1-40] Bockenheimer, C., Fata, D., & Possart, W. (2004). New aspects of aging in epoxy networks. II. Hydrothermal aging. Journal of Applied Polymer Science, 91(1), 369-377.

[1-41] Yano, O., & Yamaoka, H. (1995). Cryogenic properties of polymers. Progress in Polymer Science, 20(4), 585-613.

[1-42] Bockenheimer, C., Fata, D., & Possart, W. (2004). New aspects of aging in epoxy networks. II. Hydrothermal aging. Journal of Applied Polymer Science, 91(1), 369-377.

[1-43] Shokrieh, M. M., & Bayat, A. (2007). Effects of ultraviolet radiation on mechanical properties of glass/polyester composites. Journal of Composite materials, 41(20), 2443-2455.

[1-44] Chevali, V. S., Dean, D. R., & Janowski, G. M. (2010). Effect of environmental weathering on flexural creep behavior of long fiber-reinforced thermoplastic composites. Polymer Degradation and Stability, 95(12), 2628-2640.

[1-45] Sethi, S., & Ray, B. C. (2014). An assessment of mechanical behavior and fractography study of glass/epoxy composites at different temperatures and loading speeds. Materials & Design, 64, 160-165.

Chapter 2 Problems when applying *b*-value to fiber reinforced plastics structures

2.1 Introduction

As introduced in Chapter 1, the *b*-value is one of the major parameters used in acoustic emission (AE) analysis. This parameter is now widely used for integrity evaluation of concrete structures. The concept of the *b*-value originates from the field of earthquake seismology: the relationship between the magnitude of an earthquake (*M*) and the number of earthquakes larger than magnitude *M* can be expressed as the following empirical equations, known as the Gutenberg–Richter relations [2-1]:

$$\log_{10} N(M) = a - bM \,, \tag{2-1}$$

$$N(M) = \int_M^\infty n(M)\,dM \,, \tag{2-2}$$

where *M* is the magnitude of an earthquake, *n*(*M*) is the number of earthquakes with magnitude *M*, *N*(*M*) is the total number of earthquakes larger than magnitude *M,* and *a* and *b* are empirical constants. As seen in Equation (2-1), the logarithm of *N*(*M*) is proportional to *M*. The *b*-value is the negative gradient of this relationship and represents the slope of the magnitude distributions. For AE analysis, the Gutenberg–Richer relationship is modified to the following form:

$$\log_{10} N = a - b\left(\frac{dB_{AE}}{20}\right), \tag{2-3}$$

$$dB_{AE} = 20\log_{10}\left(\frac{A_1}{A_0}\right), \tag{2-4}$$

where A_0 is equal to 1 μV at the AE sensor output and A_1 is the peak voltage of the measured AE signal.

Micro-cracks with small AE amplitudes yield high *b*-values, whereas macro-cracks with large amplitudes produce relatively low values. Figure 2.1 explains the mechanism of changing *b*-value with the scale of fracture. When the level of damage to a structure approaches final fracture, the fracture behavior changes from micro-cracking to macro-cracking and the *b*-value becomes small [2.2]–[2.6]. This is the reason why the *b*-value is used for evaluation of the severity of damage to concrete structures.

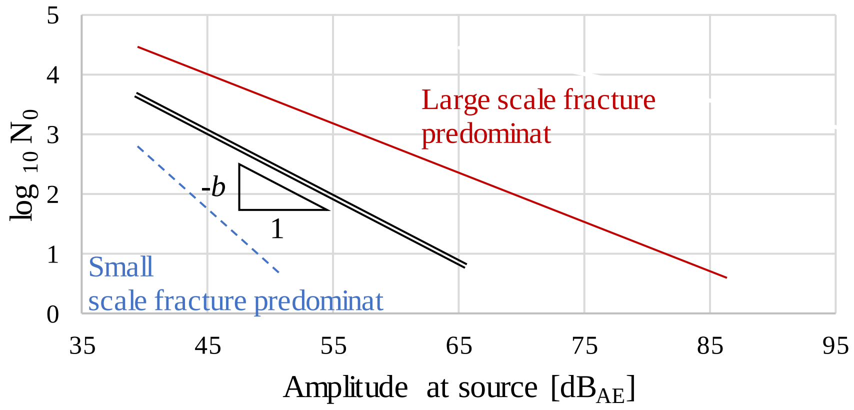

Figure 2.1 Definition of *b*-value for the modified Gutenberg–Richer relationship

This chapter discusses the applicability of the *b*-value to integrity evaluation of fiber-reinforced plastic (FRP) structures. It is well known that the frequency of AE signals generated from FRP is changed by fracture modes such as matrix cracking, fiber pull-out, and fiber fracture [2.7]–[2.9]. The effects of AE frequency on *b*-value have not yet been evaluated in detail. The purpose of this chapter is to clarify these effects using basic tensile testing of FRPs.

2.2 Acoustic emission monitoring during tensile testing

2.2.1 Specimens

As mentioned in Chapter 1, the frequency of AEs generated from FRPs depends on the nature of the fracture mode, such as matrix cracking, fiber pull-out, and fiber fracture. It is well known that the dominant fracture modes in FRPs during tensile test are affected by their stacking sequence. Table 2.1 shows the dominant fracture modes for tensile specimens with different stacking sequences for carbon-fiber-reinforced plastics (CFRP) based on literature data [2.7]–[2.9].

Table 2.1 Overview of relationships between staking sequence of carbon-fiber-reinforced plastics and dominant fracture modes (adapted from [2.7]–[2.9])

Stacking sequence		Matrix Cracking	Fiber pull-out	Fiber breakage
# 1 $[90]_1$	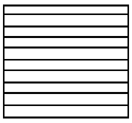	○	×	×
# 2 $[80]_1$	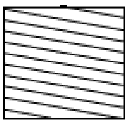	○	○	×
# 3 $[0]_1$	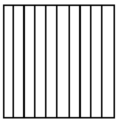	○	○	○
# 4 $[0/90]_2$	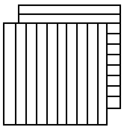	○	○	○
#5 Woven	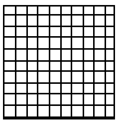	○	○	○

To investigate AE signals from different fracture modes and their influences on the *b*-value, CFRP with stacking sequences of $[90]_{16}$, $[80]_{16}$, $[0]_8$, and cross-ply $[0/90]_8$ were prepared. CFRP plates with 250 mm length and 150 mm width were prepared. They were pre-cured at 85 ˚C for 2 h, and then cured at 135 ˚C for 3 h under 0.7 MPa pressure. Rectangular plate specimens were prepared from these CFRP plates for tensile testing: their specifications, including length, width, and thickness, are shown in Table 2.2. Considering the differences in failure stress, the widths of specimens #3 and #4 were set to smaller than those of specimens #1 and #2. The diameter values shown in Table 2.2 are explained in Section 2.1.

Table 2.2 Specifications of carbon-fiber-reinforced plastic specimens

Units: mm

	Width	Length	Thickness	Diameter
# 1 $[90]_{16}$	20	200	3.6	4
# 2 $[80]_{16}$	20	200	3.6	4
# 3 $[0]_8$	16	200	1.8	6
# 4 $[0/90]_8$	16	200	1.8	6

Glass-fiber reinforced plastic (GFRP) plates of 220 mm length, 40 mm width, and 2.5 mm thickness were prepared. The plates contained woven glass fibers at an approximate fiber content of 50%. From these, rectangular plate specimens were prepared, the specifications of which are shown in Table 2.3. Because the failure stress was expected to be smaller than those of the CFRP specimens, wider specimens were prepared for GFRP.

Table 2.3 Specifications of glass-fiber-reinforced plastic specimens

Units: mm

	Width	Length	Thickness	Diameter
#5 Woven	40	250	2.5	6

b-Value analysis must be conducted using AE signals originating from a specific location. When damage occurs at various locations in a structure, the severity of damage differs for the different AE sources and separate *b*-value analyses must be conducted for each source. In this study, a center hole was introduced to concentrate the locations of the AE sources. The diameters of the holes are shown in Tables 2.2 and 2.3. Figures 2.2 and 2.3 show photographs of specimens after tensile testing. It is evident that the specimens broke from the center hole and that no damage occurred in other areas of the specimens. For this reason, it was unnecessary to determine the AE source location prior to the *b*-value analysis. Figure 2.2 also shows that the failure mechanisms changed with stacking sequence, as given in Table 2.1.

Figure 2.2 Carbon-fiber-reinforced plastic specimens after tensile testing

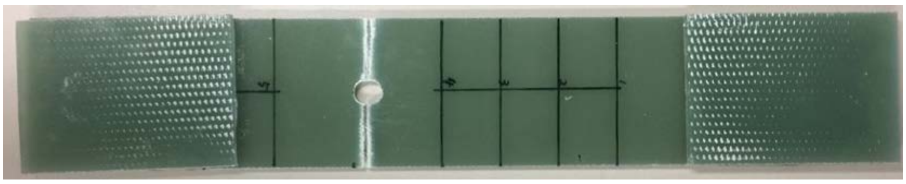

Figure 2.3 Glass-fiber-reinforced plastic specimens after tensile testing

Before each tensile test, 2.5-mm-thick GFRP tabs were attached to both ends of each specimen to avoid causing any damage from the jig. Four AE sensors (Physical Acoustics; Type: PICO) were mounted on each specimen using silicon grease and vinyl tape. Figure

2.4 shows the sensor locations, labeled as Sensors 1 to 4. Sensors 1 to 3 and 1 to 4 were mounted 10 mm from the center of the hole. A guard sensor was also attached to the left of the specimen, 10 mm from the tab (see Figure 2.4). Sensors 1 to 4 were used to investigate the influence of AE propagation distance on *b*-value; the guard sensor was used to distinguish AE from noise. The cross-head speed of the tensile tester was controlled at 0.1 mm/min. During each test, AE signals larger than 35 dB_{AE} were detected using a digitizer (Physical Acoustics; Type: PCI-2) at a sampling rate of 10 MHz per channel. Table 2.4 shows a summary of the monitoring conditions used for the AE testing.

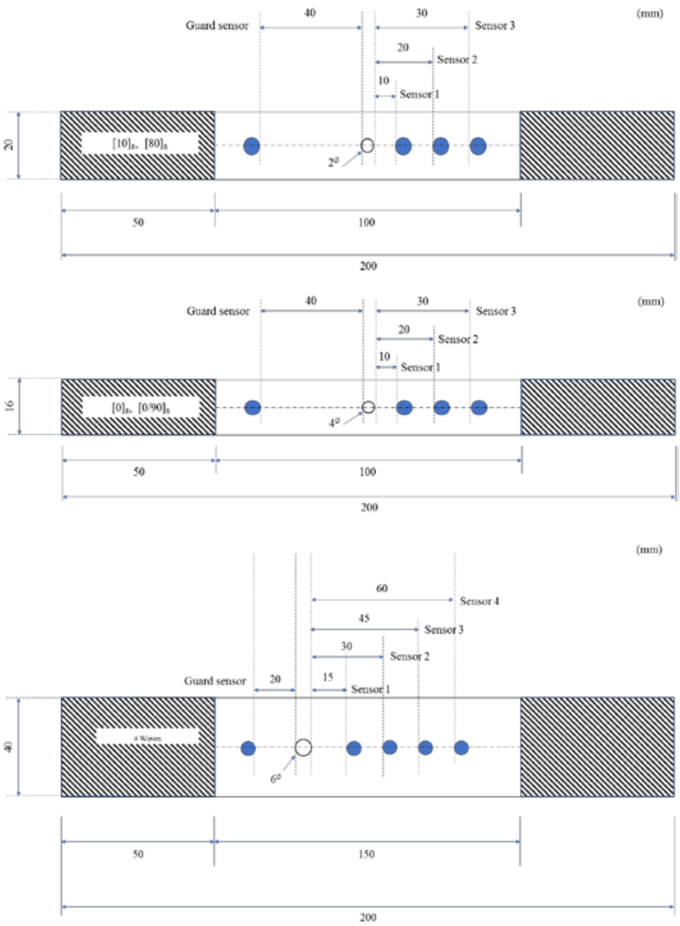

(a)

(b)

(c)

Figure 2.4 Schematic illustrations of fiber-reinforced plastic specimens with a centered hole and sensor locations. (a) $[10]_{16}$, $[80]_{16}$ carbon-fiber-reinforced plastic, (b) $[0]_8$, $[90]_8$ carbon-fiber-reinforced plastic, and (c) woven glass-fiber-reinforced plastic specimens

Table 2.4 Acoustic emission testing conditions

Threshold		Amplifier	Analog filter		Sampling conditions		
Type	dB_{AE}	dB_{AE}	Lower	Upper	Sampling rate	Pre-trigger	Length
Fixed	35	40	1 kHz	1 MHz	10 MHz	50 μsec	1 k

During AE testing, AE was detected by each sensor (including the guard sensor) when an event (fracture, noise) occurred. After testing, the AE signals measured by each sensor were clustered for each event. Signals detected during a period of 100 μs from the first-measured AE were considered to fall into the same cluster. After clustering, the AE signal amplitudes in same cluster were compared to distinguish AE from noise. When the amplitude of AE detected by Channel 1 (Ch 1; the nearest channel from the center hole) was the largest, the signals in this cluster were used for *b*-value analysis, otherwise the signals in this cluster were excluded from analysis because they may have been caused by noise.

2.3 *b*-Value analysis for various fiber-reinforced plastic specimens and propagation distances

Table 2.5 summarizes the experimental results, including total test time, failure stress and strain, time at which the first AE signals were detected, total number of AE hits, and maximum AE amplitude. As shown, the failure stresses and strains of the CFRP specimens (#1[90]$_8$, #2[80]$_8$, #3[0]$_8$, and #4[0/90]$_8$) rapidly decreased with increase in the fiber angle. The tensile stress of the woven GFRP fiber specimen (#5) was greater than that of the #1 and #2 CFRP specimens. All specimens generated large amplitudes of AE (100 dB$_{AE}$) during the last stage of tensile testing. The total number of AE hits increased in order: #1[90]$_{16}$ < #2[80]$_{16}$ < #3[0]$_8$ < #4[0/90]$_8$ = #5 woven GFRP. A partial reason may be related to the number of fracture modes available for each of these specimen types (see Table 2.1).

Table 2.5 Summary of experimental results

	Total test time	Failure stress	Failure strain	1st AE hit	Total AE hits	Max. Amp.
	[sec.]	[MPa]	[%]	[sec.]		dB$_{AE}$
#1 [0]$_{16}$	522	16.7	0.35	376	137	99
# 2 [80]$_{16}$	581	22.6	0.58	319	116	99
# 3 [0]$_8$	594	1275	4.1	52	6394	99
# 4 [0/90]$_8$	490	834	4	36.1	10282	99
#5 Woven	2064	234	2.7	106	12398	99

Figures 2.5 to 2.9 show the AE results for tensile testing of the #1[90]$_{16}$, #2[80]$_{16}$, #3[0]$_8$, #4[0/90]$_8$ CFRP, and #5 woven GFRP specimens, respectively, as detected by Sensor 1. The horizontal axes of all figures represent the specimen life time, which was defined as 100% for the time of final failure. The (a) figures show AE amplitude (maximum value of an AE waveform with a single emission, in dB$_{AE}$) detected during each test (marked

by ∗). Change in stress is superimposed on each graph (black lines). The (b) figures show cumulative AE hits (marked by double lines).

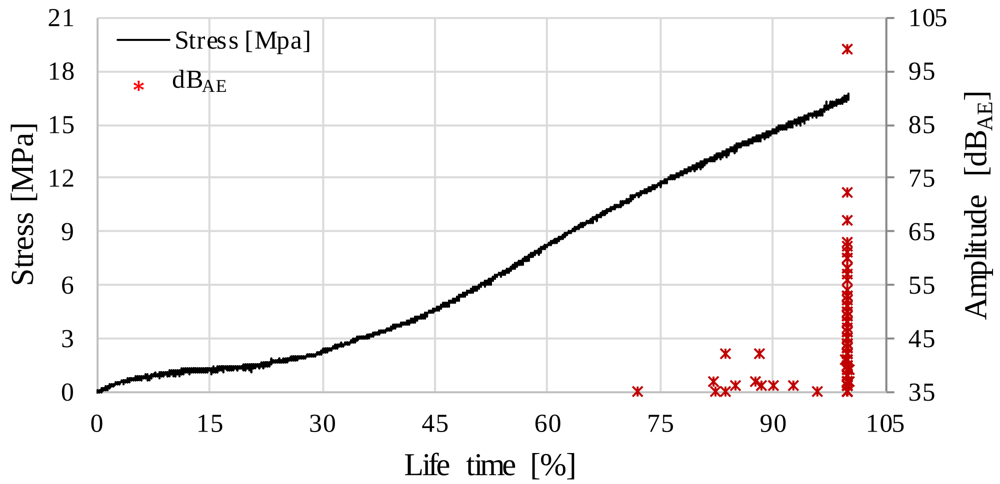

(a)

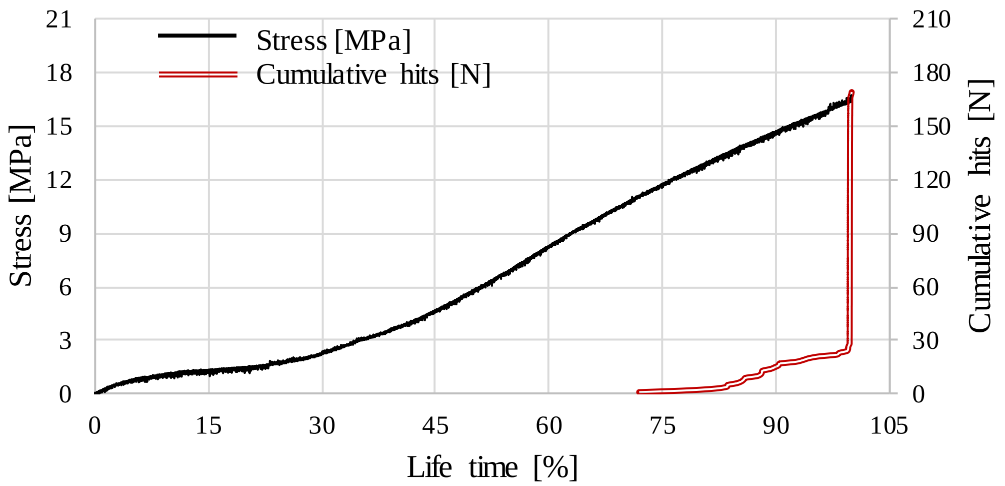

(b)

Figure 2.5 Variation in stress with (a) change in amplitude and (b) cumulative hits with life time for #1[90]$_8$ specimens under tensile test. Stress history is superimposed (black line)

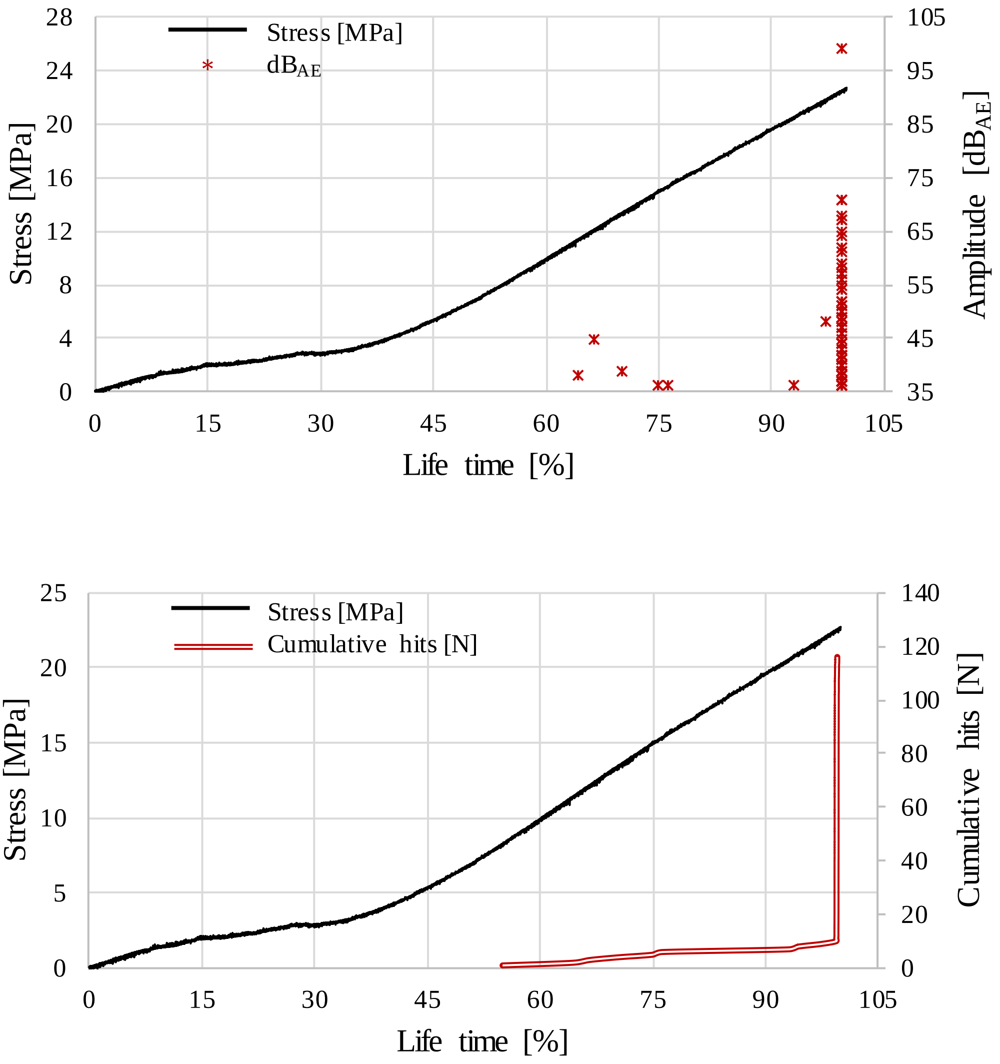

(a)

(b)

Figure 2.6 Variation in stress with (a) change in amplitude and (b) cumulative hits with life time for #2[80]$_{16}$ specimens under tensile test. Stress history is superimposed (black line)

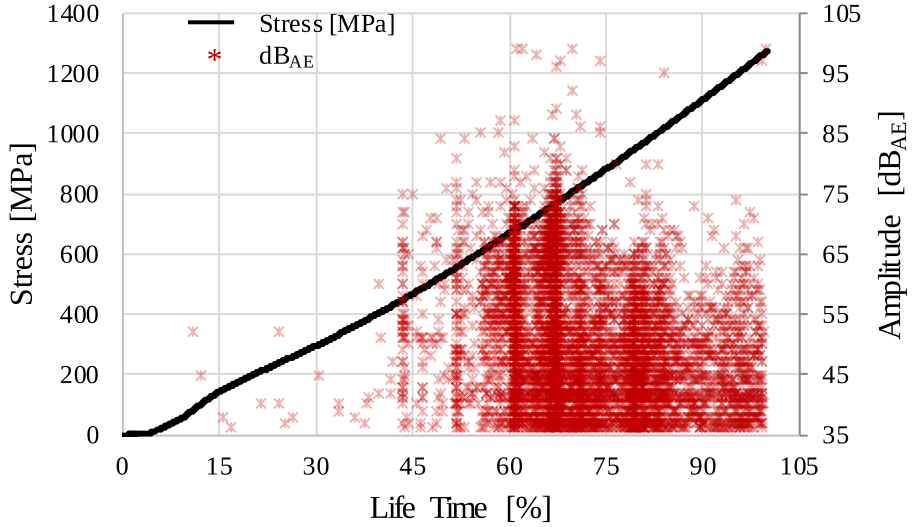

(a)

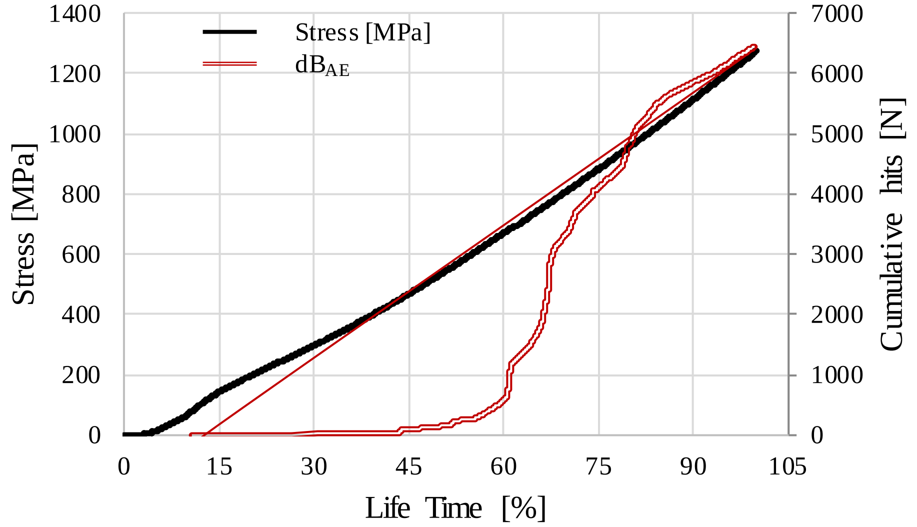

(b)

Figure 2.7 Variation in stress with (a) change in amplitude and (b) cumulative hits with life time for #3[0]$_8$ specimens under tensile test. Stress history is superimposed (black line)

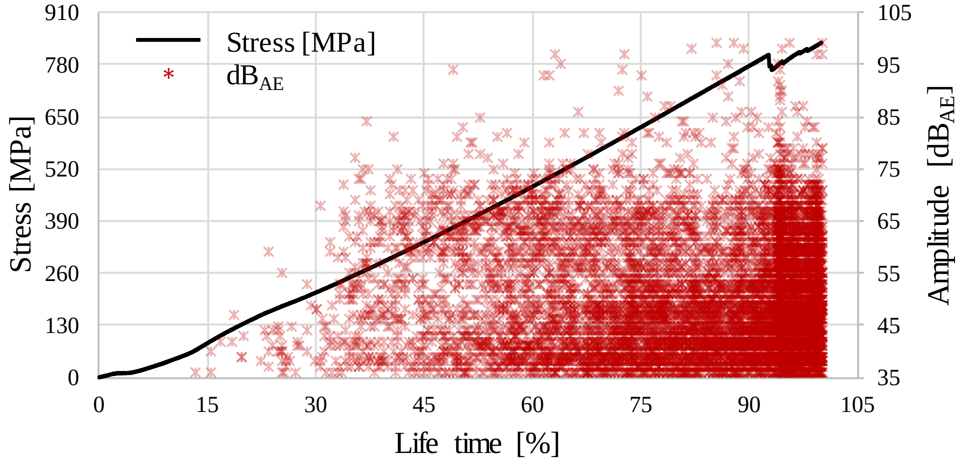

(a)

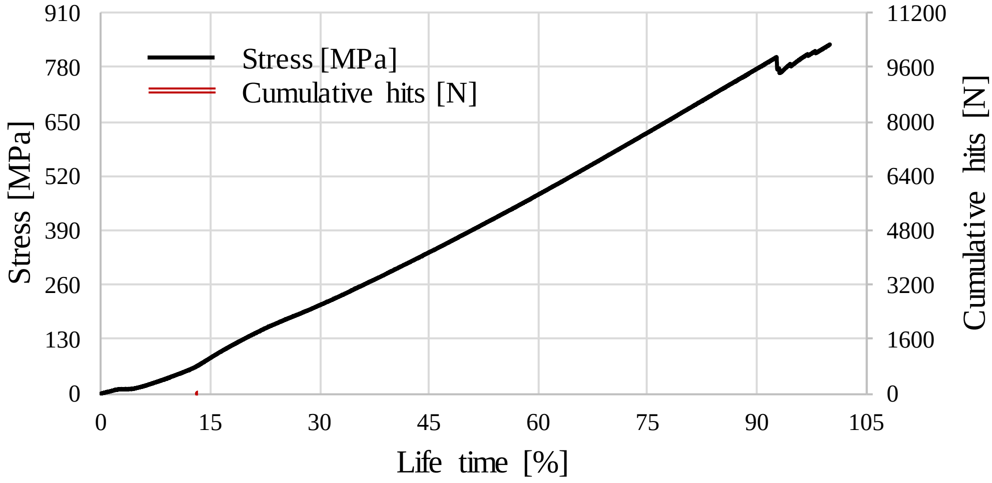

(b)

Figure 2.8 Variation in stress with (a) change in amplitude and (b) cumulative hits with life time for #4[0/90]$_8$ specimens under tensile test. Stress history is superimposed (black line)

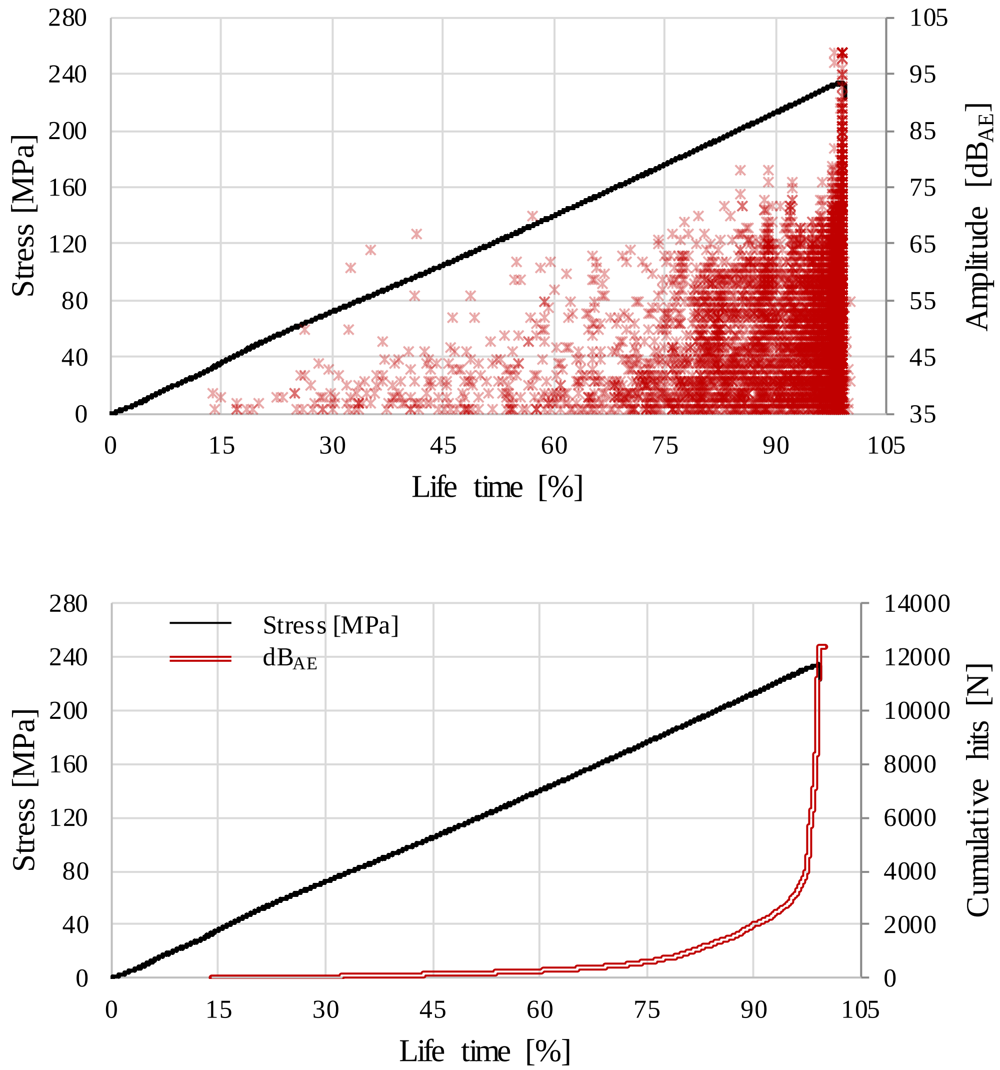

(a)

(b)

Figure 2.9 Variation in stress with (a) change in amplitude and (b) cumulative hits with life time for #5 woven GFRP specimens under tensile test. Stress history is superimposed (black line)

AE amplitude distribution gives a unique trend corresponding to the degree of damage. Both the amplitude (a) and cumulative hits (b) changed according to the characteristics of the fractures. For example, micro-cracks generated a large number of hits with small amplitude from the initial stage of a tensile test; in contrast, fiber breakages generated a small number of hits with large AE amplitude in the final stage of the test. This behavior is discussed in detail in Chapter 3.

Figures 2.10 to 2.14 show amplitude distributions of all AE signals for specimens #1 to #5, as detected by Sensors 1 to 3 for specimens #1 to #4 and Sensors 1 to 4 for specimen #5. The horizontal axes show AE amplitude in units of dB_{AE}; the vertical axes show the total number of AE hits at each amplitude.

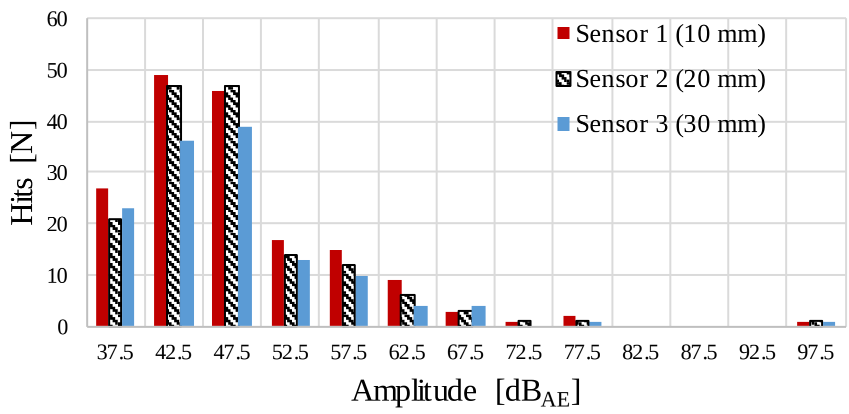

Figure 2.10 Amplitude distributions for #1[90]$_{16}$ specimen. (AE signal propagation distances to Sensors 1 to 3 are 10, 20, and 30 mm, respectively)

Figure 2.10 shows the amplitude distributions for the #1[90]$_{16}$ specimen: only matrix cracking occurred and all AE sources exhibited matrix cracking; the number of hits decreased with increasing amplitude. This result resembles that of AE testing of concrete structures. In contrast, the amplitude distributions showed several peaks at specific amplitudes when the AE sources included various fracture modes (see Figures 2.11, 2.12, 2.13, and 2.14). This phenomenon may be caused by combinations of AE signals originating from sources generated by different fracture modes, as discussed in detail in Chapter 3.

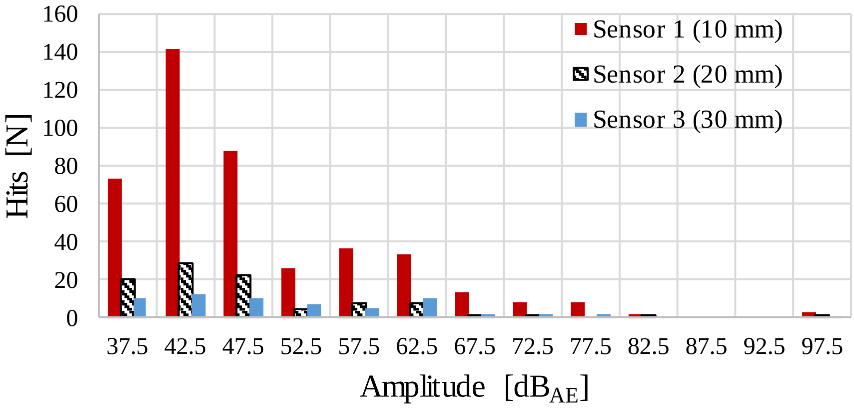

Figure 2.11 Amplitude distributions for #2[80]$_{16}$ specimen. (Acoustic emission signal propagation distances for Sensors 1 to 3 were 10, 20, and 30 mm, respectively)

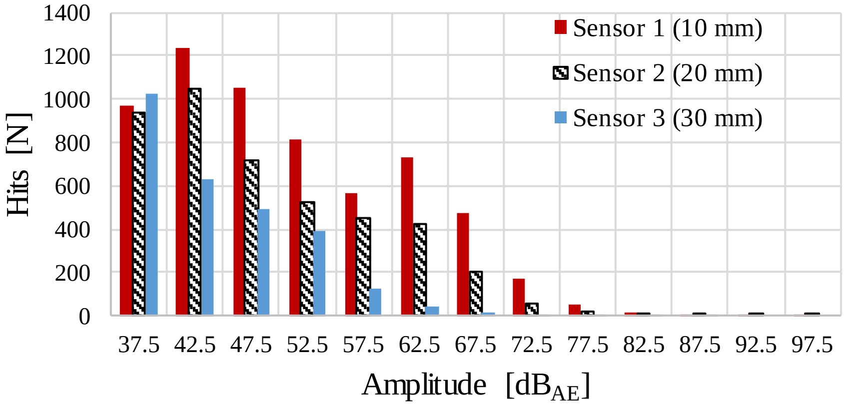

Figure 2.12 Amplitude distributions for #3[0]$_8$ specimen. (Acoustic emission signal propagation distances for Sensors 1 to 3 were 10, 20, and 30 mm, respectively)

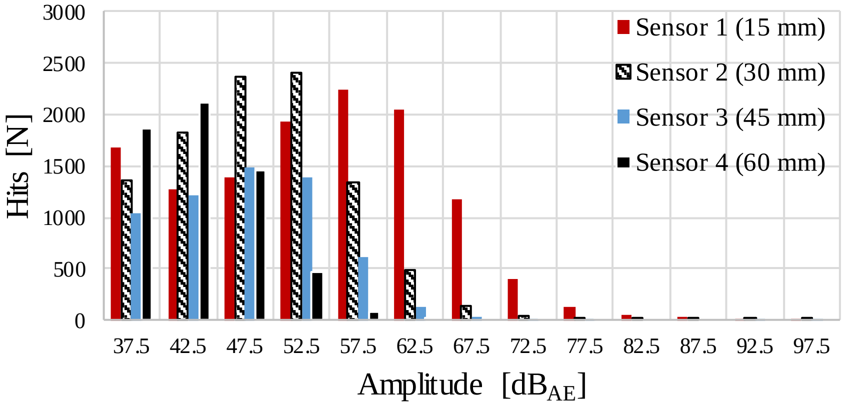

Figure 2.13 Amplitude distributions for #5 woven GFRP specimen. (Acoustic emission signal propagation distances for Sensors 1 to 4 were 15, 30, 45, and 60 mm, respectively)

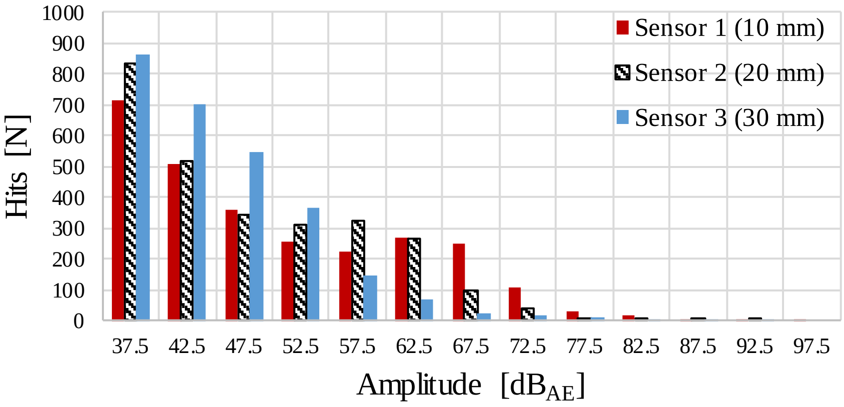

Figure 2.14 Amplitude distributions for #4 [0/90]8 specimen. (Acoustic emission signal propagation distances for Sensors 1 to 3 were 10, 20, and 30 mm, respectively)

Figures 2.15 to 2.19 show the relationships between the logarithm of cumulative hits and amplitude, constructed from the data in Figures 2.10 to 2.14. Experimental data were approximated by the lines shown in the figures. The experimental data for Figures 2.17 to 2.19 were difficult to fit linearly: this behavior is discussed in detail in Chapter 3. The AE signals in Figure 2.15 were mainly caused by matrix cracking; those in Figure 2.16 were attributed to matrix cracking and fiber pull-out; those in Figures 2.17 to 2.19 were caused by several fracture modes, as described in Section 2.1. As shown in Figure 2.15, the distributions of the cumulative hits changed with propagation distance, although the slopes of the fitted lines (*b*-values) barely changed (Sensor 1: 0.040; Sensor 2: 0.039; Sensor 3: 0.038). This result indicated that the *b*-value was unchanged by propagation distance when detected AE signals were caused by only matrix cracking; however, when the AE source contained multiple fracture modes, both the amplitude distribution and slope of the fitted line changed with propagation distance, thereby changing the *b*-value (unlike the *b*-value of specimen #1 or that of general concrete structures). These results demonstrated that the general *b*-value cannot be used for evaluation of severity of damage of FRPs without considering the propagation distance of the AE signals.

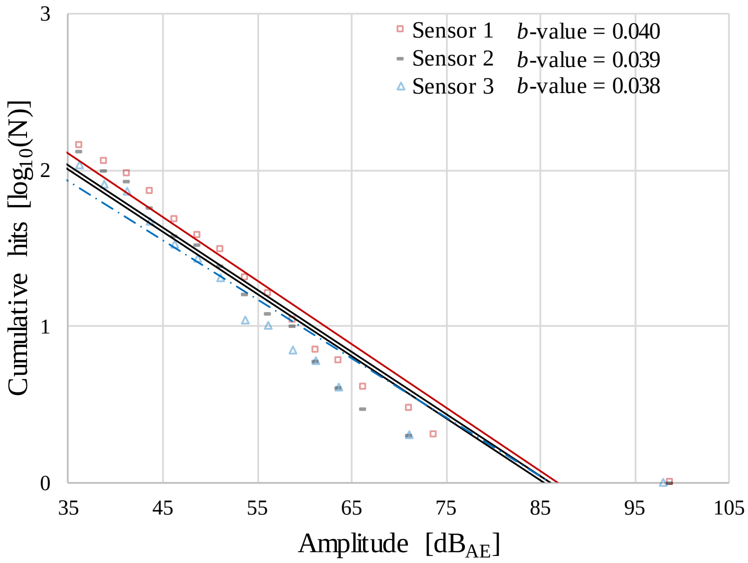

Figure 2.15 Plots of cumulative hits as a function of acoustic emission signal amplitude for tensile testing of $\#1[90]_{16}$ specimen. *b*-Values determined by fitted lines are shown. (Acoustic emission signal propagation distances for Sensors 1 to 3 were 10, 20, and 30 mm, respectively)

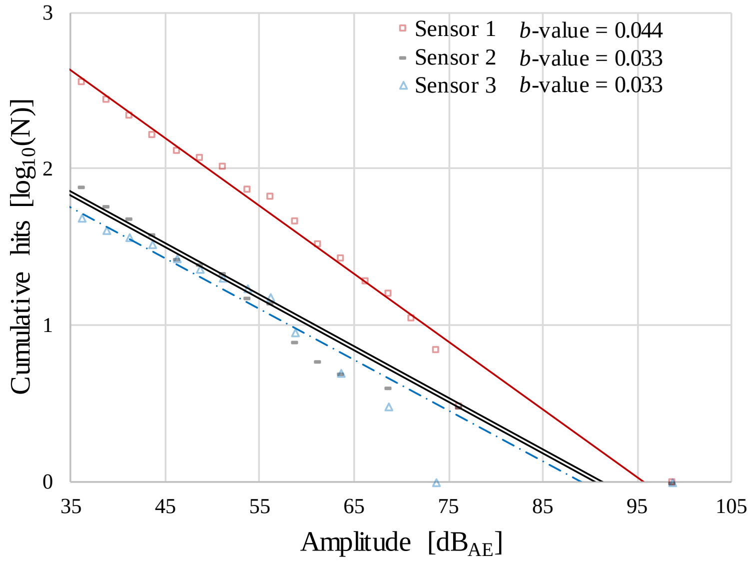

Figure 2.16 Plots of cumulative hits as a function of acoustic emission signal amplitude for tensile testing of #2[80]$_{16}$ specimen. *b*-Values determined by fitted lines are shown. (Acoustic emission signal propagation distances for Sensors 1 to 3 were 10, 20, and 30 mm, respectively)

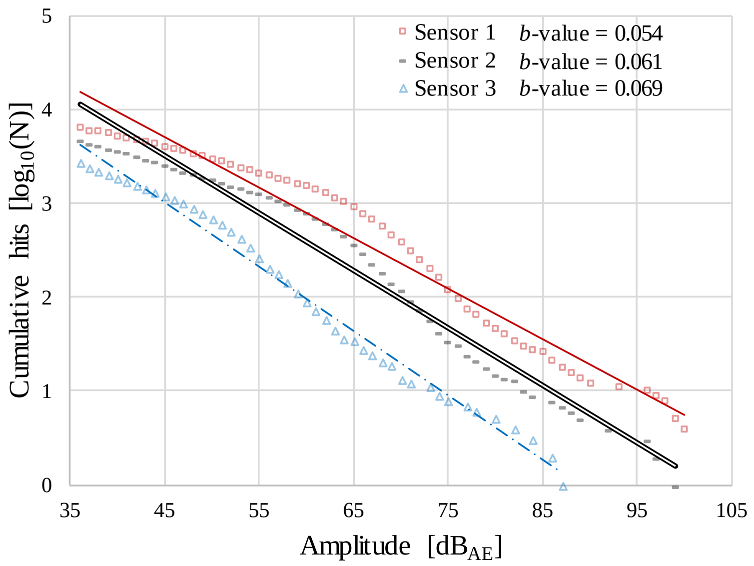

Figure 2.17 Plots of cumulative hits as a function of acoustic emission signal amplitude for tensile testing of #3[0]$_8$ specimen. *b*-Values determined by fitted lines are shown. (Acoustic emission signal propagation distances for Sensors 1 to 3 were 10, 20, and 30 mm, respectively)

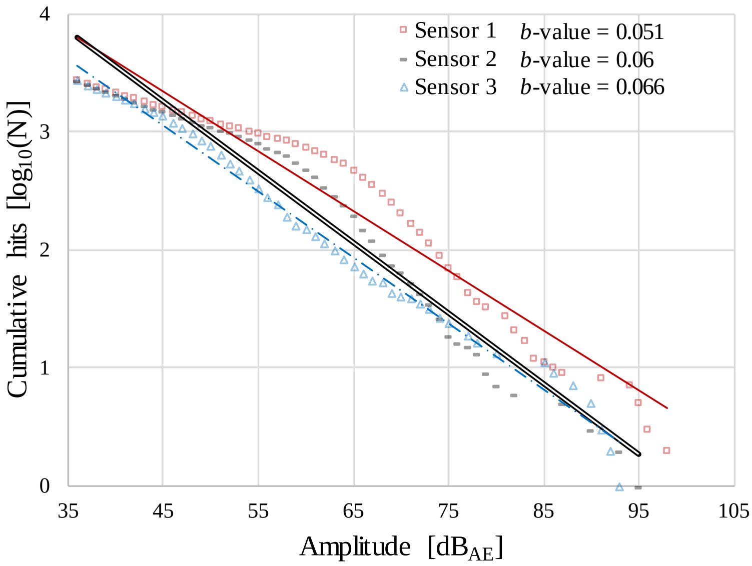

Figure 2.18 Plots of cumulative hits as a function of acoustic emission signal amplitude for tensile testing of #4[0/90]$_8$ specimen. *b*-Values determined by fitted lines are shown. (Acoustic emission signal propagation distances for Sensors 1 to 3 were 10, 20, and 30 mm, respectively)

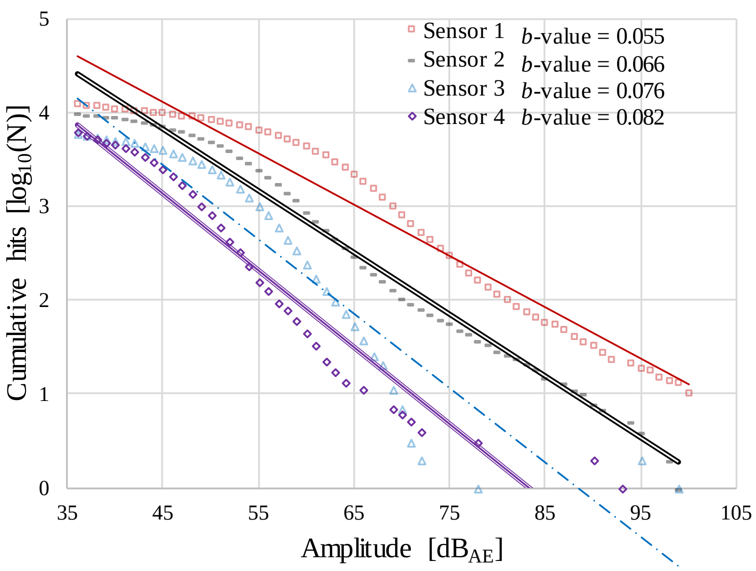

Figure 2.19 Plots of cumulative hits as a function of acoustic emission signal amplitude for tensile testing of #5 woven GFRP specimen. *b*-Values determined by fitted lines are shown. (Acoustic emission signal propagation distances for Sensors 1 to 4 were 15, 30, 45, and 60 mm, respectively)

2.4 Conclusions

This chapter discussed the applicability of using the *b*-value to evaluate the severity of damage to various FRP specimens. Tensile tests of CFRPs with several stacking sequences and of GFRP with woven fiber were conducted. AE signals originating from a hole in the center of the specimens were detected by several AE sensors located at different distances from the hole. The following points summarize the main findings.

#1 $[90]_{16}$ specimen:

1. Almost all AE signals were generated by matrix cracking.
2. The number of AE hits decreased with increasing amplitude of AE.
3. The *b*-value was unaffected by the propagation distance of AE.
4. When FRP exhibits only matrix cracking, the *b*-value can be used for evaluation of the severity of damage using the general method of AE analysis that is used in assessing concrete structures.

Other specimens:

5. AE signals were generated by several fracture modes, including matrix cracking, fiber pull-out, and fiber breakage.
6. The distribution of AE amplitudes showed several peaks at specific amplitudes. This phenomenon may be caused by mixtures of AE signals generated by different fracture modes.
7. The *b*-value changed with AE propagation distance.
8. When FRP exhibits several fracture modes, the general *b*-value cannot be used for evaluation of severity of damage without considering the distance of propagation of the AE signals.

2.5 References

[2-1] Gutenberg, B., and Richter, C.F. "Magnitude and energy of earthquakes." Annals of Geophysics 9.1 (1956): 1-15.

[2-2] Colombo, I.S., Main, I.G., Forde, M.C.: Assessing Damage of Reinforced Concrete Beam Using "*b*-value" Analysis of Acoustic Emission Signals. J. Mater. Civ. Eng. 15, 280–286 (2003). doi:10.1061/(ASCE)0899-1561(2003)15:3(280)

[2-3] Shiotani, T., Fujii, K., Aoki, T., Amou, K.: Evaluation of progressive failure using AE sources / Improved *b*-value on slope model tests. Prog. Acoust. Emiss. VII, 529–534 (1994)

[2-4] Rao, M.V.M.S., Lakshmi, K.J.P.: Analysis of *b*-value and improved *b*-value of acoustic emissions accompanying rock fracture. Curreent Sci. 89, 1577–1582 (2005)

[2-5] Sagar, R.V., Prasad, B.K.R., Kumar, S.S.: An experimental study on cracking evolution in concrete and cement mortar by the *b*-value analysis of acoustic emission technique. Cem. Concr. Res. 42, 1094–1104 (2012). doi:10.1016/j.cemconres.2012.05.003

[2-6] Zitto, M.E., Piotrkowski, R., Gallego, A., Sagasta, F., Benavent-Climent, A.: Damage assessed by wavelet scale bands and *b*-value in dynamical tests of a reinforced concrete slab monitored with acoustic emission. Mech. Syst. Signal Process. 60, 75–89 (2015). doi:10.1016/j.ymssp.2015.02.006

[2.7] de Groot, P.J., Wijnen, P.A.M., Janssen, R.B.F.: Real-time frequency determination of acoustic emission for different fracture mechanisms in carbon/epoxy composites. Compos. Sci. Technol. 55, 405–412 (1995). doi:10.1016/0266-3538(95)00121-2

[2.8] Ramirez-Jimenez, C.R., Papadakis, N., Reynolds, N., Gan, T.H., Purnell, P., Pharaoh, M.: Identification of failure modes in glass/polypropylene composites by means of the primary frequency content of the acoustic emission event. Compos. Sci. Technol. 64, 1819–1827 (2004). doi:10.1016/j.compscitech.2004.01.008

[2.9] Gutkin, R., Green, C.J., Vangrattanachai, S., Pinho, S.T., Robinson, P., Curtis, P.T.: On acoustic emission for failure investigation in CFRP: Pattern recognition and peak frequency analyses. Mech. Syst. Signal Process. 25, 1393–1407 (2011). doi:10.1016/j.ymssp.2010.11.014

Chapter 3 Cause of changes in *b*-value with propagation distance

3.1 Introduction

Chapter 2 showed that the *b*-value changed with propagation distance of an acoustic emission (AE) signal when several failure modes (such as matrix cracking, fiber pull-out, and fiber breakage) occurred in same location in fiber-reinforced plastics (FRPs); however, the cause of such changes was unclear. It is well known that the features of AE signals, such as range of frequency and amplitude, change with different FRP failure modes [3.1]–[3.6]. Groot et al. [3.3] detected AE signals generated by specific failure modes by double cantilever beam (DCB), lap shear, and 0^{o}, 10^{o}, and 90^{o} tensile tests. They concluded that the amplitude and frequency of AE signals are changed by different fracture modes. Ramirez-Jimenez et al. [3.4] prepared glass–polypropylene tensile test specimens with several stacking sequences and also reported that the frequency ranges of AE signals were changed by the fracture modes. Gutkin et al. [3.5], [3.6] also found that the frequency distribution of AE signals recorded in several tests with various fiber stacking sequences of carbon-fiber-reinforced plastics (CFRPs) using pattern recognition techniques was dependent on the fracture type (matrix cracking: 0–50 kHz; fiber pull-out: 200–300 kHz; delamination: 50–100 kHz; fiber fracture: 400–500 kHz). These results show that FRPs generate a wider frequency band of AE signals compared with those from Earth's crust, rock formations, and engineering concrete [3.7]–[3.15].

The amplitude of AE detected by a sensor located far from an AE source is considerably lower than the amplitude that would have been observed near the source. This is due to wave attenuation, i.e., the loss in energy of the wave through absorption and scattering

[3.16], [3.17]. The amplitude of an AE signal, $A_1(\omega, r)$, in a plate located at distance r from the source can be calculated from Equation (3-1) using the attenuation factor $\alpha(\omega)$ and amplitude at the source $A_0(\omega)$. It is noted that the attenuation factor α is a function of ω: higher frequencies incur higher attenuation than lower frequencies.

$$A_1(\omega, r) = A_0(\omega) \cdot \frac{1}{\sqrt{r}} \cdot \exp[-\alpha(\omega) \cdot r] \quad (3.1)$$

This chapter reports an investigation of the frequencies of AE signals detected during CFRP tensile tests and the frequency dependence of the *b*-values. The cause of changes in the *b*-value is discussed using a parametric study of AE signals with various centroid frequencies. Based on AE signals detected during tensile testing of a glass-fiber-reinforced plastic (GFRP), the amplitudes of AE signals at different propagation distances were simulated and the value of *b* estimated with changing propagation distance.

3.2 Features of acoustic emission signals from carbon-fiber-reinforced plastic specimens

Figure 3.1 shows the time series of *b*-values during tensile testing of cross-ply #4$[0/90]_8$ CFRP specimens. The *b*-values were calculated from AE signals detected by Sensor 1 (10 mm from the source; blue dotted line), Sensor 2 (20 mm; black double line), and Sensor 3 (30 mm; red line). The stress history is superimposed on this graph, shown in the black line. The dimensions of the specimen and AE sensor locations are shown in Figure 2.4 in Chapter 2. *b*-Values from all sensors fluctuated with time during the test. As noted in Chapter 2, the *b*-values changed with propagation distance. Figure 3.1 shows how the magnitudes of the differences between the three sensors changed with time.

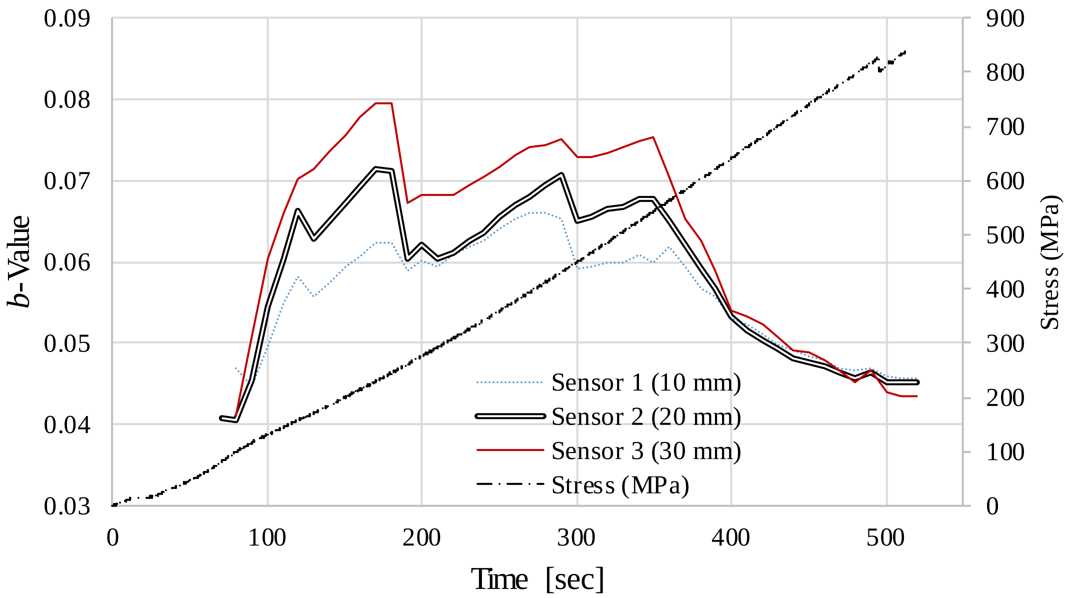

Figure 3.1 Changes in *b*-values for Sensors 1 to 3 with time during tensile testing of #4$[0/90]_8$ specimen

Figure 3.2 shows the number of AE hits at the centroid frequency for the #4$[0/90]_8$ specimens. Sensors 1 to 3 detected same AE origin, although their distributions differed. AE signals ranging from 340 to 540 kHz were dominant for Sensor 1 (propagation length:

10 mm); dominant frequencies for Sensor 3 (propagation length: 30 mm) varied from 340 to 470 kHz. Changes in dominant frequency with propagation length may change the *b*-value.

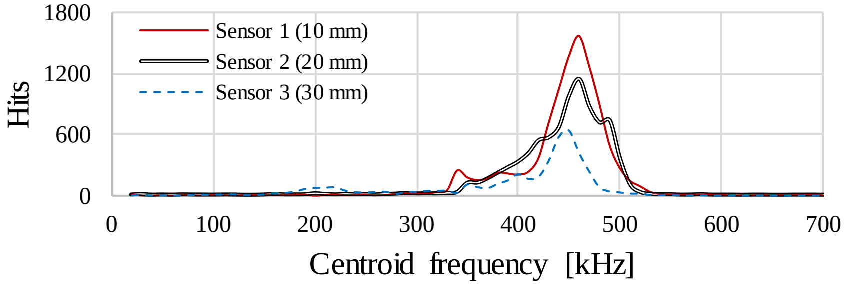

Figure 3.2 Acoustic emission hits as a function of centroid frequency for cross-ply CFRP #4[0/90]$_8$ tensile test specimens

Figure 3.3(a), (b), and (c) show the number of AE hits detected by Sensor 1 at the centroid frequency for the #1[90]$_{16}$, #2[80]$_{16}$, and #3[0]$_8$ specimens, respectively. As described in Table 2.1 in Chapter 2, the dominant AEs in Figure 3.3(a) were caused by matrix cracking; those in Figure 3.3(b) were caused by matrix cracking and fiber pull-out; and those in Figure 3.3(c) by matrix cracking, fiber pull-out, and fiber breakage. Comparing these results, the dominant frequencies for matrix cracking, fiber pull-out, and fiber breakage were confirmed as 100–250 kHz, 350–540 kHz, and 550–660 kHz, respectively. The dominant frequencies for each fracture mode exhibited by the cross-ply #4[0/90]$_8$ specimens were then separated by band-pass frequency filters of 100–250 kHz, 450–550 kHz, and 550–650 kHz. Figure 3.4(a), (b), and (c) show these results; Figure 3.4(d) is reproduced from Figure 2.18 for comparison and shows the AE data before filtering. As shown in Figure 3.4(a) (matrix cracking) and (b) (fiber pull-out), the slopes of each line (negative of *b*-value) were almost independent of distance; that of Figure 3.4(c) was little changed when compared with that in Figure 3.4(d) (before filtering), which may be caused by AE signals arising from a mixture of fiber pull-out and fiber breakage fracture modes. The *b*-value was almost unchanged by propagation distance when the detected AE signals were caused by certain fracture modes.

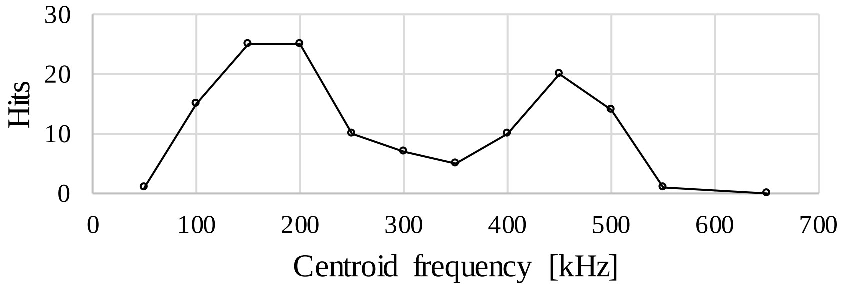

(a)

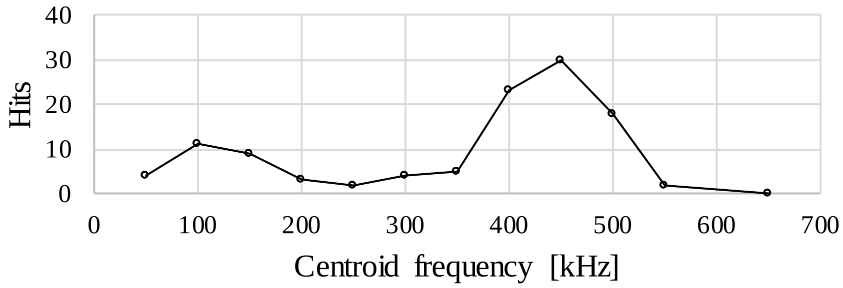

(b)

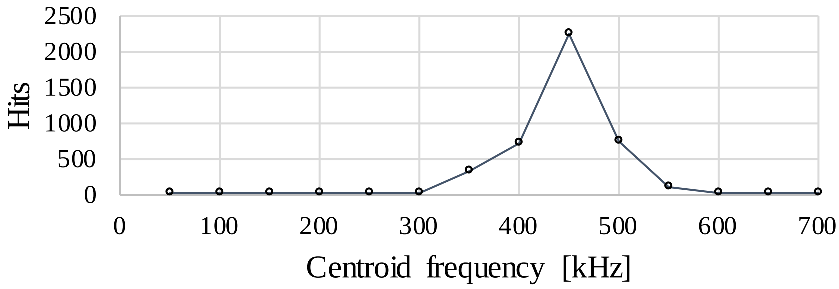

(c)

Figure 3.3 Acoustic emission hits as a function of centroid frequency for (a) #1$[90]_{16}$ (matrix cracking), (b) #2$[80]_{16}$ (matrix cracking and fiber pull-out), and (c) #3$[0]_{8}$ (matrix cracking, fiber pull-out, and fiber breakage) specimens

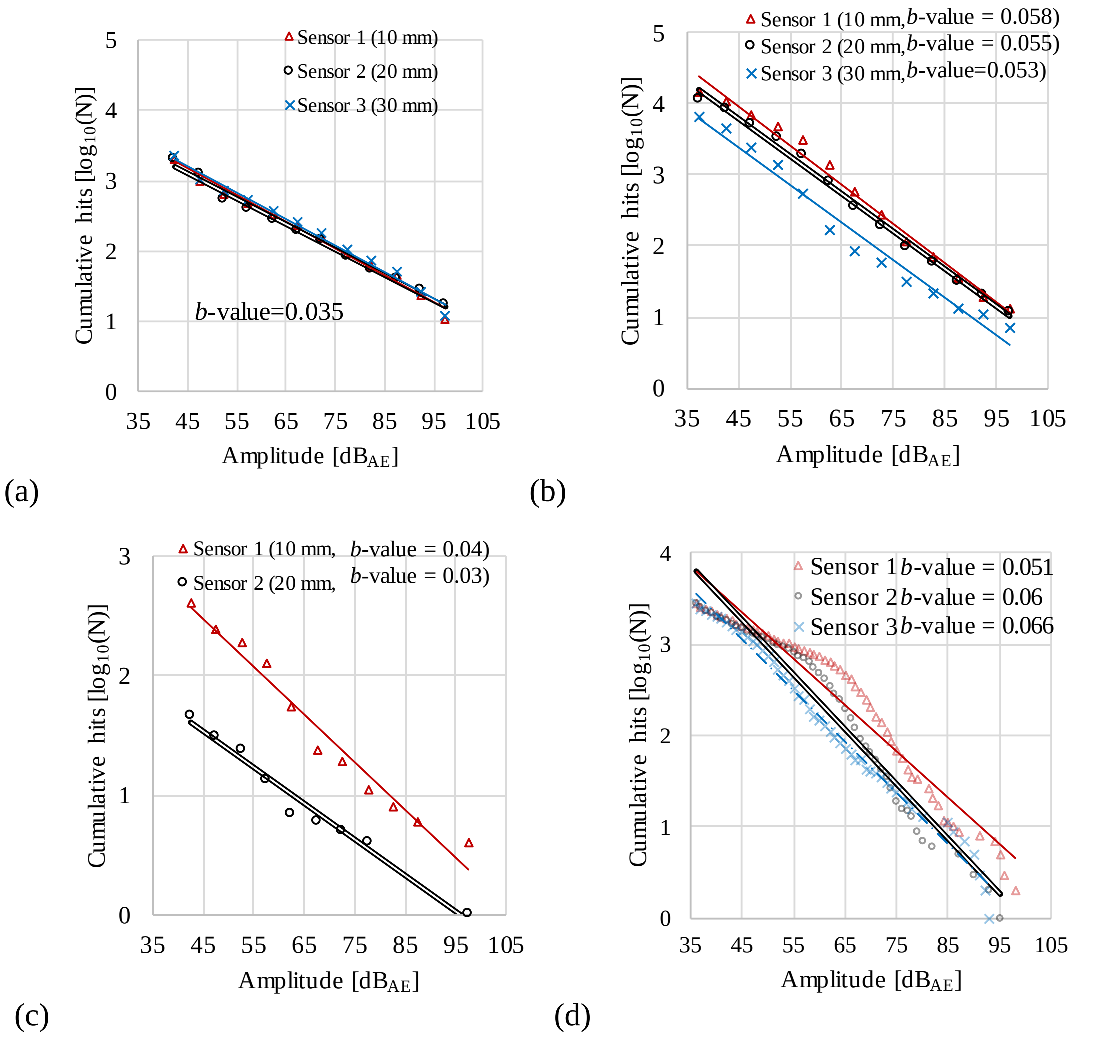

Figure 3.4 Cumulative amplitude distributions of each frequency component according to fracture mode. (a) 100–250 kHz (matrix cracking), (b) 350–550 kHz (fiber pull-out), (c) 550–650 kHz (fiber breakage), and (d) total acoustic emission signal (all failure modes)

To determine the cause of the change in *b*-value with propagation distance, the cumulative amplitude distributions of each frequency component were investigated according to the fracture mode. Figure 3.5 shows the cumulative hits by amplitude for each fracture mode for different AE propagation distances. The cumulative number of AE hits for all AE signals is also shown (symbol: ◯).

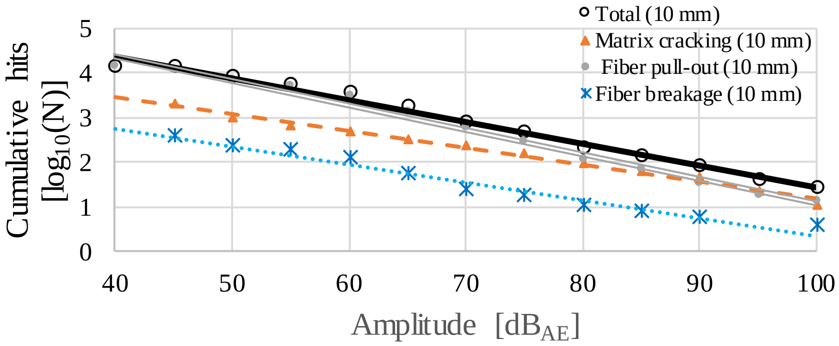

(a)

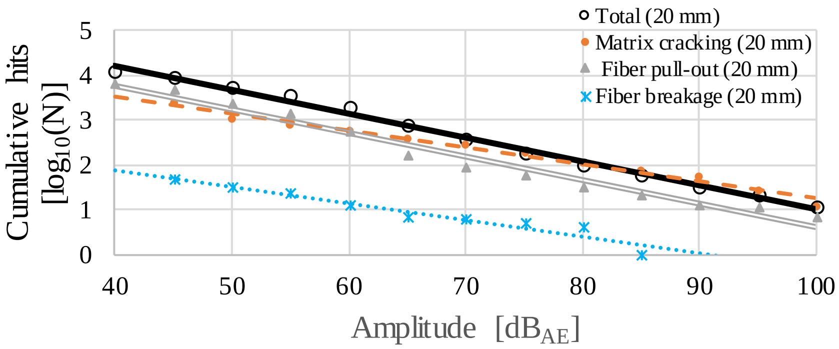

(b)

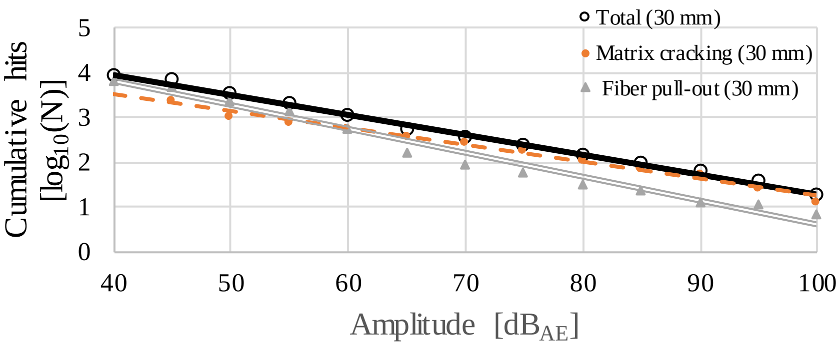

(c)

Figure 3.5 Cumulative amplitude distributions of each frequency component according to fracture mode (matrix cracking: 100–250 kHz; fiber pull-out: 350–550 kHz; fiber breakage: 550–650 kHz) for propagation distances of (a) 10 mm (Sensor 1), (b) 20 mm (Sensor 2), and (c) 30 mm (Sensor 3)

The slope of the fitted line representing all AE sources (◯) at a propagation distance of 10 mm [Figure 3.5(a)] is composed of all frequency components: 100–250 kHz (matrix cracking); 450–550 kHz (fiber pull-out); and 550–650 kHz (fiber breakage). The negative slope of the line (*b*-value) was 0.051, which differs from that of each individual frequency source (100–250 kHz: 0.035; 450–550 kHz: 0.058; 550–650 kHz: 0.04). Owing to the frequency dependence of attenuation (high attenuation factor for high frequency components), the number of high-frequency AE signals attributed to fiber breakage (550–650 kHz) was significantly reduced for propagation distances of 20 and 30 mm [Figure 3.5(b) and (c)]; however, the slope representing the distribution of all AE sources (◯) at a propagation distance of 30 mm were primarily dominated by the 100–250 kHz (matrix cracking) and 450–550 kHz (fiber pull-out) components. From these results, it is evident that a change in *b*-value may be caused by a change in the proportion of each frequency component after propagation that can be attributed to the frequency dependence of the AE attenuation.

Because propagation distance affected the *b*-value for CFRP, we focused on a propagation length of 10 mm to determine its failure evolution based on analysis of the *b*-value. Figure 3.6 shows a time series of *b*-values during tensile testing originating from all AE (black double line), those from matrix cracking only (dashed line: 100–250 kHz), fiber pull-out only (red dotted line: 450–550 kHz), and fiber breakage alone (red solid line: 550–650 kHz). The narrow black line with triangle symbols indicates the prevailing stress during the test. It was apparent that matrix cracking and fiber pull-out were the dominant fracture modes for the first 270 s, but, thereafter, fiber breakage also contributed. When the damage to the CFRP specimens approached final fracture, the dominant fracture behavior changed from matrix cracking and fiber pull-out to fiber breakage; each *b*-value then changed significantly.

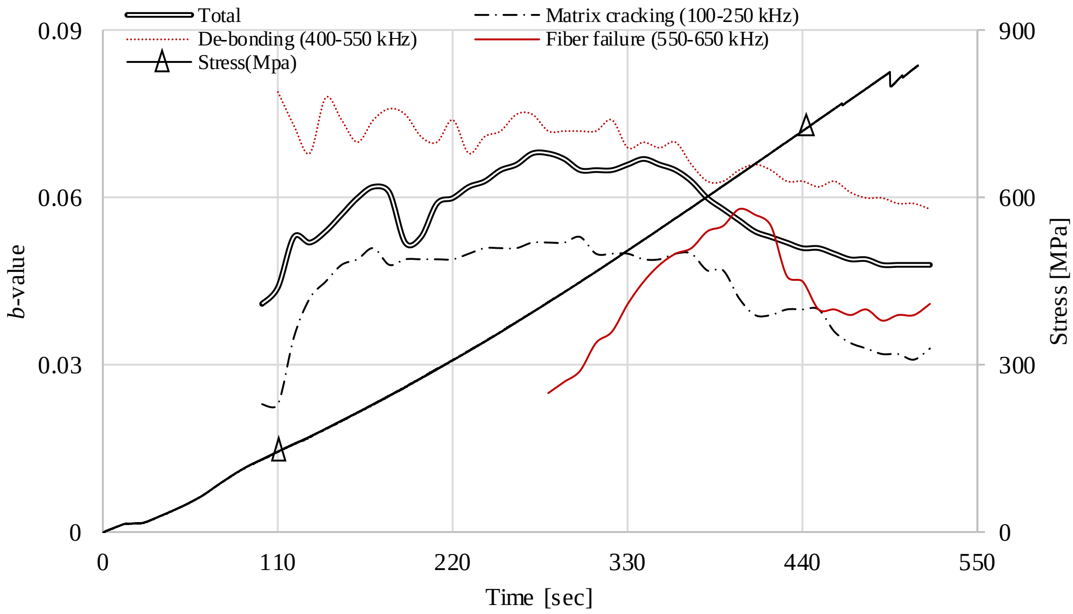

Figure 3.6 Changes in *b*-values for all acoustic emission sources (50–650 kHz) and the individual contributions from matrix cracking (100–250 kHz), fiber pull-out (350–550 kHz), and fiber breakage (550–650 kHz)

3.3 Parametric study of *b*-values of acoustic emission with multiple frequencies

A parametric study of the *b*-value was then conducted to clarify the cause of changes in the *b*-value. AE signals with frequencies of 150, 250, and 500 kHz were assumed to be generated at the same AE source and detected at distances of 30, 100, 300, and 500 mm from the source. Attenuations of these three frequencies were assumed to be 0.015, 0.058, and 0.116 Np/mm, respectively, and their cumulative hit distributions by amplitude were set as shown in Figure 3.7, where the vertical axis is the logarithm of the cumulative number of AE hits. The total number of AE signals for each frequency was set to 10 000. A total number of 30 000 AE signals were then assumed to be generated in this simulation. As shown in Figure 3.7, the *b*-values at the AE source position were set at 0.055, 0.081, and 0.062 for the 150, 250, and 500 kHz frequencies, respectively.

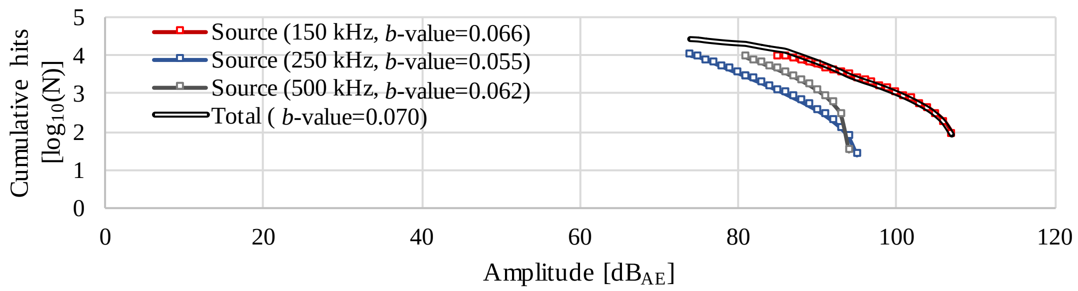

Figure 3.7 Assumed cumulative numbers of hits for 150, 250, and 500 kHz signals from an acoustic emission source

Figure 3.8 shows the simulation results for single and multiple AE frequencies at propagation distances of 30, 100, 300, and 500 mm. The multiple frequencies represent the sum of all single AE frequencies. The *b*-value was calculated for each distance using the linear portion of the data and applying the least-squares method. As shown in Figure 3.8, the shapes of the distributions of single-frequency AEs did not change, but only moved parallel to the horizontal axis, indicating that the *b*-value of a single-frequency source does not change when the propagation length changes. In contrast, the shapes of the distributions for multiple frequencies did change with propagation distance: the *b*-value decreased from 0.072 to 0.026 as the propagation length increased from 30 to 500 mm.

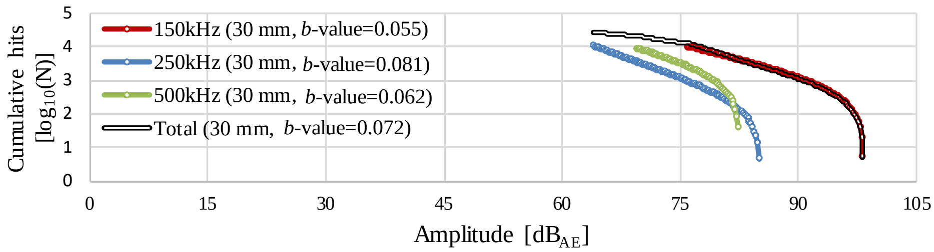

(a)

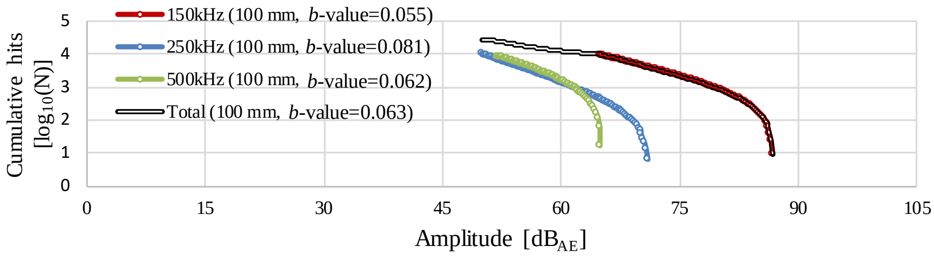

(b)

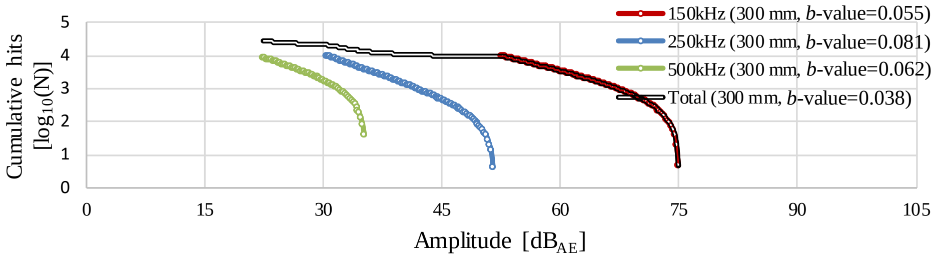

(c)

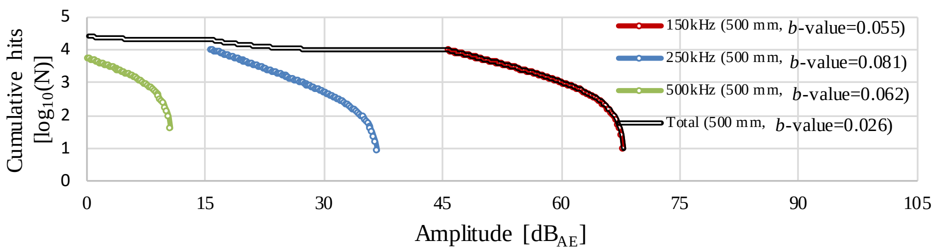

(d)

Figure 3.8 Cumulative acoustic emission hits with single and multiple frequencies as a function of amplitude at propagation distances from the source of (a) 30 mm, (b) 100 mm, (c) 300 mm, and (d) 500 mm Figure 3.9 Cumulative acoustic emission hits of single and multiple frequencies at 500 mm from the source, superimposed with the number of acoustic emission signals at the source

3.4 Change in *b*-values of woven glass-fiber-reinforced plastic specimens

AE detected during tensile tests of woven GFRP specimens were also analyzed in detail. The specimen, experimental setup, and tensile testing method were explained in Chapter 2.

Detected AE signals were divided pointwise into series of 1000 units and the time series of the *b*-value was calculated. The results for the three sensors are shown in Figure 3.10, as well as the applied stress. It is evident that the *b*-values differed for different propagation distances from the AE source. The *b*-values fluctuated during the test, but fell rapidly just before catastrophic failure occurred.

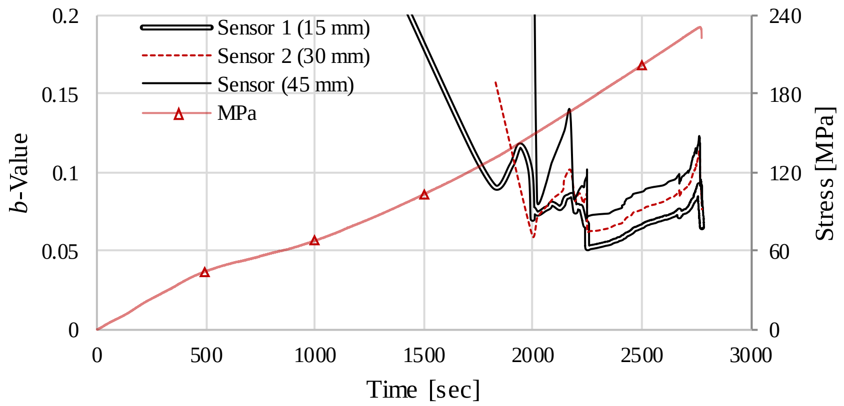

Figure 3.10 Time dependence of the *b*-value for various propagation lengths with variation in tensile stress

Figure 3.11 shows the distributions of the centroid frequency for different propagation lengths. The centroid frequency was calculated using *Visual AE-Suite* software (Vallen Systeme, Germany), which employs the fast Fourier transform method. The centroid frequency is an important parameter for characterizing the frequency dependence of the attenuation. The AE frequency ranges detected by Sensors 1 (15 mm), 2 (30 mm), and 3 (45 mm) were 75–525 kHz, 90–490 kHz, and 90–480 kHz, respectively. The frequency range of detected AE signals widened as the testing time increased and a wide range of

AE frequencies were detected before final failure. This result showed that the number of fracture modes that occurred in the specimen increased with test time.

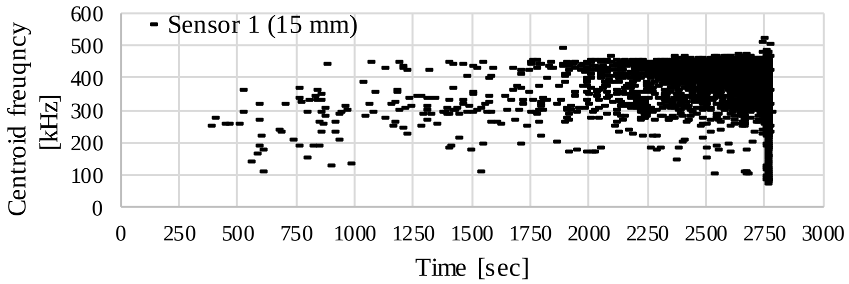

(a)

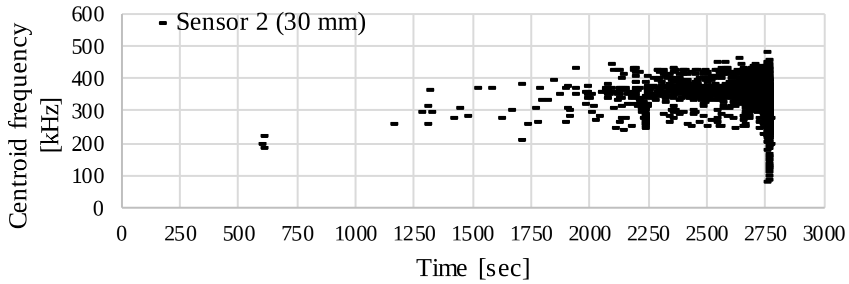

(b)

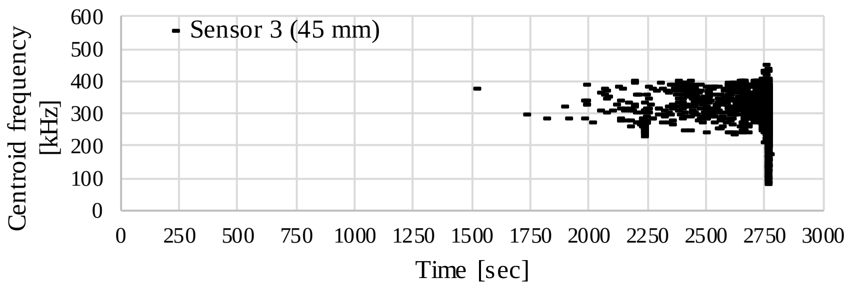

(c)

Figure 3.11 Distribution of centroid frequency with test time at propagation lengths of (a) 15 mm (Sensor 1), (b) 30 mm (Sensor 2), and (c) 45 mm (Sensor 3) from the source for glass-fiber-reinforced plastic specimen

Figure 3.12 shows the distribution of number of AE signals by centroid frequency for the three sensors placed at different propagation distances *d* from the source. The center frequencies were 440 kHz for *d* = 15 mm (Sensor 1), 380 kHz for *d* = 30 mm (Sensor 2), and 320 kHz and 390 kHz for *d* = 45 mm (Sensor 3). As shown in Figure 3.12, the peaks of the distributions shifted with propagation length, which may be caused by the frequency dependence of attenuation.

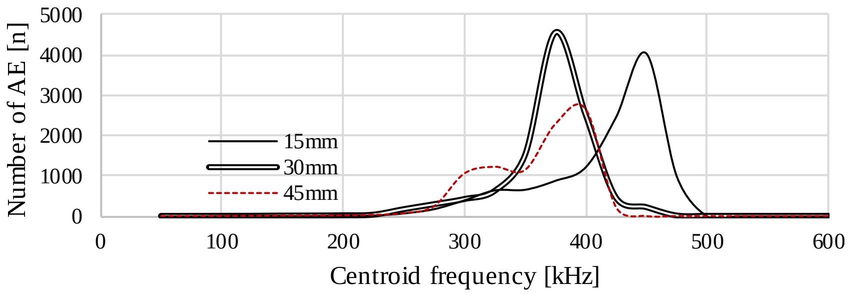

Figure 3.12 Frequency distributions of Sensors 1, 2, and 3 at final fracture (sum of frequencies emitted from all acoustic sources)

To investigate these changes in the *b*-value for AE in GFRP, a parametric study was then performed. Figure 3.13(a) presents an enlarged view of the blue line of Figure 3.10, showing the calculated *b*-values from experimental data as recorded by Sensor 3 (d = 45 mm). These signals were used as the AE source in the parametric study. The total number of source emissions was 8558. These exhibited various amplitudes (40–100 dB_{AE}), centroid frequencies, and times of occurrence. The number of AE signals at the source, presented by centroid frequency, is shown in Fig. 3.13(b), which is same as Sensor 3 data of Figure 3.12. In the simulation, the source AEs were divided into three groups as shown: Sources A, B, and C were AE signals in the frequency ranges of 50–320 kHz, 320–380 kHz, and 380–480 kHz, respectively, and with average frequencies of 185 kHz, 350 kHz, and 430 kHz, and numbers of source emissions of 2651, 3041, and 2866, respectively.

To estimate the AE attenuation factor, all signals of 70 dB_{AE} (3500 μV) and above were extracted from the 8558 data points. From the remaining data, AE signals with 237 kHz, 309 kHz, 349 kHz, and 402 kHz centroid frequencies at Sensor 1 (d = 15 mm) were extracted as representative data. Changes in amplitude of these representative AE signals with propagation distance are shown in Figure 3.14: the amplitudes of all signals decreased with increasing propagation distance; moreover, higher-frequency AE signals incurred higher attenuation than those of lower frequency. From these data and using Equation (3-1), the attenuation factors α were determined as 0.005, 0.009, 0.012, 0.018, and 0.030 Np/mm for centroid frequencies of 237, 309, 348, 402 and 469 kHz, respectively. The results are plotted in Figure 3.15(a), where the vertical axis represents the attenuation factor α. α increased with increasing centroid frequency. An empirical formula to estimate the attenuation factor from centroid frequency was determined from these data, as shown in Figure 3.14.

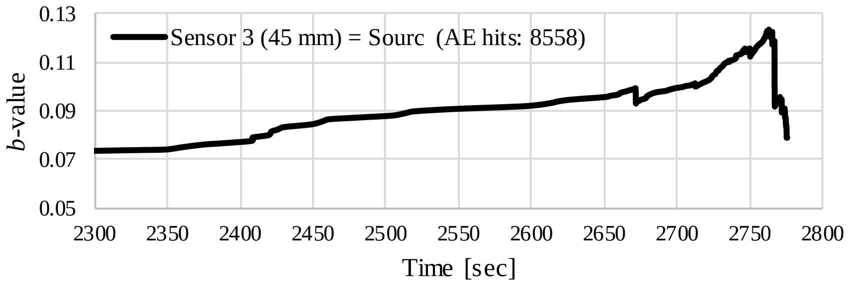

(a)

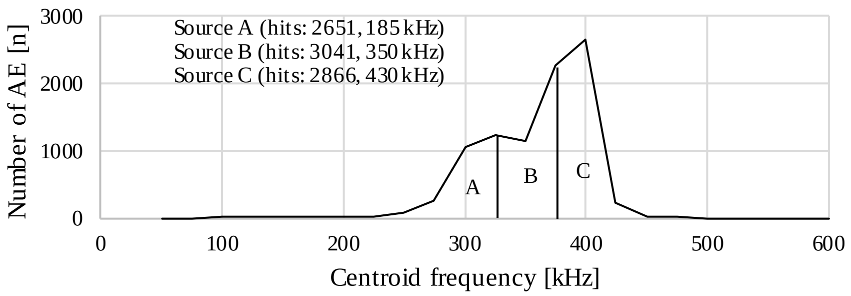

(b)

Figure 3.13 Acoustic emission source used for parametric study of glass-fiber-reinforced plastic specimen. (a) *b*-Values of acoustic emission detected by Sensor 3 and (b) number of acoustic emissions presented by centroid frequency and definition of sources

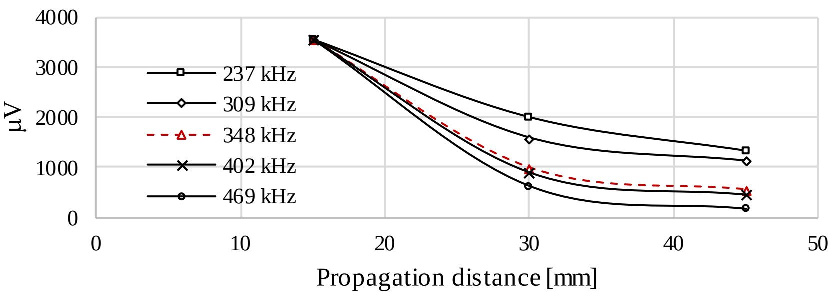

Figure 3.14 Dependence of acoustic emission amplitude on sensor location for centroid frequencies between 237 and 469 kHz

Figure 3.15(b) shows an example of results from the calculation of AE amplitude. AE signals with 185, 350, 430, and 322 kHz centroid frequencies and a minimum amplitude of 100 dB_{AE} were assumed, based on the data of Figure 3.13. The frequency of 322 kHz is the average of the first three of these frequency values. By using the empirical equation presented in Figure 3.15(a), the change in AE amplitude with propagation distance could be calculated for any AE with arbitrary amplitude and centroid frequency at the source.

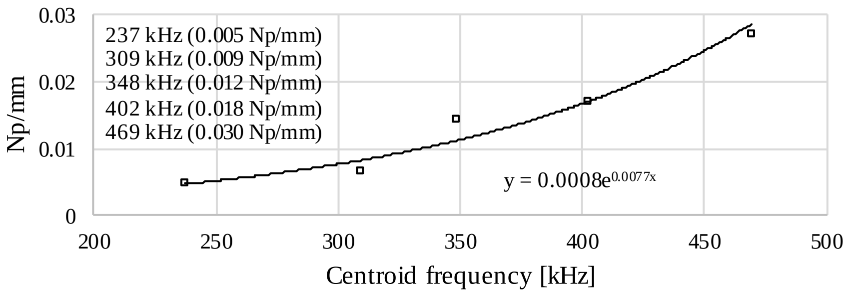

(a)

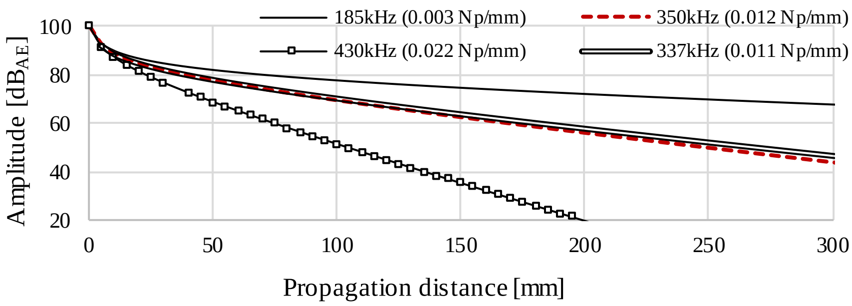

(b)

Figure 3.15 (a) Frequency dependence of attenuation and (b) cumulative acoustic emission amplitudes as a function of propagation length for multiple-frequency source

Using the empirical equation shown in Figure 3.15(a) and assuming the AE source shown in Figure 3.13, a parametric study for *b*-value was conducted. In the simulation, the threshold value to detect AEs was set as 30 dB_{AE}. The *b*-value was first simulated under the condition that the centroid frequency of all AE was constant (i.e., a single-frequency source) with a value of 322 kHz. The *b*-value was then calculated using the real AE data shown in Figure 3.13 as an AE source. As explained above, the total number of AE sources was 8558, which exhibited various amplitudes (40–100 dB_{AE}), centroid frequencies, and occurrence times (i.e., multiple frequencies).

Figure 3.16 shows the cumulative number of AE hits from 0 to 2760 s by amplitude for the single- and multiple-frequency sources. A parametric study was conducted using these data for propagation distances of 85 and 125 mm. The numbers of hits detected at these locations are shown. All AE signals (2110 events) were detected at both locations for the single-frequency source, but fewer signals were detected for the multiple-frequency source. The *b*-values were determined for each simulation condition by linearly fitting the simulated data: the values obtained showed that the *b*-value was unchanged for the single-frequency simulation, but did change for the multiple-frequency simulation.

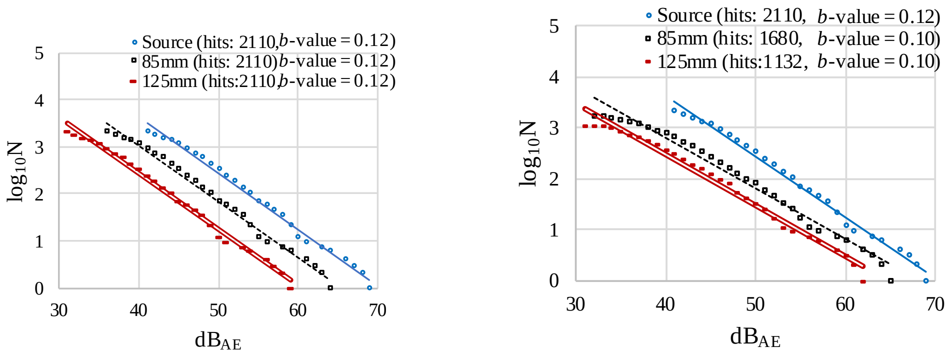

(a) (b)

Figure 3.16 Amplitude frequency distributions of acoustic emission signals emitted up to 2760 s of testing time with (a) single and (b) multiple frequencies. The distributions at the sources were also delayed at propagation lengths of 85 mm and 125 mm

Figure 3.17 shows the final simulation results for single and multiple frequencies for the different propagation lengths. The total numbers of detected AE signals at each position are shown. The *b*-value was calculated for each point (2300–2780 s/1000 points) using the least-squares method. As shown, the *b*-value of the single-frequency source did not change with propagation length; in contrast, a change occurred for the multiple-frequency source. The *b*-values for both propagation conditions fluctuated over some range during testing, although the average *b*-value for the specimen with a propagation length of 125 mm was lower than that of the source. From these results, it was evident that a change in *b*-value may be caused by a change in the frequency dependence of the attenuation after propagation and a change in the total number of signals used for the *b*-value calculation.

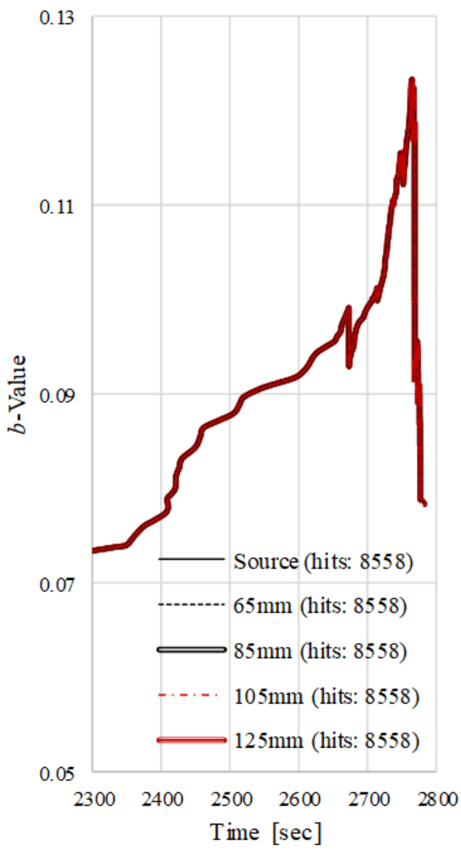

(a)

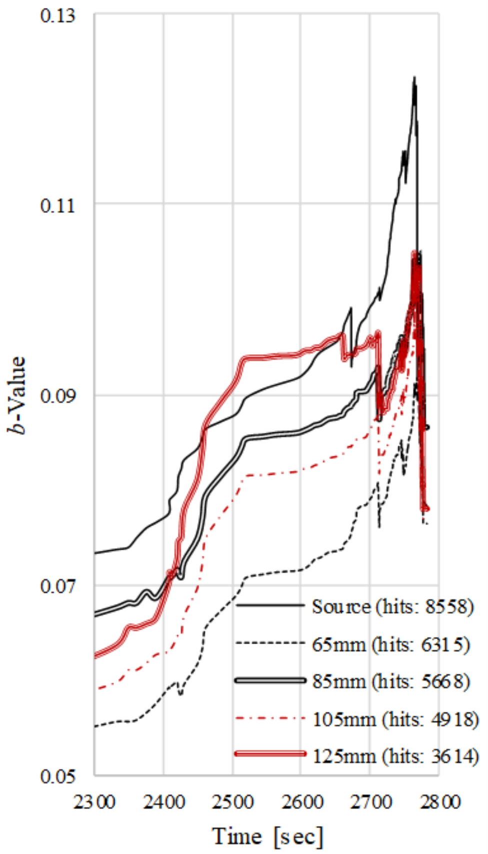

(b)

Figure 3.17 Simulated *b*-values for (a) single- and (b) multiple-frequency acoustic emission sources for different propagation distances

3.5 Conclusion

This chapter investigated the cause of changes in *b*-value with propagation distance. The *b*-value was analyzed for signals detected at different propagation distances from the AE source. The following points summarize the findings of this chapter.

1. AE signals detected for #1$[90]_{16}$, #2$[80]_{16}$, #3$[0]_{8}$, and cross-ply #4$[0/90]_{8}$ CFRP tensile specimens were analyzed. The dominant fracture modes (matrix cracking, fiber pull-out, and fiber breakage) changed with CFRP stacking sequence and the AE centroid frequency changed with fracture mode. The AE signals attributed to each fracture mode were separated using frequency filters of 100–250 kHz (matrix cracking), 450–550 kHz (fiber pull-out), and 550–650 kHz (fiber reakage). The *b*-values were calculated for the extracted AE signals with these single-frequency modes (AE within a limited frequency band) and determined to be almost constant with propagation distance; in contrast, when the AE source contained several fracture modes, the *b*-value changed with propagation distance.

2. To investigate the cause of this change in *b*-value, a parametric study was conducted. AE signals with several centroid frequencies and attenuation factors were assumed. When the AE source contained a single frequency, the distribution of AE number by amplitude simply moved parallel to the horizontal axis with propagation distance: in this case, the *b*-value did not change with propagation distance. The shape of the distribution for multiple AE signals (the sum of emissions with a single frequency) did, however, change. This was caused by a change in the proportion of each frequency component after propagation due to the frequency dependence of attenuation. For this reason, the *b*-value changed with propagation distance when the detected AE signals contained a wide band of centroid frequencies.

3. To more accurately conduct the parametric study, AE signals detected in a GFRP specimen were used as the AE source for the simulation. The attenuation factor was determined from experimental data and the threshold amplitude at which AE was

detected was also taken into account. Simulation results showed that changes in the *b*-value may be caused by changes in the contribution of each frequency component as a function of propagation distance.

3.6 References

[3-1] de Groot, P.J., Wijnen, P.A.M., Janssen, R.B.F.: Real-time frequency determination of acoustic emission for different fracture mechanisms in carbon/epoxy composites. Compos. Sci. Technol. 55, 405–412 (1995). doi:10.1016/0266-3538(95)00121-2

[3-2] Ramirez-Jimenez, C.R., Papadakis, N., Reynolds, N., Gan, T.H., Purnell, P., Pharaoh, M.: I dentification of failure modes in glass/polypropylene composites by means of the primary f requency content of the acoustic emission event. Compos. Sci. Technol. 64, 1819–1827 (2004).

[3-3] Gutkin, R., Green, C.J., Vangrattanachai, S., Pinho, S.T., Robinson, P., Curtis, P.T.: On acoustic emission for failure investigation in CFRP: Pattern recognition and peak frequency analyses. Mech. Syst. Signal Process. 25, 1393–1407 (2011).

[3-4] Colombo, I. S., Main, I. G., & Forde, M. C. (2003). Assessing damage of reinforced concrete beam using “b-value” analysis of acoustic emission signals. Journal of materials in civil engineering, 15(3), 280-286.

[3-5] Shiotani, T., Fujii, K., Aoki, T., & Amou, K. (1994). Evaluation of progressive failure using AE sources and improved b-value on slope model tests. Progress in acoustic emission, 7(7), 529-534.

[3-6] Shiotani, T., Yuyuma, S., Li, Z. and Ohtsu, M. (2001). Application of AE improved b-value to quantitative evaluation of fracture process in concrete materials. Journal of Acoustic Emission, 18, 118-133 .

[3-7] Shiotani, T., Luo, X., Haya, H., & Ohtsu, M. (2007, July). DAMAGE QUANTIFICATION FOR CONCRETE STRUCTURES BY IMPROVED b-VALUE ANALYSIS OFAE. In Earthquakes and Acoustic Emission: Selected Papers from the 11th International Conference on Fracture, Turin, Italy, March 20-25, 2005 (p. 181). CRC Press.

[3-8] Sagar, R. Vidya, BK Raghu Prasad, and S. Shantha Kumar. "An experimental study on cracking evolution in concrete and cement mortar by the b-value analysis of acoustic emission technique." Cement and Concrete Research 42.8 (2012): 1094-1104.

[3-9] Sagar, R. V., Prasad, B. R., & Kumar, S. S. (2012). An experimental study on cracking evolution In concrete and cement mortar by the b-value analysis of acoustic emission technique. Cement and Concrete Research, 42(8), 1094-1104.

[3-10] Schumacher, T., Higgins, C. C., & Lovejoy, S. C. (2011). Estimating operating load conditions on reinforced concrete highway bridges with b-value analysis from acoustic emission monitoring. Structural Health Monitoring, 10(1), 17-32.

Chapter 4 Effect of ultraviolet irradiation induced degradation of fiber reinforced plastics on *b*-value

4.1 Degradation of fiber-reinforced plastics

Chapter 3 discussed the cause of a changing *b*-value with propagation distance from an acoustic emission (AE) source over a wide frequency range of emissions. The change in *b*-value was mainly attributed to the frequency dependence of AE attenuation.

AE testing is used for condition monitoring of machines, structures, and vessels that are sometimes installed in the open, without the protection of a building. In such cases, AE monitoring continues over a long period and the tested materials become degraded. One of the major causes of degradation of fiber-reinforced plastic (FRP) is ultraviolet (UV) radiation, also known as photodegradation [4-1], [4-2]. Photodegradation mainly changes physical, mechanical, and chemical properties of FRPs. This chapter discusses AE signals that are generated by damage in degraded FRP and the resulting effect on the *b*-value.

4.2 Effect of ultraviolet radiation

Tensile tests of glass-reinforced-fiber plastic (GFRP) plate specimens (22 mm × 200 mm × 2 mm) with a center hole (2 mm in diameter) were conducted. GFRP tabs, 2 mm in thickness, were attached to the specimens at both ends to avoid causing any damage by the test jig. Three AE sensors (Physical Acoustics, Type: PICO) were mounted on the specimen at different distances from the hole (identified as Sensors 1, 2, and 3 in Figure 4.1). The cross-head speed of the tensile tester was controlled at 0.1 mm/min. Owing to this concentration of stress, the specimens broke near the center hole. The testing conditions for AE monitoring are shown in Table 4.1. AE signals greater than 35 dB_{AE} were detected. The front and back surfaces of the specimens used for the tensile test were irradiated by UV light for 0 to 300 h in a chamber from which all outside light was excluded. The UV strength was 1820 μW/cm^2 and the maximum spectrum output was 365 nm.

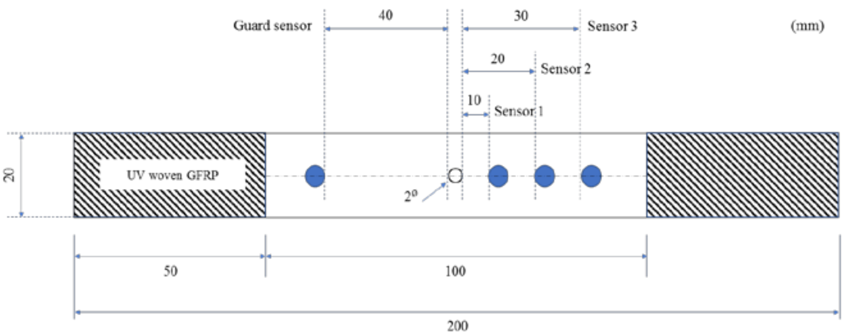

Figure 4.1 Schematic illustration of fiber-reinforced plastic specimen with a center hole and showing location of sensors

Table 4.1 Acoustic emission testing conditions

Threshold		Amplifier	Analog filter		Sampling conditions		
Type	dB_{AE}	dB_{AE}	Lower	Upper	Sampling rate	Pre-trigger	Length
Fixed	35	40	1 kHz	1 MHz	10 MHz	50 □ sec	1 k

Following a tensile test, the AE signals measured by each sensor were clustered for each event: signals detected within 100 μs from the first-measured signals were considered to originate from the same cluster.

Table 4.2 shows optical images of UV-aged specimens after exposure of 0, 100, 200, and 300 h to UV radiation. Yellowing of the specimen was clearly seen after 200 h and increased with increasing UV radiation time.

Table 4.2 Optical images of woven glass-fiber-reinforced specimens with center hole after different durations of ultraviolet radiation

UV radiation time	0 h	100 h	200 h	300 h
Woven GFRP	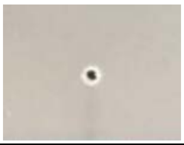			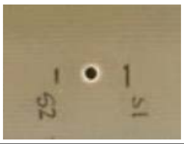

Table 4.3 compares the mechanical properties of virgin (UV irradiation: 0 h) and UV-degraded specimens. Fracture stress significantly changed after irradiation for 100 h; fracture strain gradually changed with increasing irradiation time. Table 4.4 summarizes the AE test results for each specimen. The maximum AE amplitude was 99 dB_{AE} and the total number of AE hits was almost the same.

Table 4.3 Effect of mechanical properties on exposure to ultraviolet radiation

	Irradiation time	Fracture stress	Fracture stress
	[Hour]	[MPa]	[%]
#6-0UV	0	279	2
#6-100UV	100	211	2.1
#6-200UV	200	182	2.3
#6-300UV	300	174	2.4

Table 4.4 Summary of acoustic emission test results

	Total test time	1st AE hit	Total AE hits	Max. Amp
	[sec.]	[sec.]		dB_{AE}
#6-0UV	1751	166	13158	99
#6-100UV	1779	145	13158	99
#6-200UV	1301	74	13263	99
#6-300UV	1410	111	13375	99

Figure 4.2 shows photographs of fractured specimens irradiated for 0 h and 300 h. Matrix cracking was dominant fracture mode for the specimen without irradiation (0 h); both matrix cracking (indicated by the circle) and pull-out (square) were observed in the specimen irradiated for 300 h.

(a)


(b)


(c)
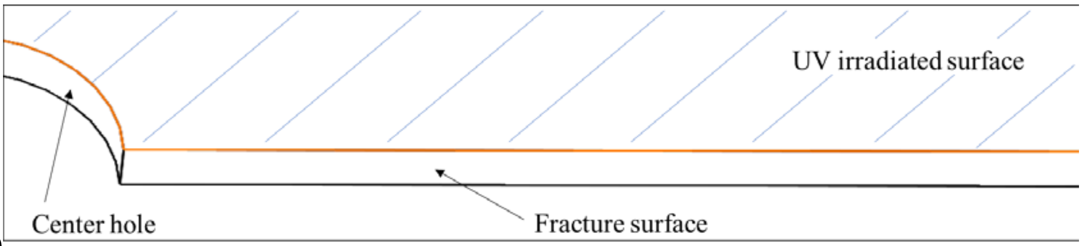

Figure 4.2 Photographs of fractured specimens subjected to ultraviolet radiation for (a) 0 h and (b) 300 h. Image (c) presents a description of the photograph locations

Figure 4.3 shows the AE signals detected during tensile testing of the #6-0UV, #6-100UV, #6-200UV, and #6-300UV specimens, where the horizontal axes are the specimen life time, defined as 100% at the time of final failure; the vertical axes show the AE amplitude (maximum value of an AE waveform with a single emission, measured in dB_{AE}, and marked by *). The corresponding changes in stress are shown by the black lines. It is evident that the amplitude distributions prior to 25% of the total life time were significantly changed by irradiation time.

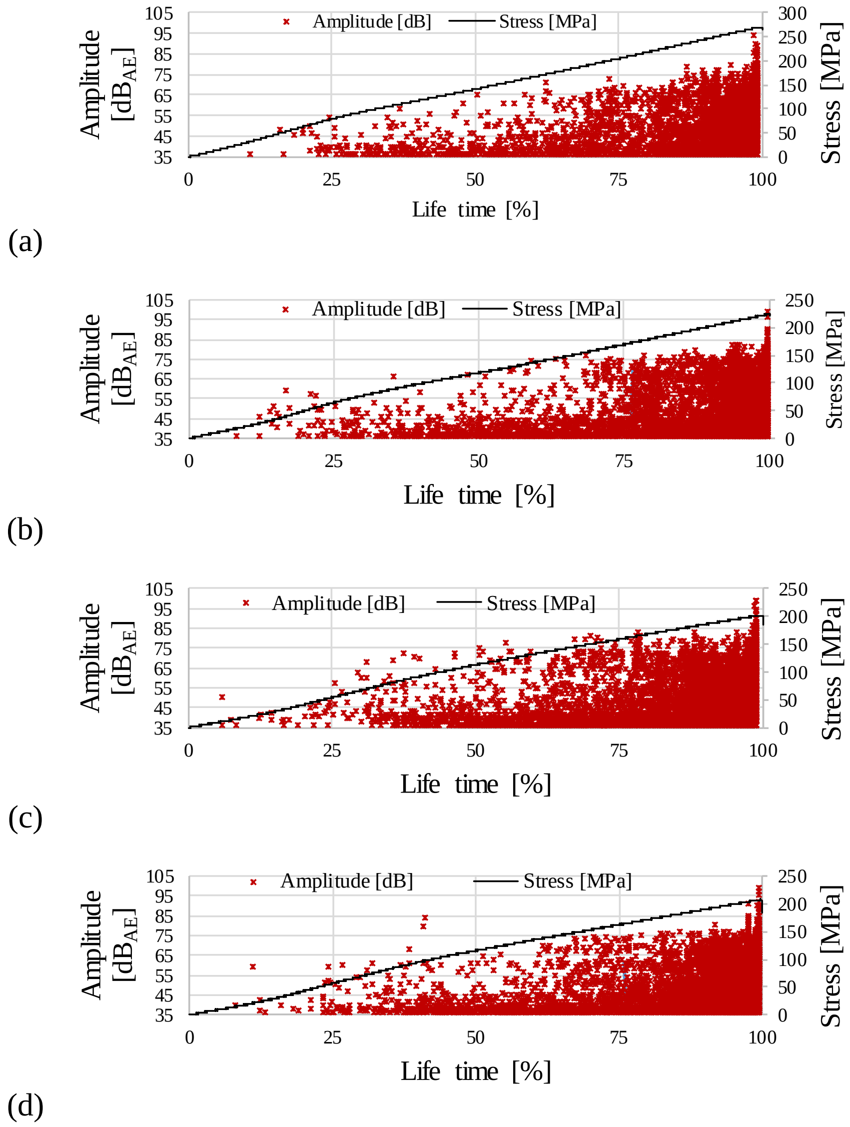

Figure 4.3 Effect on change of amplitude with life time of specimens irradiated with ultraviolet light for (a) 0 h, (b) 100 h, (c) 200 h, and (d) 300 h. Stress history is shown by the black line

Figure 4.4 shows the *b*-values calculated using AE signals detected by Sensor 1 for these specimens. The *b*-value of the virgin specimen at 75–90% life time is clearly distinguished from those of the degraded specimens. A decrease in *b*-value means an increase in macro-crack occurrence. In this period of the life time, numerous macro-cracks occurred in the degraded specimens compared with the virgin specimen.

In this thesis, the effect of degradation of the materials on changes in the *b*-value (i.e., changes in characteristics of AE propagation induced by degradation) is the target of discussion. The *b*-values in Figure 4.4 were affected by both the changing failure mechanism itself and changing characteristics of AE propagation: these two effects are separated for the purposes of discussion.

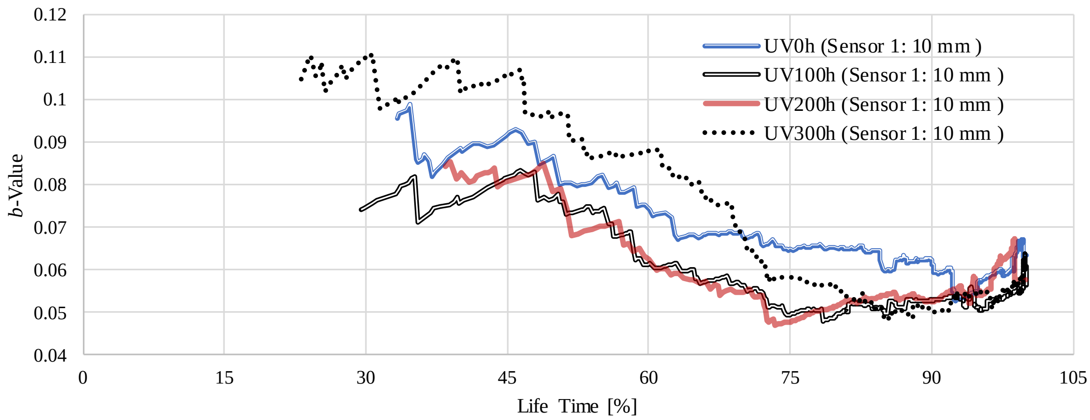

Figure 4.4 Logarithm of cumulative amplitude distributions corresponding to increasing ultraviolet irradiation time, as measured by sensors located at different propagation distances from the source

Figure 4.5 shows the centroid frequency distributions for specimens #6-0UV to #6-300UV detected by Sensors 1 (*d*: 10 mm) and 2 (*d*: 20 mm), where the horizontal axes show the frequency centroid in kHz and the vertical axes show the number of hits at each frequency. The black and red lines indicated the number of AE hits detected by Sensors 1 and 2, respectively. The distributions of centroid frequency change with propagation distance due to the frequency dependence of AE attenuation. The AE signal at the source contained a wide range of frequency components [Figure 4.6(a)], but the higher-frequency components decreased readily with propagation distance [Figure 4.6(b)]; therefore, signals in the higher-frequency region decreased more rapidly than those in lower-frequency regions. As a result, the centroid frequency changed with propagation distance [Figure 4.6(c)]. Figure 4.5(d) shows the distribution of centroid frequencies for the specimen irradiated for the longest time (300 h): the number of AE signals with a centroid frequency of 150–200 kHz was larger than that of the other specimens.

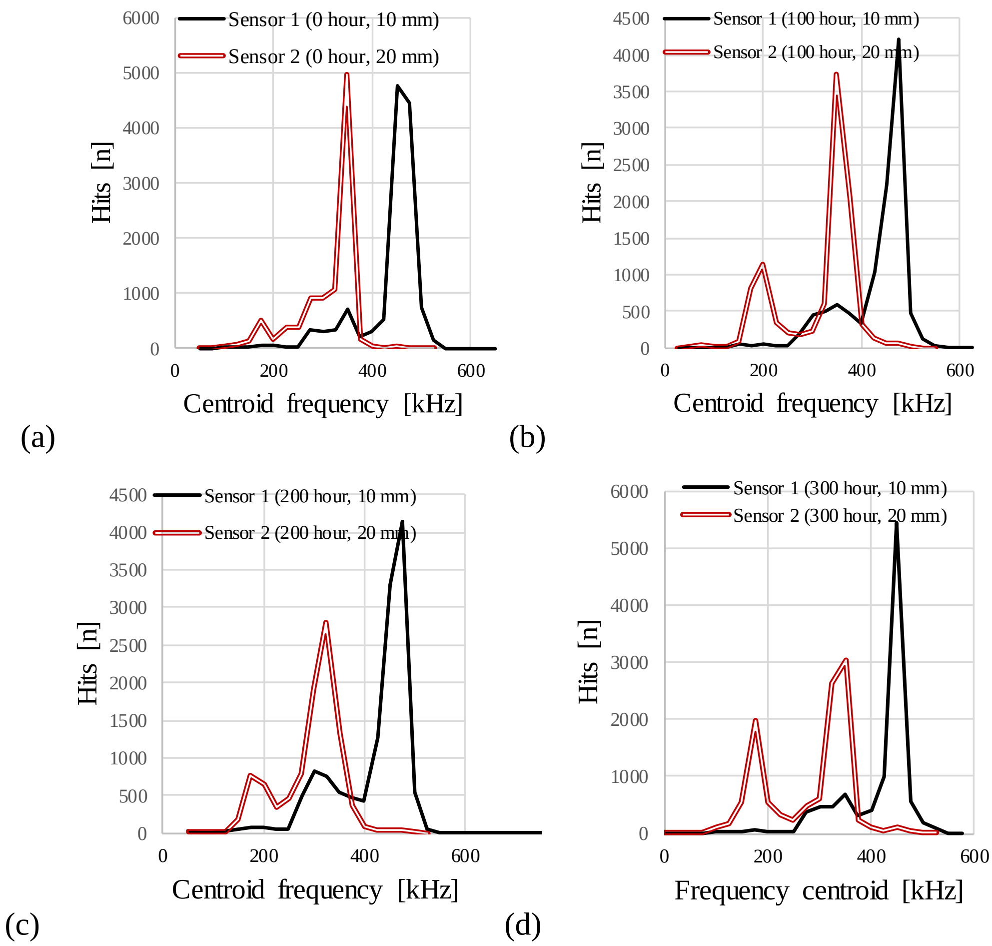

Figure 4.5 Frequency centroid distributions as a function of the number of acoustic emission hits recorded by Sensors 1 and 2 (propagation distances of 10 mm and 20 mm, respectively) during tensile testing of specimens (a) #6-UV 0, (b) #6-UV 100, (c) #6-UV 200, and (d) #6-UV300

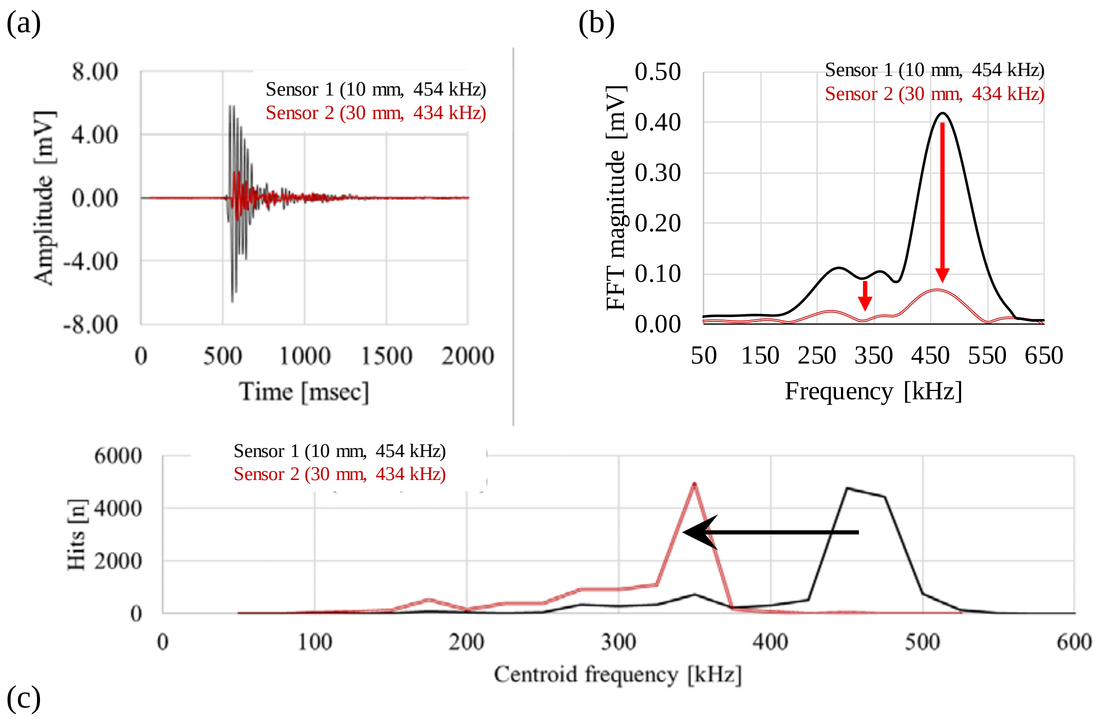

Figure 4.6 (a) Acoustic emission signals, (b) their frequency components, and (c) centroid frequency distributions at propagation distances of 10 mm and 30 mm for 0 h ultraviolet irradiation time

Figure 4.7 shows the *b*-values measured for tensile tests in which the sensor locations were 10 mm to 30 mm from the center hole (AE source positions). The *b*-values increased with increasing propagation distance, with the exception of the data shown in Figure 4.7(d) at 20–50% life time. The extent of differences between the three curves in each figure changed with irradiation time, showing that degradation of materials by UV irradiation causes as change in wave-propagation characteristics, which may affect the *b*-value.

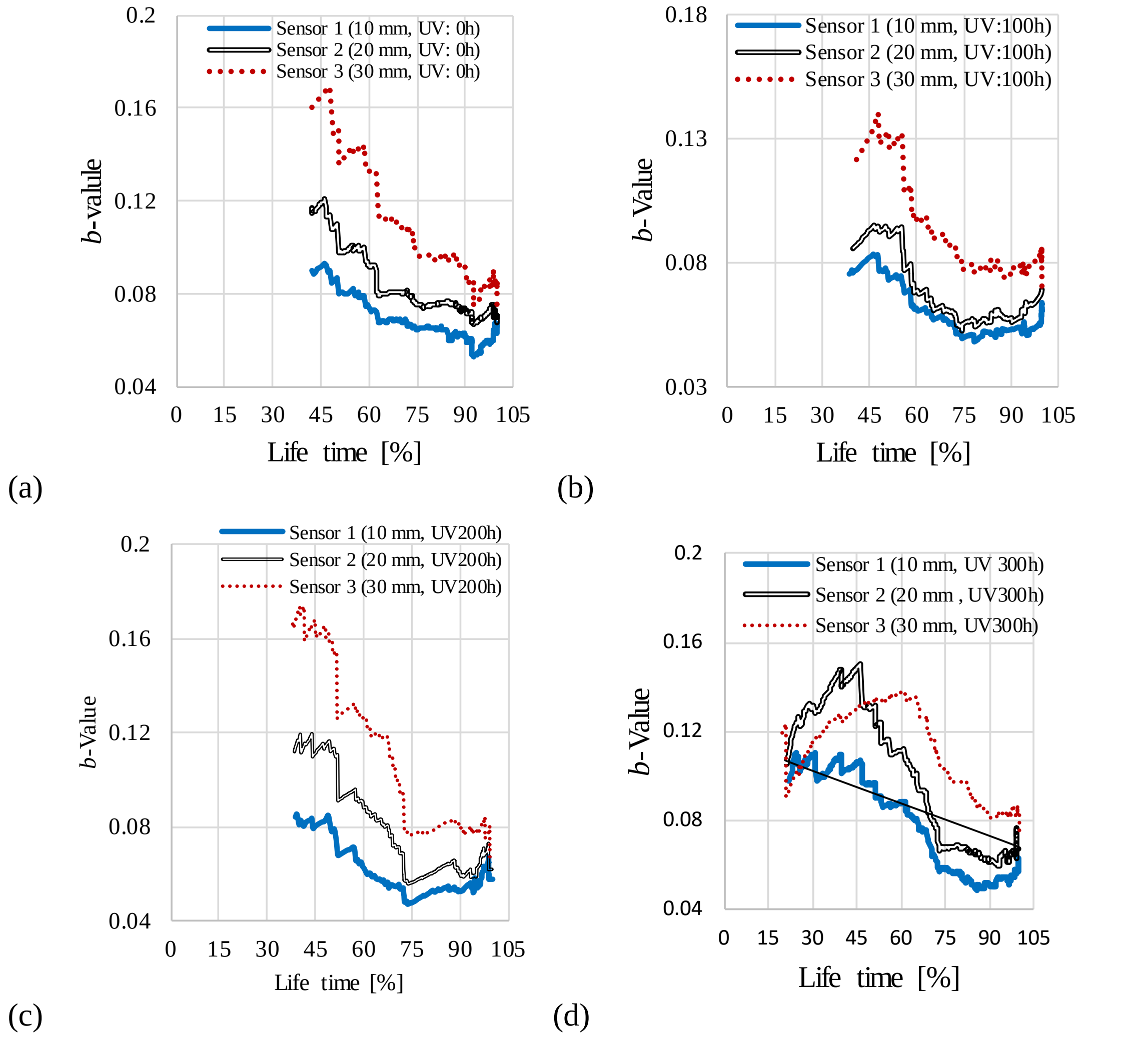

Figure 4.7 *b*-Value distributions of specimens subjected to ultraviolet radiation for (a) 0 h, (b) 100 h, (c) 200 h, and (d) 300 h at propagation distances of 10, 20, and 30 mm

Considering that the attenuation factor of woven GFRP was changed by UV irradiation, the sensors received more attenuated AE from the UV-irradiated specimens: a small number of AE signals was received by Sensor 3 for the 300 h irradiated specimen; as a result, *b*-values for Sensor 3 at 20–50% life time were low [Figure 4.7(d)].

Figure 4.8 shows the results of an investigation of the reason for changes in the AE attenuation distribution with different UV irradiation times, i.e., the attenuation factor was estimated using Equation (3-1). These results showed that the attenuation of specimens irradiated for less than 200 h decreased compared with that of virgin specimens, but increased in the specimens irradiated for 300 h. Generally, the initial effect of UV irradiation effect is to decrease attenuation because of UV surface hardening: as UV irradiation time increases, various defects occur on the surface and the attenuation increases [4-3]. The change in the frequency dependence of the attenuation is discussed in Chapter 5.

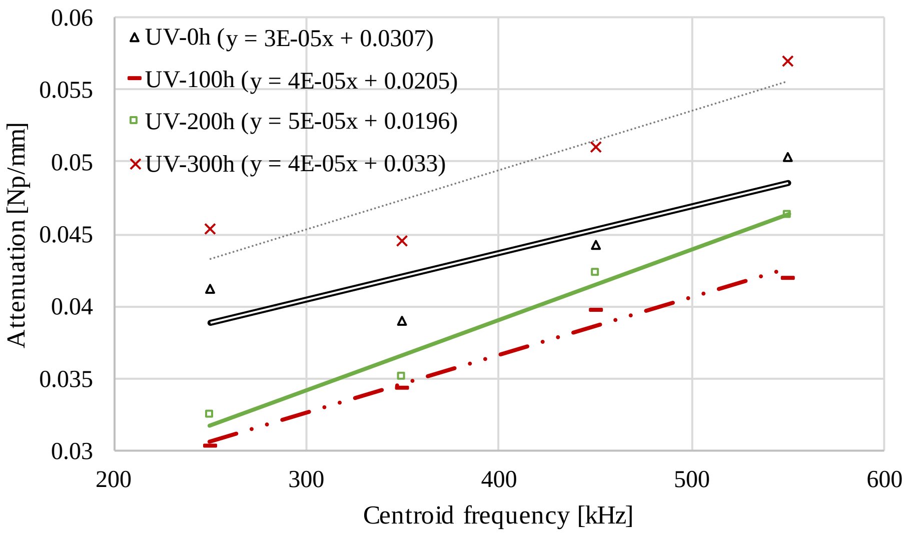

Figure 4.8 Frequency dependence of attenuation with increasing duration of ultraviolet irradiation

Figure 4.9 shows the relationship between phase velocity and frequency of AE when assuming velocities of the longitudinal and shear waves of 3150 and 1727 m/s, respectively[4-4]. The velocities of most AE signals detected in this study were less than 2000 m/s, indicating that most detected AE seemed propagate in A_0 mode. When AE propagates in A_0 mode, the phase velocity is almost constant in the main frequency band detected (100–600 kHz). As a result, the effect of the dispersion nature of Lamb waves on the modified *b*-value is low. In contrast, the wavelengths of detected AE in this study were larger than the specimen plate thickness, so AE signals propagated through the full thickness of the plate. AE propagation was therefore affected by both the UV degradation area near the specimen surface and by the undamaged area at the center of the specimen.

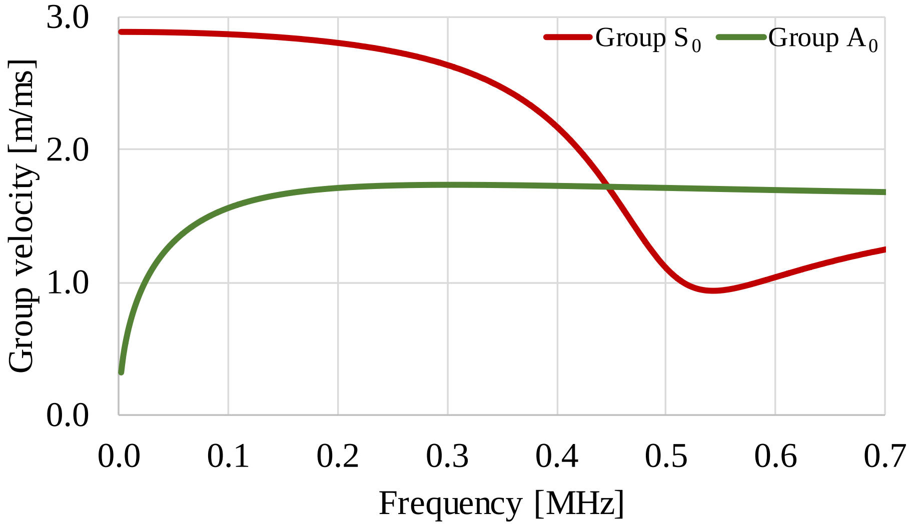

Figure 4.9 Relationship between phase velocity and frequency of acoustic emission (P-wave: 3.150 mm/μs; S-wave: 1.727 mm/μs: *t* = 2.5 mm [4-4])

4.3 Parametric study of *b*-value with degraded attenuation

To clarify the effects of UV irradiation without surface damage, a parametric study was conducted. AE detected during tensile testing of UV-degraded GFRP specimens were analyzed in detail. The woven GFRP AE source, simulation set-up, and tensile test method are explained in Chapter 3.

Table 4.5 shows an example of results of attenuation with different UV irradiation times, calculated using data from Figure 4.7. The time ranges used for the degraded AE signals were 1651–1751 s, 1679–1779 s, and 1109–1309 s for specimens irradiated for 0 h, 100 h, and 200 h, respectively. The attenuation of each AE signal was calculated using Equation (3-1). These data show that high UV irradiation times induced lower attenuation of AE signals because the UV-affected GFRP became brittle with surface cracks [4-1].

Table 4.5 Attenuation parameters

	UV irradiation time	Centroid frequency [kHz]		
		Source A (180)	Source B (350)	Source C (430)
	[Hour]	[Np/mm]	[Np/mm]	[Np/mm]
UV-0h	0	0.0397	0.0482	0.0532
UV-100h	100	0.0277	0.0205	0.0385
UV-200h	200	0.0286	0.0371	0.0421

Figure 4.10 shows the frequency dependency of the attenuation parameters used for additional simulations. The range for attenuation in the specimen in the absence of UV radiation (specimen labelled UV-0h) was considered to be valid within ±10% of the measured value. The slope of the frequency dependence of attenuation remained the same. Attenuation differences of ±10% changed the base of the 250 kHz UV-0h attenuation and were designed to compare the effects of attenuation distribution for the

same propagation distance. Table 4.6 summarizes the attenuation values used in the simulation.

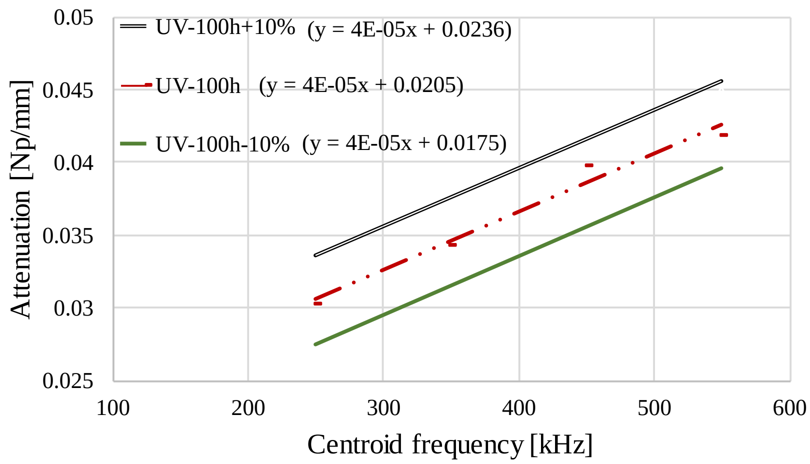

Figure 4.10 Valid range of attenuation of acoustic emission signals in the UV–0h specimen, showing a range of ±10% of the measured value, as used in simulations

Table 4.6 Attenuation parameters with ± 10% range

	Centroid frequency [kHz]		
	Source A (180)	Source B (350)	Source C (430)
UV-100h + 10%	0.0308	0.0376	0.0408
UV-100h	0.0277	0.0345	0.0377
UV-100h - 10%	0.0247	0.0315	0.0347

Figure 4.11 shows the simulated amplitude distributions using the #5 woven GFRP AE source at 45 mm propagation distance, where attenuation was limited to that caused by UV irradiation only. Only a single propagation distance was used (45 mm), so all AE sources were affected by only one attenuation parameter. The vertical axis shows the total AE at each amplitude; in Figure 4.10(a), the red, black, and blue lines represent the number of AE hits degraded by UV irradiation exposure for 0 h, 100 h, and 200 h, respectively. Figure 4.10(b) shows the analogous data with the ±10% attenuation range.

When the acoustic signal was propagated with different frequency-dependent attenuation ratios, the amplitude distribution changed at the same propagation distance; however, when the attenuation parameter increased without a change in the frequency-dependent attenuation ratio, the amplitude distribution was unchanged. The total number of AE hits also changed with change in the frequency-dependent attenuation ratio for a given propagation distance. This result is similar to that observed for the amplitude distributions of multiple frequencies with increasing propagation distance.

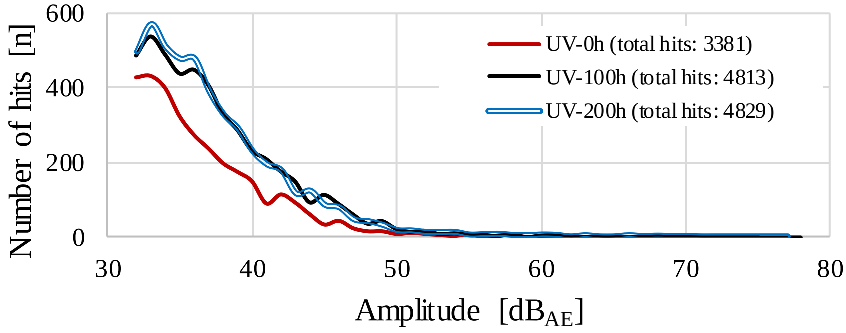

(a)

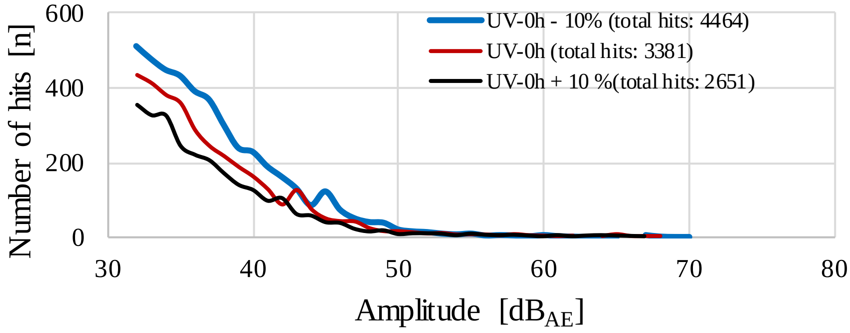

(b)

Figure 4.11 Distribution of acoustic emission hits attributed to (a) attenuation by ultraviolet radiation and (b) ±10% of the attention for the non-irradiated sample

Figure 4.12 shows the amplitude frequency distributions generated by the parametric study with the attenuation parameter and its ±10% values as a function of UV irradiation time at a propagation distance of 45 mm. Figure 4.10(a) shows that the *b*-value changed with the frequency dependence of the attenuation ratio at a given propagation distance, but did not change for same frequency dependence of attenuation ratio. This result resembles that of the AE testing of the carbon-fiber-reinforced (CFRP) specimens #2[80]$_{16}$ to #4[0/90]$_8$ and the #5 woven specimen, although the change was smaller; however, compared with the results for the #5 woven single-frequency experiment, which did not change with propagation distance, a clear change was found in the parametric study.

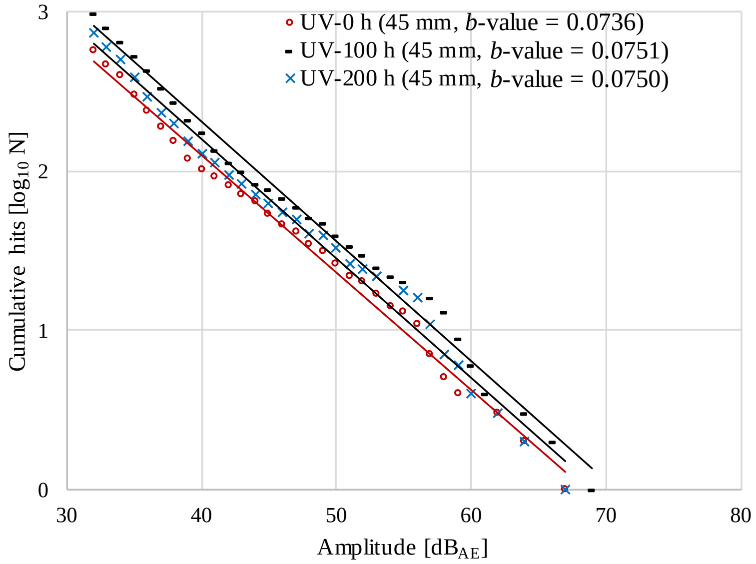

(a)

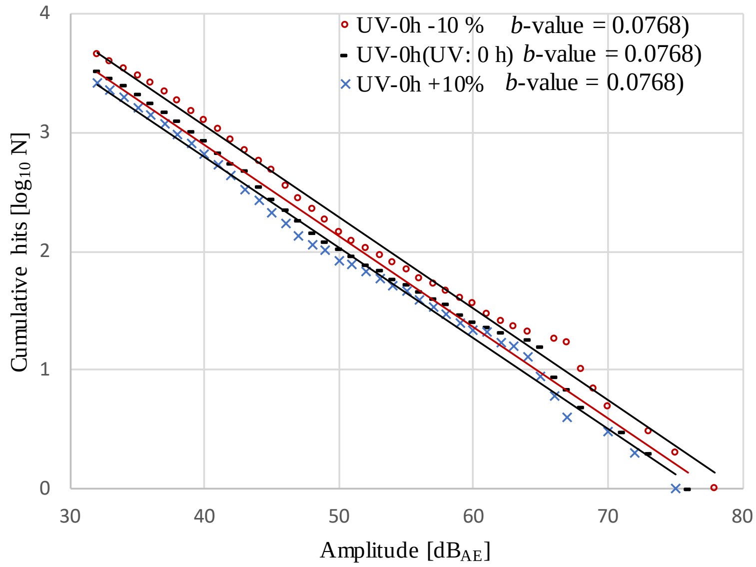

(b)

Figure 4.12 Plots of cumulative acoustic emission events as a function of amplitude and *b*-values for different attenuation factors using (a) multiple and (b) single slopes

4.4 Conclusions

This chapter investigated the cause of the *b*-value changing with increasing UV irradiation time. The *b*-value was analyzed for AE signals detected under conditions of different UV irradiation times from an AE source. The following summarize the conclusions of this chapter.

1. Tensile properties and AE parameters were analyzed using FRP specimens irradiated for 0, 100, 200, and 300 h with UV radiation. Yellowing occurred during the UV irradiation tests. Fracture stress and fracture strain decreased with increasing UV irradiation time. The amplitudes of the AE signals correspondingly changed, causing a change in the *b*-value.

2. To investigate the cause of the change in *b*-value with UV irradiation, the centroid frequency distribution of AE hits was calculated for increasing UV irradiation times. A single AE signal contains a wide band of frequencies, which varies with the frequency dependence of the attenuation: as a result, the centroid frequency changed with propagation distance of the AE signal from the source. When comparing the results for UV irradiation times of 100 h and 30 h, the centroid frequency changed with 10 mm propagation distance from Sensor 1 to Sensor 2. These results were clarified by analyzing the attenuation distribution using Equation (3-1). The frequency dependence of the attenuation distribution changed as the UV irradiation time increased.

3. A simulation was performed out to investigate the effect of change of frequency dependency of attenuation. AEs detected in a GFRP specimen were used as the AE source. Additional artificial attenuation was introduced based on the attenuation of a virgin specimen and the UV-induced attenuation factor was experimentally determined. This value was varied within ±10%. The *b*-value changed with the change in frequency dependence of attenuation for a given propagation distance, but did not change for the same frequency dependence of attenuation.

4.5 References

[4-1] Chin, J. W., Nguyen, T., & Aouadi, K. (1997). Effects of environmental exposure on fiber-reinforced plastic (FRP) materials used in construction. *Journal of Composites, Technology and Research*, *19*(4), 205-213.

[4-2] Kumar, B. G., Singh, R. P., & Nakamura, T. (2002). Degradation of carbon fiber-reinforced epoxy composites by ultraviolet radiation and condensation. *Journal of Composite materials*, *36*(24), 2713-2733.

[4-3] Bamford, C. H., Jenkins, A. D., & Johnston, R. (1957, February). Studies in Polymerization. XI. Reactions between Polymer Radicals and Ferric Chloride in Non-Aqueous Media. In Proceedings of the Royal Society of London A: Mathematical, Physical and Engineering Sciences (Vol. 239, No. 1217, pp. 214-229). The Royal Society.

[4-4] Advanced NDT LTD, "Ultrasonic velocity table", http://www.advanced-ndt.co.uk (2017.08.03)

Chapter 5 Use of a modified *b*-value for integrity evaluation of fiber-reinforced plastics

5.1 Introduction

The amplitude of an acoustic emission (AE) source is associated with the magnitude of fracture of its structure, so the *b*-value (defined as the slope of the amplitude frequency distribution) is known as an effective index related to the state of fracture [5-1]; however, this work has shown that the general *b*-value is not applicable to fiber-reinforced plastic (FRP) structures, for reasons explained in Chapters 3 and 4. AE signals from FRPs are generated by several fracture modes, including matrix cracking, fiber pull-out, and fiber breakage. Each fracture mode generates different and wide frequency bands. This behavior differs from that of concrete structures used in the field of civil engineering. When AE sources contain several fracture modes (different and wide frequency bands), the *b*-value changes with propagation distance. Furthermore, when FRPs are exposed to ultraviolet (UV) irradiation, the attenuation is also changed by UV degradation and the *b*-value is correspondingly affected. These problems can be described by Equation (3-1). Changing $\alpha(\omega)$ to $\alpha(\omega, t_{UV})$ in Equation (3-1) allows the derivation of Equation (5-1):

$$A(\omega, r) = A_0(\omega) \cdot \frac{1}{\sqrt{r}} \cdot \exp\{-\alpha(\omega, t_{UV}) \cdot r\}, \tag{5-1}$$

where $A(\omega, r)$ is the amplitude that propagates depending on the frequency and $\alpha(\omega, t_{UV})$ is the amplitude attenuation that depends on frequency and UV irradiation time. Here, $A(\omega, r)$ is the amplitude of an AE signal at a propagation distance r and frequency ω, A_0 is the amplitude at the source position, and α is the attenuation ratio, which depends on both the frequency ω and UV irradiation time, t_{UV}. When α is constant with ω and t_{UV}, the *b*-value does not change with propagation distance of the AE signal or UV irradiation time; however, the results from Chapters 3 and 4 show that α does change with both ω and t_{UV} for the materials considered, thereby affecting the *b*-value. In this chapter, the proposed use of a modified *b*-value that is not affected by changes in α is discussed.

5.2 Amplitude distribution at acoustic emission source

In general, decay of the amplitude of AE signals with propagation distance *r* can be expressed by Equation (5-2), based on Equation (5-1), when considering the relative sensitivity of each sensor $S_X(\omega)$ [X = A (Sensor 1); B (Sensor 2); C (Sensor 3)]:

$$A_{iX}\{\omega, t_{UV}, r_{iX}\} = S_X(\omega)\cdot A_{iO}(\omega)\cdot\frac{1}{\sqrt{r_{iX}}}\cdot\exp\{-\alpha_i[\omega, t_{UV}]\cdot r_{iX}\}, \qquad (5\text{-}2)$$

Known value: $A_{iX}(\omega, t_{UV}, r_{iX})$, r_{iX};

Unknown value: $A_{iO}(\omega)$, $\alpha(\omega, t_{UV})$, $S_X(\omega)$.

Here, A_{iX} is the amplitude of the AE signal from the i^{th} AE source at sensor X; A_{iO} is the amplitude of the AE signal at the source position that is excited at the i^{th} AE source; $\alpha(\omega, t_{UV})$ is the attenuation factor; r_{iX} is the propagation distance from the source to sensor X for i^{th} AE source. The value of r_{iX} can be accurately determined using the source location method (explained in Chapter 1). From Equation (5-2), it is evident that the amplitude of AE signals at the source position A_{iO} is not affected by $\alpha(\omega, t_{UV})$. A method of estimating A_{iO} from A_{iX} and r_{iX} is discussed, using the example of AE signals detected in the #5 woven glass-fiber-reinforced plastic (GFRP) specimen by Sensors 1 to 3.

When considering attenuation of an AE signal from a single AE source, the following equations can be derived from Equation (5-2):

$$e^{\alpha_i(\omega, t_{UV})\cdot r_{iX}} = S_X(\omega)\cdot A_{iO}(\omega)\cdot\frac{1}{A_{iX}(\omega, t_{UV}, r_{iX})}\cdot\frac{1}{\sqrt{r_{iX}}}; \qquad (5\text{-}3)$$

$$\alpha_i(\omega, t_{UV}) = \frac{1}{r_{iX}}\cdot\ln[S_X(\omega)] + \frac{1}{r_{iX}}\cdot\ln[A_{iO}(\omega)] - \frac{1}{r_{iX}}\cdot\ln[A_{iX}(\omega, t_{UV}, r_{iX})] - \frac{1}{r_{iX}}\cdot\ln[\sqrt{r_{iX}}]. \qquad (5\text{-}4)$$

Using amplitudes (A_{1A} and A_{1B}) and propagation distances (r_{1A} and r_{1B}) to Sensors 1 and 2 (*A* and *B* in the equations, respectively) for the first AE source:

$$\alpha_1(\omega, t_{UV}) = \frac{1}{r_{1A}}\cdot\ln[S_A(\omega)] + \frac{1}{r_{1A}}\cdot\ln[A_{1O}(\omega)] - \frac{1}{r_{1A}}\cdot\ln[A_{1A}(\omega, t_{UV}, r_{1A})] - \frac{1}{r_{1A}}\cdot\ln[\sqrt{r_{1A}}]; \qquad (5\text{-}5)$$

$$\alpha_1(\omega, t_{UV}) = \frac{1}{r_{1B}}\cdot\ln[S_B(\omega)] + \frac{1}{r_{1B}}\cdot\ln[A_{1O}(\omega)] - \frac{1}{r_{1B}}\cdot\ln[A_{1B}(\omega, t_{UV}, r_{1B})] - \frac{1}{r_{1B}}\cdot\ln[\sqrt{r_{1B}}]. \qquad (5\text{-}6)$$

Attenuation is the same in the same material [$\alpha_1(\omega,t_{UV})=\alpha_1(\omega,t_{UV})$], so the amplitude of the first AE source at source position A_{1O} can be calculated using the following procedure:

$$\frac{1}{r_{1A}}\cdot\ln[S_A(\omega)]+\frac{1}{r_{1A}}\cdot\ln[A_{1O}(\omega)]-\frac{1}{r_{1A}}\cdot\ln[A_{1A}(\omega,t_{UV},r_{1A})]-\frac{1}{r_{1A}}\cdot\ln[\sqrt{r_{1A}}]$$

$$=\frac{1}{r_{1B}}\cdot\ln[S_B(\omega)]+\frac{1}{r_{1B}}\cdot\ln[A_{1O}(\omega)]-\frac{1}{r_{1B}}\cdot\ln[A_{1B}(\omega,t_{UV},r_{1B})]-\frac{1}{r_{1B}}\cdot\ln[\sqrt{r_{1B}}];$$

(5-7)

$$\left(\frac{r_{1B}-r_{1A}}{r_{1B}\cdot r_{1A}}\right)\ln[A_{1O}(\omega)]=\frac{1}{r_{1B}}\cdot\left\{\ln\left[\frac{S_B(\omega)}{A_{1B}(\omega,t_{UV},r_{1B})\cdot\sqrt{r_{1B}}}\right]\right\}-\frac{1}{r_{1A}}\cdot\left\{\ln\left[\frac{S_A(\omega)}{A_{1A}(\omega,t_{UV},r_{1A})\cdot\sqrt{r_{1A}}}\right]\right\};$$

(5-8)

$$\ln[A_{1O}(\omega)]=\frac{r_{1A}}{r_{1B}-r_{1A}}\cdot\left\{\ln\left[\frac{S_B(\omega)}{A_{1B}(\omega,t_{UV},r_{1B})\cdot\sqrt{r_{1B}}}\right]\right\}-\frac{r_{1B}}{r_{1B}-r_{1A}}\cdot\left\{\ln\left[\frac{S_A(\omega)}{A_{1A}(\omega,t_{UV},r_{1A})\cdot\sqrt{r_{1A}}}\right]\right\};$$

(5-9)

$$A_{1O}(\omega)=e^{\left\langle\frac{r_{1A}}{r_{1B}-r_{1A}}\cdot\left\{\ln\left[\frac{S_B(\omega)}{A_{1B}(\omega,t_{UV},r_{1B})\cdot\sqrt{r_{1B}}}\right]\right\}-\frac{r_{1B}}{r_{1B}-r_{1A}}\cdot\left\{\ln\left[\frac{S_A(\omega)}{A_{1A}(\omega,t_{UV},r_{1A})\cdot\sqrt{r_{1A}}}\right]\right\}\right\rangle} \quad (5\text{-}10)$$

where A_{1O} is the amplitude of the first AE signal excited at the source position.

From Equation (5-10), the amplitude of the AE signal at the i^{th} AE source at the source position can be calculated by Equation (5-11) using the AE amplitudes detected by sensors A and B at different propagation distances:

$$A_{iO}(\omega)=e^{\left\langle\frac{r_{iA}}{r_{iB}-r_{iA}}\cdot\left\{\ln\left[\frac{S_B(\omega)}{A_{iB}(\omega,t_{UV},r_{iB})\cdot\sqrt{r_{iB}}}\right]\right\}-\frac{r_{iB}}{r_{iB}-r_{iA}}\cdot\left\{\ln\left[\frac{S_A(\omega)}{A_{iA}(\omega,t_{UV},r_{iA})\cdot\sqrt{r_{iA}}}\right]\right\}\right\rangle} \quad (5\text{-}11)$$

A_{iO} is derived using $\alpha_i(\omega,t_{UV})$, which includes the frequency dependence and environmental degradation factor (UV irradiation); A_{iO} is therefore not affected by the attenuation factor.

Table 5.1 shows examples of calculating amplitude at source A_{iO} using real AE data detected for the #5 woven GFRP specimen using Sensors 1 and 2, which were 15 mm and 30 mm from the AE source, respectively. For Source 1, the amplitudes detected by Sensors 1 and 2 were 70 and 63 dB_{AE}, respectively. The AE centroid frequencies detected by Sensors 1 and 2 differed, although $\alpha_i(\omega, t_{UV})$ in Equation (5-4) was assumed to be same in this calculation. The propagation distances r_{iX} were known in this experiment (15 mm and 30 mm, respectively), so the AE amplitude at the source could be calculated using Equation (5-11). The estimated amplitude for Source 1 was 88.8 dB_{AE}. Source 2 contained higher centroid frequencies compared with Source 1 and its estimated amplitude was 82.8 dB_{AE}. From these results, it is evident that the effect of the frequency dependence of attenuation is taken into account when using this method of estimation of the *b*-value.

Table 5.1 Examples of estimating acoustic emission source amplitudes.
(Data detected for #5 woven GFRP test was used. Sensors 1 and 2 were 15 mm and 30 mm from the acoustic emission source, respectively.)

		Source 1		Source 2	
		Sensor 1	Sensor 2	Sensor 1	Sensor 2
Propagation distance	[mm]	15	30	15	30
Centroid frequency	[kHz]	454	444	317	307
Amplitude	dB_{AE}	70	63	70	66
	μV	3163	998	3163	1994
Estimated amplitude at the source	dB_{AE}	88.8		82.8	
	μV	27445		13743	

5.3 Modified *b*-value

Sections 5.1 and 5.2 explained that the amplitude of AE at the source position was not affected by attenuation factor. A method for estimating the amplitude of AE at source was proposed and demonstrated in Section 5.2. In this section, a modified *b*-value, calculated using the amplitude distribution of AE at the source position, is proposed. The effectiveness of this modified *b*-value is evaluated using AE data presented in previous chapters.

Figure 5.1 shows the concept of the modified *b*-value, where the vertical axis shows cumulative number of AE hits and the horizontal axis shows the amplitude of AE. As explained in Section 5.2, the AE amplitude at the source can be calculated using two AE signals detected by Sensors 1 and 2. The distribution of AE hits can then be calculated using Equation (5-11). The double line in Figure 5.1 shows an image of calculated distribution: the modified *b*-value proposed in this thesis is the slope of this line.

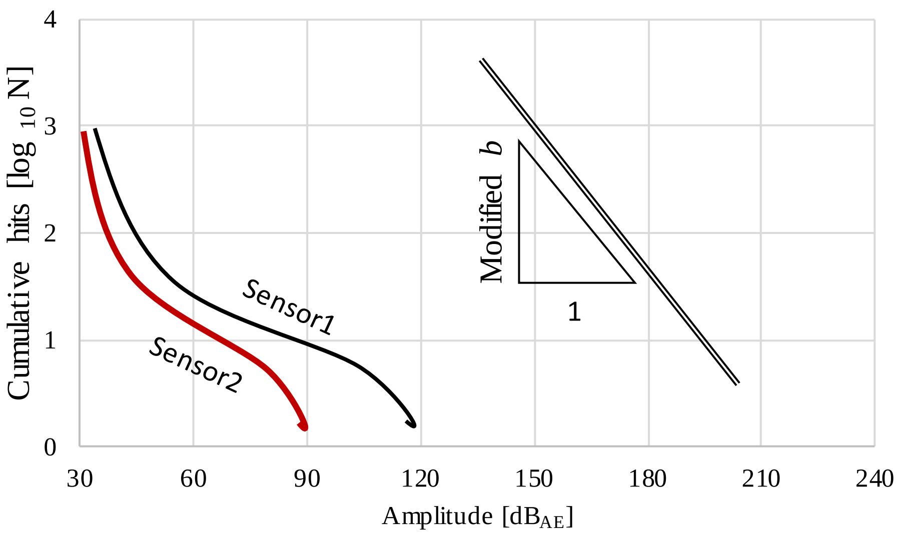

Figure 5.1 Concept of modified *b*-value

Figure 5.2 shows the amplitude distribution by AE source for the #5 woven GFRP tensile test at 0–2760 s (see Chapter 3.4). The vertical axis shows the cumulative number of AE hits; the symbols ○, ◊, and – indicate Sensors 1, 2, and 3 that were located 15, 30, and 45 mm from the AE source, respectively. The amplitude frequency distributions changed with propagation distance; the *b*-value (slope of fitted line) therefore changed with propagation distance (Sensor 1: 0.083; Sensor 2: 0.101; Sensor 3: 0.110).

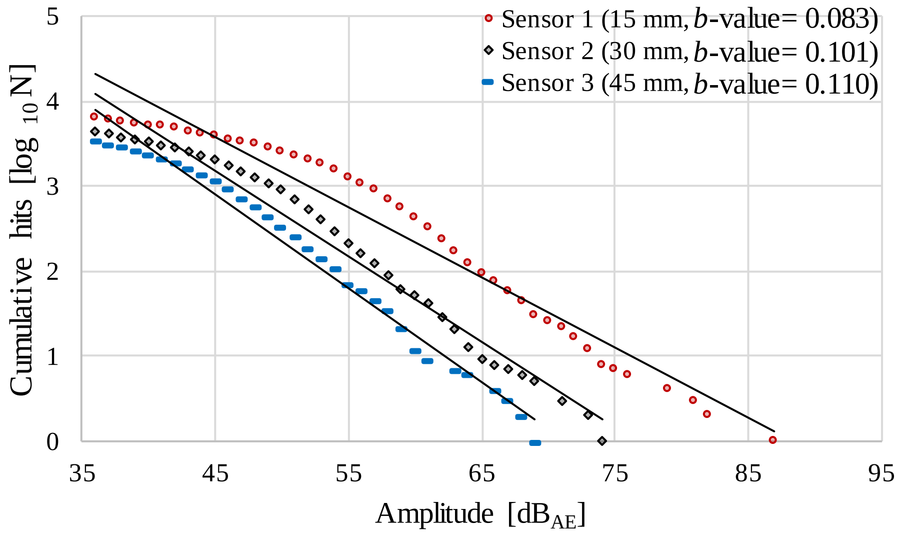

Figure 5.2 Plot of acoustic emission amplitude distributions detected in tensile testing of #5 woven glass-fiber-reinforced plastic specimen

Table 5.2 summarizes the AE data used for calculating the modified *b*-values. As explained in Section **, the AE amplitude at the source can be calculated using data detected by two sensors. In these experiments, we detected AE by three sensors attached at different propagation distances from the source. The amplitude at the AE source was then calculated by using AE signals detected by different combinations of these sensors. The AE data used for calculating the modified *b*-value were grouped and labelled as *1 to *4 in Table 5.2: those signals in Groups *1 to *3 were detected by all sensors; those in Group *4 were detected only by Sensors 1 and 2. As a result, the number of hits for Groups *1 to *3 was 3605, but was 4712 for Group *4. The amplitudes of those AE signals that disappeared (4712 − 3605 = 1107) during propagation from Sensor 2 to Sensor 3 decreased to below the threshold amplitude. The propagation distances of Groups *1 to *3 was 15 mm; that of Group *4 was 30 mm.

Table 5.2 Summary of acoustic emission data used for calculating modified *b*-value (S1: sensor 1; S2: sensor 2; S3: sensor 3)

		Propagation distance	AE group hits (0-2760 sec)			
		[mm]	S1	S2	S3	Number of hits
*1	S3 and S2	15	○	○	○	3605
*2	S3 and S1	30	○	○	○	3605
*3	S2 and S1	15	○	○	○	3605
*4	S2 and S1	15	○	○	×	4712

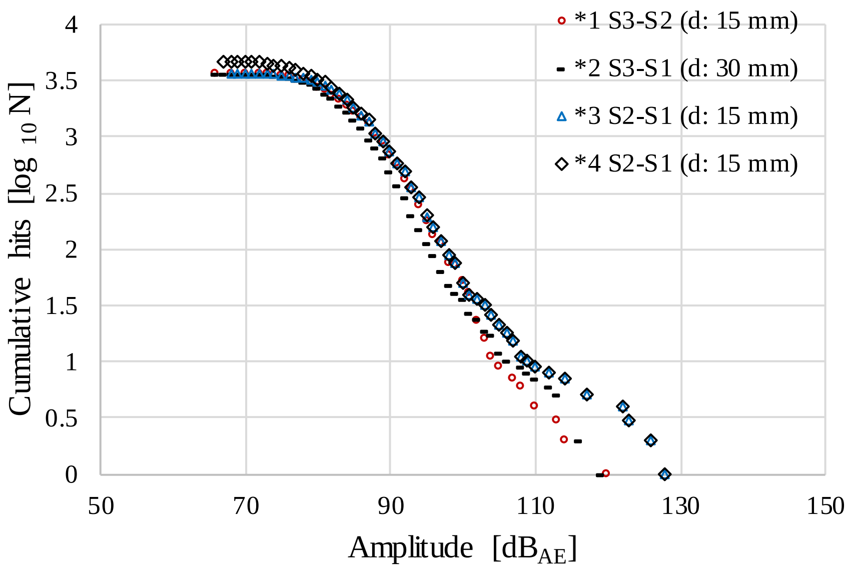

Figure 5.3 Determination of amplitude frequency distributions at the source position using different combinations of sensors and propagation distances

Even a small number of AE signals with large amplitude significantly affects the *b*-value, so data with large amplitude were deleted before calculation of the *b*-value. Figure 5.4 shows the same data as that of Figure 5.3, but with AE data deleted when the logarithm of the cumulative number of hits was below a value of 1. The fitted line and estimated *b*-value are also shown. The *b*-values calculated for Groups *1 to *4 were 0.068, 0.070, 0.070, and 0.071, respectively. When comparing the modified *b*-value with the general *b*-

value (Figure 5.2), the difference decreased, thereby proving that the modified *b*-value is not affected by the attenuation factor α that is a function of frequency and UV irradiation time.

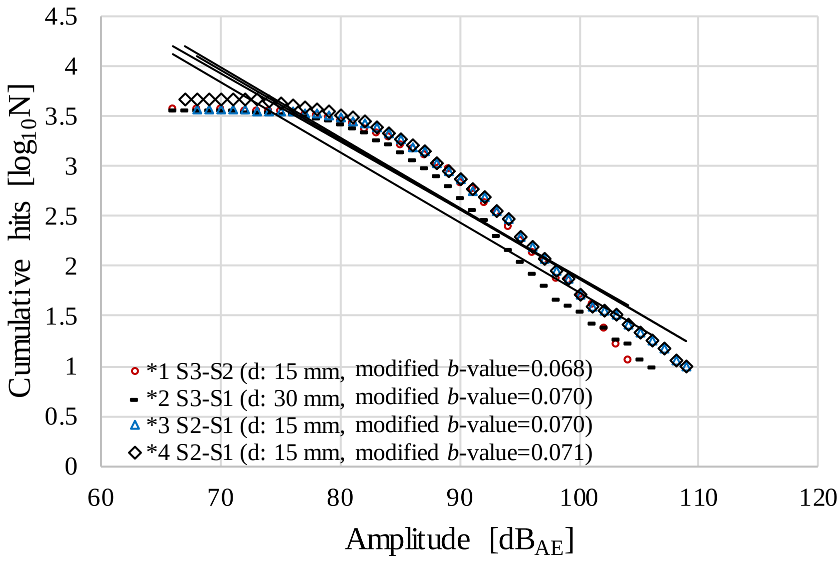

Figure 5.4 Determination of amplitude frequency distributions at the source position using different combinations of sensors and propagation distances and omitting cumulative hit data with a logarithmic value of less than 1, showing fitted lines and *b*-values

Finally, the validity of using Equation (3-1) for calculating the modified *b*-value was evaluated. Figure 5.5 shows the relationship between amplitude and propagation distance for AE detected from the GFRP specimen. The centroid frequencies of the three sets of AE signals were 278 kHz, 317 kHz, and 454 kHz. The data are overlaid by curves fitted using Equation (3-1). It is obvious that Equation (3-1) does take into account the effect of frequency dependence of attenuation.

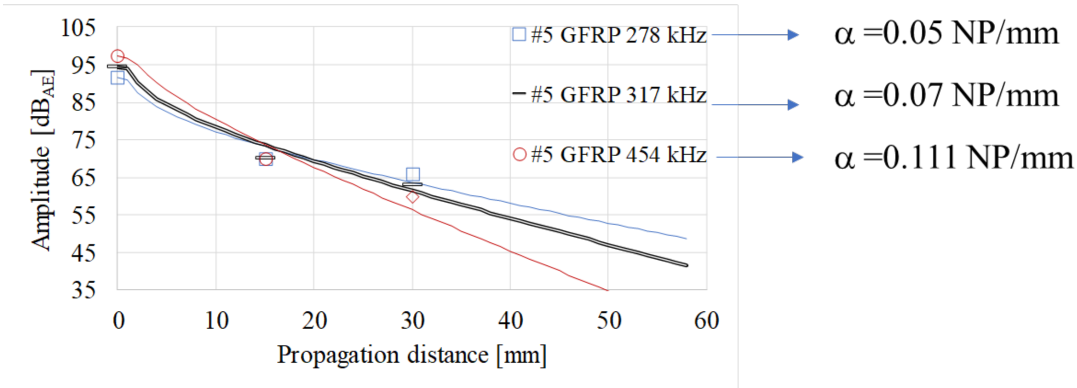

Figure 5.5 Relationship between acoustic emission amplitude and propagation distance with data fitted according to Equation (3-1)|

5.4 Conclusions

In this chapter, a new parameter, named the modified *b*-value, was proposed and feasibility of its use was evaluated. The modified *b*-value can be calculated from AE data detected at different propagation distances from an AE source and is the slope of the estimated AE amplitude distribution at the source position. The results are summarized as below.

1. The amplitude of an AE signal at the source position can be estimated using AE data detected at different propagation distances from the source using the following equation:

$$A_{iO}(\omega) = e^{\left\langle \frac{r_{iA}}{r_{iB}-r_{iA}} \cdot \left\{ \ln\left[\frac{S_B(\omega)}{A_{iB}(\omega, t_{UV}, r_{iB}) \cdot \sqrt{r_{iB}}} \right] \right\} - \frac{r_{iB}}{r_{iB}-r_{iA}} \cdot \left\{ \ln\left[\frac{S_A(\omega)}{A_{iA}(\omega, t_{UV}, r_{iA}) \cdot \sqrt{r_{iA}}} \right] \right\} \right\rangle}$$

2. A new parameter, named the modified *b*-value, was proposed, which is defined as the slope of AE amplitude distribution at the source position. This value is, in theory, not affected by attenuation factors that are functions of frequency and UV irradiation time.

3. To evaluate the feasibility of using this modified *b*-value, AE amplitude distributions at a source were calculated using real AE data detected for a woven GFRP specimen. All calculated amplitude distributions had a similar shape and their slopes (modified *b*-values) were similar, thereby proving that the modified *b*-value may not be affected by an attenuation factor that is a function of frequency and UV irradiation time. The modified *b*-value seems suitable for use in continuous monitoring of FRP structures.

Chapter 6 Conclusions

6.1 Conclusions

This thesis presents the applicability of using the general *b*-value, derived from acoustic emission (AE) data, for structural health monitoring in fiber-reinforced plastics (FRPs), as determined by both experimental and parametric studies. Because *b*-values change with propagation distance in these materials, it was found that the general *b*-value cannot be used for FRP structures. A new parameter, named the modified *b*-value, is proposed and its applicability discussed. The main results of this research are summarized as follows.

In Chapter 2, the applicability of the *b*-value to integrity evaluation of FRPs was assessed. AE signals arising from different fracture modes and their influences on the *b*-value were analyzed. Results from specimen #1$[90]_{16}$ indicated that when detected AE signals were caused by only matrix cracking, the *b*-value did not change with propagation distance; in contrast, when AE sources contained multiple fracture modes, such as those observed for specimens #2$[80]_{16}$, #3$[0]_8$, and cross-ply #4$[0/90]_8$, both the amplitude distributions and slopes of the fitted line (*b*-value) changed with propagation distance through the material. This result is in contrast to that observed for only matrix cracking and behavior of general concrete structures. These results showed that the general *b*-value cannot be used for evaluation of severity of damage in FRPs without considering the distance of propagation of the AE signals.

Chapter 3 analyzed the cause of changes in the *b*-value in these materials. The frequencies of detected AE signals during tensile testing of carbon- (CFRP) and glass- (GFRP) fiber-reinforced plastic specimens were investigated. These FRPs exhibit a very wide frequency band (100–660 kHz), compared with materials such as rock (1–10 kHz) and concrete (1–200 kHz). The wide frequency band of FRPS comprised frequency components relating to damage originating from matrix cracking, fiber pull-out, and fiber breakage. The change in *b*-value may be caused by changes in the proportion of each dominant frequency (fracture mode) on propagation due to the frequency dependence of the AE attenuation. A parametric study was conducted using calculated attenuation values from detected AE signals. The *b*-value of a single-frequency source did not change with propagation length; in contrast, a change occurred for multiple-frequency sources. These simulation results showed that changes in *b*-value may be caused by changes in the contribution of each frequency component as a function of propagation distance. These results proved the frequency dependency of the *b*-value.

Chapter 4 discussed the generation of AE signals by damage in degraded FRPs and their effect on the *b*-value. The amplitude distribution prior to 25% of the life time was changed significantly by ultraviolet (UV) irradiation time: the change in distribution of centroid frequency for the most irradiated specimen (300 h exposure) was larger than that of other specimens. This showed that UV irradiation may cause a change of AE attenuation in the high-frequency components of the signal, which may then affect the *b*-value. A parametric study was conducted to clarify the effects of UV irradiation in the absence of surface damage. When an AE signal was propagated with different frequency-dependent attenuation ratios, the amplitude distribution changed for a given propagation distance; however, when the attenuation parameter increased without a change in the frequency-dependent attenuation ratio, there was no change in amplitude distribution. The *b*-value therefore changed with change in the slope of the frequency dependence of the attenuation change at a given propagation distance.

In Chapter 5, a new parameter, named the modified *b*-value, was proposed and feasibility of its application evaluated. In theory, AE source amplitude is not affected by attenuation factors that are functions of both frequency and UV irradiation time. The amplitude at the source position of the i^{th} AE source can be calculated using the AE amplitudes detected by AE sensors (A and B) placed at different propagation distances, using the following Equation (5-11):

$$A_{iO}(\omega) = e^{\left\langle \frac{r_{iA}}{r_{iB}-r_{iA}} \cdot \left\{ \ln\left[\frac{S_B(\omega)}{A_{iB}(\omega, t_{UV}, r_{iB}) \cdot \sqrt{r_{iB}}} \right] \right\} - \frac{r_{iB}}{r_{iB}-r_{iA}} \cdot \left\{ \ln\left[\frac{S_A(\omega)}{A_{iA}(\omega, t_{UV}, r_{iA}) \cdot \sqrt{r_{iA}}} \right] \right\} \right\rangle} .$$

We proposed the modified *b*-value using the calculated amplitude at the source position. All calculated amplitude distributions had similar shape and the modified *b*-values of these distributions were also similar. It was proved that the modified *b*-value may not be affected by an attenuation factor that is a function of frequency and UV irradiation time. The modified *b*-value therefore appears to be suitable for use in continuous monitoring of FRP structures.

6.2 Future work

The modified *b*-value proposed in this study can only be used when the source is located on the sensor line (see Figure 6.1). The algorithm needs to be changed so that the modified *b*-value can be estimated even if the source is not located on the sensor line. This requires discussion of the orientation dependence of the attenuation factor.

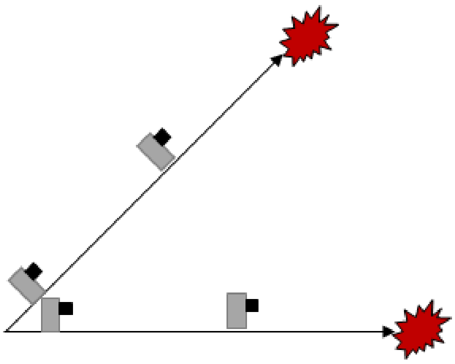

Figure 6.1 Limitation of application of the modified *b*-value

To evaluate effect of orientation dependence of the attenuation factor, several AE sensors were attached around an AE source by changing the angle (see Figure 6.2) at which the AE signals were detected. As shown in Figure 6.2, there appears to be little dependence of orientation of the attenuation factor on the *b*-value.

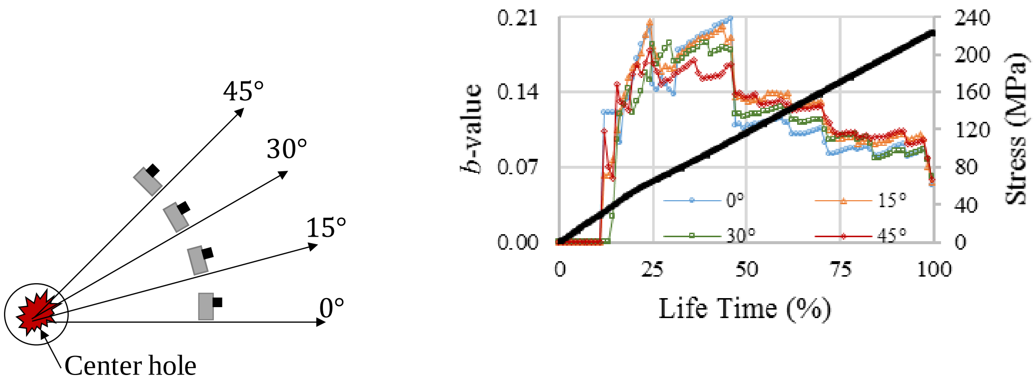

Figure 6.2 Orientation dependence of *b*-value

To understand the orientation dependence of the *b*-value, Figure 6.3 shows the change of AE parameters according to propagation angle. An AE signal of 100 kHz at the source changed with sensor location and showed the orientation dependence indicated in Figure 6.3(a). At the same time, the slope of frequency dependency of attenuation did not change, as shown in Figure 6.3(b). These results indicated that the *b*-value is less affected by propagation angle when the propagation distance of AE signals is constant. Further experimentation is required to confirm this finding.

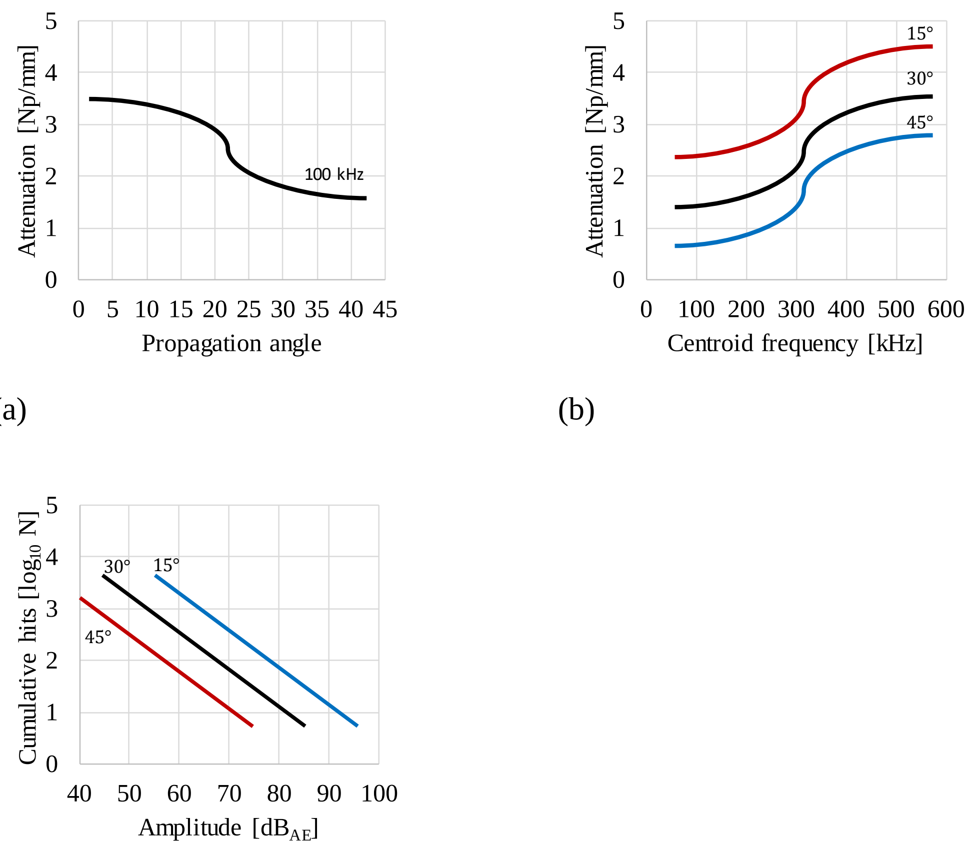

(a) (b) (c)

Figure 6.3 Variation in acoustic emission parameters for sensor locations when the propagation angle varied from 0° to 45°. (a) Attenuation (100 kHz), (b) frequency dependence of attenuation, and (c) *b*-value

When calculating the modified *b*-value, it was assumed that the attenuation did not change with increasing propagation distance; however, AE signals contain a wide range of frequencies and the higher-frequency region attenuates more rapidly than the lower-frequency region, thereby changing attenuation with propagation distance. It is therefore necessary to consider the attenuation dependence of propagation distance. In future work, optimization of the modified *b*-value, taking into consideration the attenuation dependence of propagation distance, is necessary.

List of publications

Published papers

(1) **<u>Doyun Jung</u>**, Yoshihiro Mizutani, Akira Todoroki, Yoshiro Suzuki, Change in *b*-value by AE Propagation Length in CFRP, Journal of Acoustic Emission. 2016, Vol. 33, pp. 123-129.

(2) **<u>Do Y. Jung,</u>** Yoshihiro Mizutani, Akira Todoroki and Yoshiro Suzuki (2017) Frequency Dependence of the *b*-value used for Acoustic Emission Analysis of Glass Fiber Reinforced Plastics, Open Journal of Composite Materials, (accepted)

International conferences

(1) <u>Doyun Jung</u>, Yoshihiro Mizutani, Akira Todoroki and Yoshiro Suzuki, "Fracture Behavior of Deteriorated FRP by UV radiation", PROGRESS in ACOUSTIC EMISSION XVIII, (2016) Dec 5-8, Kyoto (Japan), pp.169-175. (査読付きフルペーパー)

(2) <u>Doyun Jung</u>, Yoshihiro Mizutani, Akira Todoroki and Yoshiro Suzuki, "Study on Change of *b*-value by Different Fracture Mode in GFRP", Proceedings of International Conference on Asia-Pacific Conference on Fracture and Strength, (2016) Sep 19-21, Toyama (Japan), p p.219-221.

(3) <u>Doyun Jung</u>, Yoshihiro Mizutani, Akira Todoroki and Yoshiro Suzuki," Assessing Damage of GFRP Using *b*-value Analysis of AE Signals", Proceedings of the 10th Asian-Australasian Conference on Composite Materials, (2016) Oct 16-19, Busan (Korea), pp.118-119.

(4) <u>Doyun Jung</u>, Yoshihiro Mizutani, Akira Todoroki and Yoshiro Suzuki, "Change in *b*-value by AE Propagation Length in GFRP", Proceedings of the Asian Conference on Experimental Mechanics, (2016) Nov. 13-16, Jeju (Korea), pp.27-28.

(5) <u>Doyun Jung</u>, Yoshihiro Mizutani, Akira Todoroki, Yoshihiro Suzuki, "Study on frequency dependence of *b*-value", the 10th Korea-Japan Joint Symposium on Composite Materials, (2015) Oct 28~30, Jeonju (Korea) pp. 81-82.

---

(1) <u>Doyun Jung</u>, Yoshihiro Mizutani, Akira Todoroki and Yoshiro Suzuki, "CHANGE IN *b*-VALUE BY AE PROPAGATION LENGTH IN CFRP", Proceedings of the 32^{nd} European Conference on

Acoustic Emission Testing, (2016) Sep 07-09, Prague (Czech Republic), p p.231-238. (査読付きフルペーパー) 学会誌・論文誌等と同じ内容

Domestic conferences

(1) Doyun Jung, Yoshihiro Mizutani, Akira Todoroki and Yoshiro Suzuki, "Frequency dependence of *b*-value used for AE analysis", 日本機械学会〔No15-6〕M&M2015 材料力学カンファレンス 講演論文集, (2015) Nov 21 ~23, Tokyo (Japan), pp. OS0415-251.

(2) Doyun Jung, Yoshihiro Mizutani, Akira Todoroki, Yoshihiro Suzuki, "A study of the change in *b*-value by AE propagation length" Proceeding of the 2015 National Conference on Acoustic Emission, (2015) Nov 19~20, Nagoya (Japan), pp. 197-202. (査読付きフルペーパー)

Other research

(1) Abdalla Abdal-hay, NPG. Suardana, Do Yeon Jung, Kwang-Seog Choi, Jae Kyoo Lim, Effect of Diameters and Alkali Treatment on the Tensile Properties of Date Palm Fiber Reinforced Epoxy Composites, international journal of procession engineering and manufacturing Vol. 13, No. 7, pp.1199-1206

(2) N.P.G. Suardana, Ali Abdalla, Do Yeon Jung, Jae Kyoo Lim, Characterization and Possibility of Coconut Filter Fibers as Reinforcement for Polymers, Advanced Materials Research Vols. 217-218 (2011) pp 1202-1207

(3) Do Yeon Jung, Abdallah. Abdel-hay, Jae Kyoo Lim, Study on Applied load and Irradiation of Ultraviolet (UV) Aging of Polycarbonate Characteristics: Consequences on Mechanical Properties, Advanced Materials Research Vol. 472-475 (2012) pp. 1361-1365

Abdalla Abdal-hay, Do Yeon Jung, Kang Lee, G.T.Abdel-Jaber,Jae Kyoo Lim, Study on Water Absorption and Impact Properties of Vegetal Composites Material: Composite Structures, Advanced Materials Research Vol. 530 (2012) pp. 34-39